Sensory Information Processing

Detection, Feature Extraction, & Multimodal Integration

Paul Friedel

Sensory Information Processing

Detection, Feature Extraction, & Multimodal Integration

Paul Friedel

Wir, Stäubchen auf der Fläche unseres Planeten, der selbst kaum ein Sandkorn im unendlichen Raume des Weltalls zu nennen ist, wir, das jüngste Geschlecht unter den Lebendigen der Erde, nach geologischer Zeitrechnung kaum der Wiege entstiegen, noch im Stadium des Lernens, kaum halb erzogen, mündig gesprochen aus gegenseitiger Rücksicht, und doch schon durch den kräftigeren Antrieb des Causalgesetzes über alle unsere Mitgeschöpfe hinaus gewachsen und sie im Kampf um das Dasein bezwingend, haben wahrlich Grund genug stolz zu sein, dass es uns gegeben ist „die unbegreiflich hohen Werke" in treuer Arbeit langsam verstehen zu lernen, und wir brauchen uns nicht im Mindesten beschämt zu fühlen, wenn dies nicht gleich im ersten Ansturm eines Icarusfluges gelingt.

<div align="right">

Hermann von Helmholtz, Die Thatsachen
in der Wahrnehmung

</div>

Learned conversation is either the affectation of the ignorant or the profession of the mentally unemployed.

<div align="right">

Oscar Wilde, The Critic as Artist

</div>

Preface

The brain is an incredibly complex piece of machinery. Many billions of neurons are interconnected by an even larger number of synapses. Most neurons receive their input predominantly from other neurons. Nonetheless, *nothing* in the brain happens in the absence of any form of external input. The brain can be seen as nothing more than a—very intricate—device that transforms external inputs into muscle action. The behavior of the animal must be adapted to the environmental circumstances in an optimal way. For this reason, it is very important that sensory input is detected and processed as efficiently as possible.

In addition to the traditional human "five senses" (touch, vision, hearing, smell, and taste), there are many sensory systems that deal exclusively with body-internal processes. Examples are sensors monitoring the position of the limbs and the "touch-sensitive" neurons in the gut. Another group of sensors monitors gravity, heat, cold, pain etc. Many more sensory systems have evolved in other animals. Fish and amphibians use their lateral-line system to detect minute water movements, snakes and some insects have specialized infra-red radiation detection systems, a multitude of animals can detect the direction of polarization of light, birds find their way using a magnetic compass, and so on.

The list of possibilities is endless. It seems that for each physical quantity, an animal can be found that measures it and make use of the information so obtained. In spite of this perplexing multitude of different sensory systems, several general principles of key importance in sensory processing can be recognized. This thesis discusses three concrete realizations of such principles.

The first step in sensory processing is *detection* of a physical quantity by the sensory organ. In chapter 2, the detection and localization of ground-borne vibrations by snakes is discussed. Although snakes are generally believed to be deaf, they do have a functional inner ear. There is some sensitivity to air-borne sound, but because of the special construction of the their middle ear and lower jaw, snakes can also pick up substrate vibrations and literally *hear* prey moving about. Ground-borne vibrations cannot merely be detected; a simple neuronal model suffices to enable localization of the sound source as well. A mechanical description of the vibration detection process is given and source localization is explored through numerical simulations.

After signal detection, the sensory information is generally not simply relayed to higher processing centers "as is". *Feature extraction* is first performed to distill essential characteristics from the signal. In the visual system, for instance, the first processing layers identify the presence of edges, movement, and similar attributes of the input signal.

Signal periodicity plays an important role in the processing of auditory and vibratory input. It is perhaps the most important cue in object recognition and identification. The precise neuronal mechanism by which periodicity detection and recognition is achieved is, however, still unclear. Chapter 3 considers two neuronal models that can accomplish neuronal periodicity identification. Periodicity detection is performed in many different neuronal systems. These systems do not necessarily share a common neuronal architecture. Therefore, the models have been kept deliberately simple. The focus lies on understanding the basic properties of neuronal periodicity detection and *not* on the modeling of any specific system. To achieve such an understanding, mathematical

analysis is combined with numerical simulations.

The third fundamental concept in neuronal information processing that is discussed in this dissertation is *multimodal integration*. The combined use of several sensory systems radically enhances the efficiency of signal detection and processing. Multimodal maps, representing a unified spatial image of the external world, are indispensable in cognitive processing and motor control. All unimodal input maps to the multimodal map must be aligned. Only then a specific location in the outside world is represented at one unique location in the multimodal map. Two neuronal mechanisms to achieve such alignment are discussed in chapter 4. Again, a combination of mathematical analysis and numerical simulations is used to characterize the behavior of the models.

Organization of this thesis

Theoretical neuroscience is situated at the intersection of many disciplines: biology, physics, mathematics. . . This dissertation has therefore been written with a broad class of possible readers in mind. The first chapter gives an introduction to fundamental concepts in neuroscience that are needed to understand the rest of the work. Although the introduction is necessarily short, the references should enable every reader to find all essential information.

In chapter 2, vibration detection by snakes is discussed and chapter 3 discusses periodicity detection and identification. Multimodal integration, finally, is studied in chapter 4.

A short guide to the notation used in this work is given in appendix A. Some widely used neuron models are discussed in appendix B. The bibliography has been organized thematically. Since a wide range of topics is covered in this thesis, this seemed to make more sense than simply make one big list of references. Good reviews and other "must-read" material have been indicated and historically interesting material has been marked.

Thank you

Many people have been of help during my time at the Physik Department. In the first place, I thank Leo van Hemmen, my thesis supervisor. His enthusiasm for scientific research is unbounded, and through many interesting and vivid discussions I have learned a great deal about neuroscience.

The biological input provided by Bruce Young has been indispensable for the work on the snake auditory system. Without Bruce's knowledge of snakes, I would have been quite at a loss.

Writing this thesis would not have been possible without the pleasant interaction and cooperation with my colleagues at the "T35" chair. Moritz Bürck, Stefanie Bürck, Andreas Sichert, and Christine Voßen have proofread parts of the thesis and gave valuable comments. In addition, Moritz Bürck has shared an office with me for three years without getting insane. Many thanks!

I have had the opportunity to learn many things in Munich. In addition, I have made many new friends. I am very grateful to all of them for making me feel welcome and at home.

Finally, I thank Karla, who has always been there for support.

Munich, May 2008

Contents

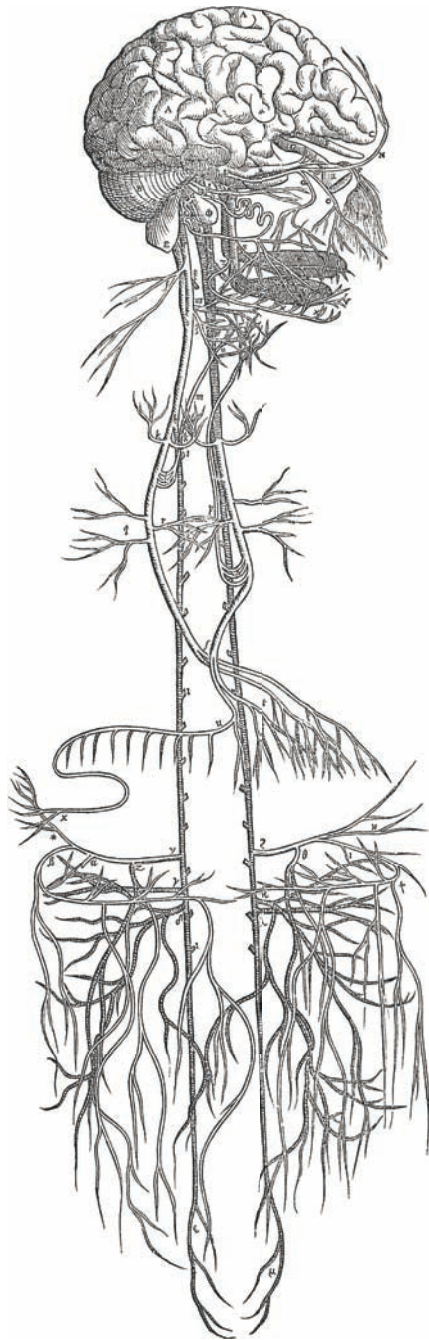# Contents

Contents

Andreas Vesalius' great work on human anatomy, De Humani Corporis Fabrica (On the Fabric of the Human Body), was published in Basel as early as 1543 [22]. This illustration shows his representation of the human nervous system.

... vielmehr ist die Erregung der Nervenfaser durch Helmholtz in die Reihe messbarer Vorgänge zurückgewiesen, und durch du Bois-Reymond mit Hilfe der Magnetnadel an sich erkennbar gemacht worden. Jetzt wissen wir sogar, dass dieser Vorgang sich in Form einer Welle von bestimmter Länge in der Nervenfaser fortpflantzt und unmittelbar auf electrischem Wege gemessen werden kann.

Julius Bernstein,
Untersuchungen über den Erregungsvorgang
im Nerven- und Muskelsysteme
Heidelberg, 1871

1. Neurons, learning, and sensory input

This chapter provides an overview of the anatomy and function of the central nervous system and its elementary building block, the neuron. Synaptic plasticity and some principles relating to the processing of sensory input and organization in neuronal maps are discussed.

1.1 Anatomy of the nervous system

The human nervous system consists of approximately 10^{11} nerve cells, also called neurons. More than 90% of these neurons are located within the brain.[1] Neurons are able to generate pulses of electrical current (called action potentials or spikes) in response to external input or signals from other neurons. These pulses travel away from the neuron's cell body through axons and are transmitted to other neurons through synapses. Ultimately, action potentials drive the muscle fibers and thereby control behavior.

Each neuron is on average connected to 1000 other neurons through axons and synapses [16]. This means that there are dazzling 10^{14} synapses present in the human brain. The high interconnectivity of the neurons combined with the high propagation velocity ($50\,\mathrm{m/s}$) of the action potentials makes the brain a highly efficient computing machine.

The nervous system can be separated into two parts: the peripheral nervous system and the central nervous system. The peripheral system consists of nerves which carry information from the body to the brain and vice versa. The peripheral nerves are connected to the spinal cord, which functions as the main "transmission cable" connecting the brain with the rest of the body. The spinal cord is usually not considered to be part of the peripheral nervous system.

The head region plays a special role. In addition to the peripheral nerves, there are twelve cranial nerves.[2] These nerves are responsible for the information transfer to and from the face and head, and they connect directly to the brain, rather than to the spinal cord.

The central nervous system consists of spinal cord and brain. The brain can be subdivided into three regions: the hindbrain, midbrain, and forebrain, see Fig. 1.1 [18]. The hindbrain is the evolutionary oldest part of the brain. It can be regarded as the direct continuation of the spinal cord into the brain. The brain stem, part of the hindbrain, controls functions that are absolutely

---

[1] An accessible introduction to brain anatomy and function can be found in [21]. A good book focusing solely on neuroanatomy is [2].

[2] In humans, there are only twelve cranial nerves, but 26 different cranial nerves are presently recognized in comparative neuroanatomy [8].
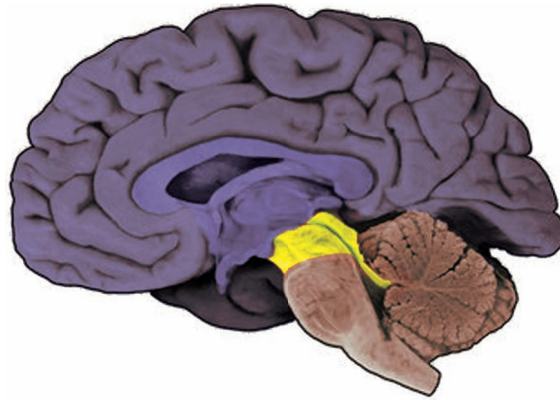
Figure 1.1: *Brain anatomy. This section through a human brain shows the hindbrain (brown), midbrain (yellow), and forebrain (purple). The cerebellum and cerebral cortex can easily be recognized by their wrinkled appearance. Image adapted from [19].*

essential for survival, such as respiration, heart action, digestion, facial expression, feeding behavior, and regulation of the sleep-wake cycle. The cerebellum, which is also part of the hindbrain, plays a role in motor coordination and is involved in basic learning and memory tasks.

In the midbrain, input from multiple sensory systems converges. The sensory information is relayed to the forebrain for further processing but motion control, especially relating to orientation reflexes, is partly coordinated by neurons in the midbrain.

The forebrain, finally, is the newest part of the brain and controls all "higher" functions, such as emotion, advanced sensory information processing, fine motor control, motivation, cognition, and language. The most important structure of the forebrain is the cerebral cortex [16]. In all mammals, it is the largest subdivision of the brain and in humans it even accounts for an estimated 80% of the total brain weight.

The cortex consists of a layer of densely packed neurons (gray matter). Under this layer lies a complex network of axons (white matter) that connects neurons located in different locations within the cortex. Although the cortex receives substantial input from other brain regions, about 85% of the neuronal connections are intracortical. Cortical neurons like to "talk" with other cortical neurons. Connectivity is very high and every cortical neuron may receive in the order of 10^4 inputs from other cortical neurons. In addition, the connections between cortical neurons can change in dependence upon neuronal activity patterns.

Schüz argues that cortical architecture is optimally suited to support associative processing of information [16]. Although humans do not have the biggest brain of all animals, they do have a relatively large brain-to-body weight ratio [15]. What really distinguishes humans from animals, however, is the huge number of cortical neurons that we possess. Following Schüz, the enormous increase in the number of cortical neurons arguably allowed humans to develop an unprecedented capability for associative thought. In this view, our enormous cortex can therefore be considered as a crucial ingredient that makes us who we are [18].

The basic layout of the cortex is identical in all mammals. The thickness of the combined gray and white matter layers is a couple of mm for all species, but the surface area of the cortex varies enormously between species [18]. Consequently, the cortical surface must be folded to make room for all the neurons. Figure 1.2 compares the brains of several mammals. Animals that are considered "intelligent" by intuitive standards often have brains that appear convoluted, implying a large cortical surface area.
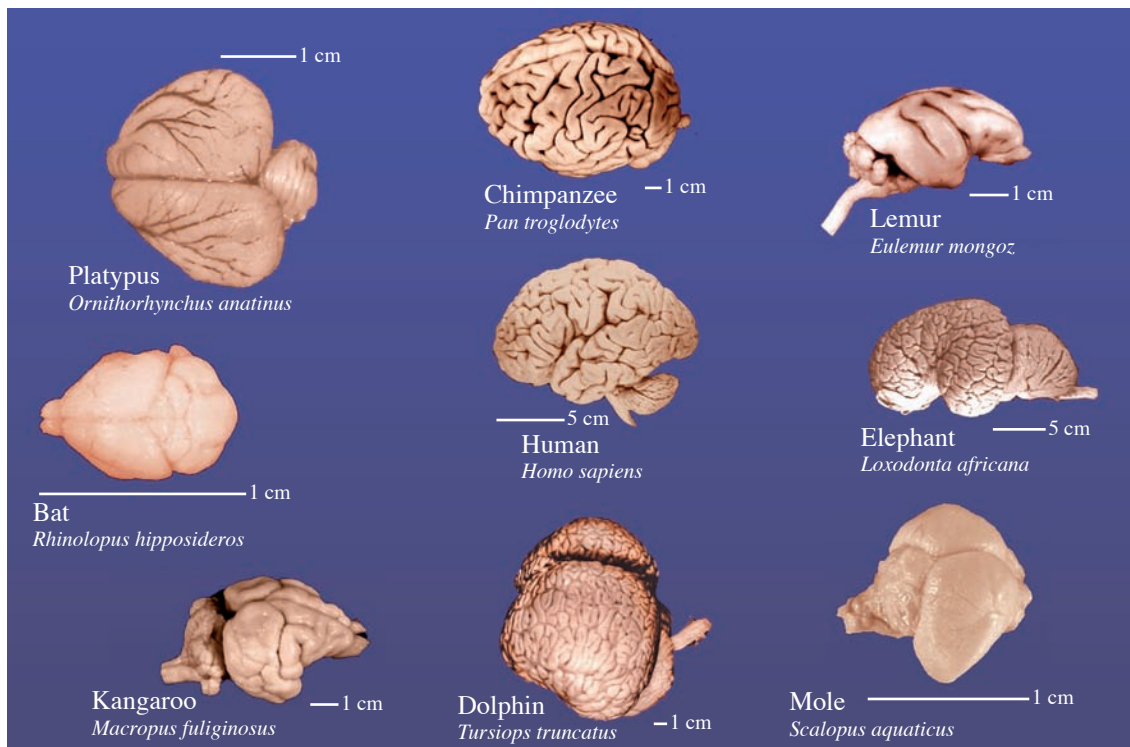
Figure 1.2: *Comparison of mammalian brains. Brain size is correlated with body size, but relative brain size varies considerably between animals. Except for human and chimpanzee, all brains displayed here belong to animals of different phylogenetic orders. Still, all these brains share the same basic structure. The lateral division into two brain halves is obvious and the cerebellum is clearly recognizable in all species as the globular structure lying directly upon the brain stem. Although the fundamental architecture does not vary greatly, the differences in surface appearance are striking. A highly convoluted appearance is associated with high intelligence. Images adapted from [3].*

1.2 Neurons and synapses

All computations in the brain are carried out by interconnected neurons. Apart from the odd exception, all neurons can be functionally divided into three parts: dendrites, soma, and axon (Fig. 1.3). In the dendrites, input from other neurons arrives. In the cell body (or soma) input from all dendrites is integrated, and if the electric current arriving exceeds a threshold, an action potential or spike is formed at the axon hillock. There, the axon leaves the neuron to propagate its spikes to other neurons. It is helpful to think of dendrites as the input unit of the neuron. The soma can in this picture be seen as the processing unit, and the axon can be thought of as output unit of the neuron.

1.2.1 Membrane properties

The cell membrane of a neuron contains many ion channels, which are each permeable to specific ion types [7]. These ion channels electrically connect the intracellular and extracellular fluid. Most of the channels on the dendrites and the soma are passive: the permeability and thus the electrical conductivity remain constant. Four ion types playing an especially important role in neuron functioning are Na^+, K^+, Ca^{2+}, and Cl^-.
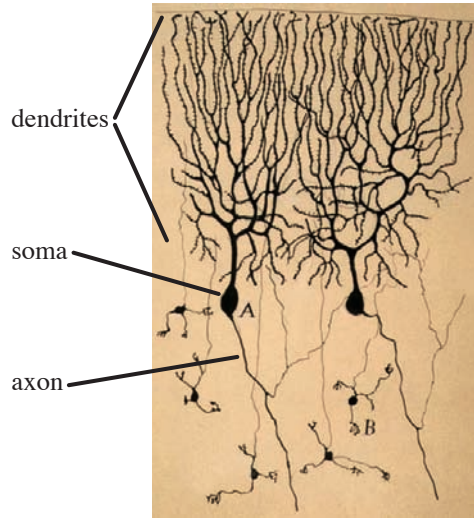
Figure 1.3: *Drawing of neurons from the pigeon cerebellum by the famous neuroanatomist Santiago Ramón y Cajal. The basic design of a neuron is readily observed. Input reaches the neurons through synapses located on the dendritic tree, in the top half of the figure. In the soma, the input current from the dendrites is integrated and if a certain threshold is exceeded, an action potential is generated. The action potential travels to other neurons along the axon.*

On the axon hillock and the axon itself, many ion channels are *active*. The permeability of active channels changes as a function of the voltage difference across the membrane. In addition, ion pumps actively transport ions across the cell membrane. This rich electrical structure is the primary feature that allows for rapid communication between neurons.

The ion pumps try to maintain a concentration gradient across the membrane. The concentration gradient for an ion species x leads to an associated across-membrane reversal potential E_x given by the Nernst equation [36, 40]

$$E_x = \frac{RT}{z_x F} \ln \left(\frac{[x]_o}{[x]_i} \right) . \tag{1.1}$$

Here, R, F, and T are the gas constant, Faraday constant, and temperature. The valency of the ion x is denoted by z and $[x]_o$ and $[x]_i$ denote the extracellular and intracellular concentration.

The reversal potential E_x is the membrane potential that would result if only the ion species x were present. The total steady-state potential, or resting potential V_r, across the membrane is given by the mean of the individual reversal potentials weighted by the conductance g_x of the membrane for each ion species

$$V_r = V_{\text{out}} - V_{\text{in}} = \frac{\sum_x g_x E_x}{\sum_x g_x} . \tag{1.2}$$

In most neurons, the resting potential is dominated by the potassium reversal potential. The potassium concentration is much higher within the cell than outside and the resting potential has a negative value, typically about -75 mV. Any change of the membrane potential with respect to this resting potential can propagate through the neuron and, if the deviation from the resting potential is large enough, generate an action potential. In this thesis, the voltage scale will always be chosen such that the resting potential is zero. The membrane potential will then simply be taken as the difference between the true, physical, membrane potential and the resting potential.

1.2.2 The action potential

Most of the active ion channels are closed at the resting potential. Therefore, the steady-state analysis in the previous section could be applied. However, as soon as the membrane voltage changes appreciably, the active channels may open. This means that the simple analysis from the last section does not hold anymore since the channel conductances will not be constant. The Hodgkin-Huxley equations [30] describe the nonlinear dynamics of ion flux through a membrane if active channels are present (for details, see appendix B.1.2). In the classical case of the squid giant axon—the original object of study of Hodgkin and Huxley—there are two active channels that play a role in action potential generation, sodium and potassium channels. The dynamical interaction of these two types of ion channels can lead to short ($\sim$ ms) fluctuations of the membrane potential with an amplitude of $\sim 100\,\text{mV}$. Such a fluctuation is called an *action potential* or *spike*.

If, due to an electrical current input, the membrane potential at the axon hillock becomes significantly less negative (*depolarization*), the sodium channels open and sodium ions start crossing the membrane. Since the sodium concentration is higher outside the neuron than inside, positive charge starts flowing into the cell, further increasing the membrane potential. As the potential keeps rising, the sodium channels close again, blocking the positive inward current. At the same time potassium channels, which respond slower than the sodium channels, start to open. Since there is more potassium in the cell than outside, potassium starts flowing outwards. As a result, the membrane potential starts to sink, typically even somewhat undershooting the resting potential (*hyperpolarization*). Finally, all active channels close and ion pumps bring the membrane potential back to its resting value.

During the time that the potential is below its resting value, it is more difficult or even impossible to induce a new action potential. This is because the potential is further away from threshold and at the same time, many ion channels are still open, leading to efficient ion concentration balancing inside and outside. The time span in which the neuron is less excitable is called the refractory period.

It is clear that spiking is an all-or-none process. If the input is large enough, a spike results, but if the input is too small, nothing happens. This property makes neurons very efficient "binary" calculators. Already in 1943, McCulloch and Pitts tried to describe neurons using propositional logic [38]. There are many models describing neuronal spiking dynamics. The model developed by Hodgkin and Huxley is perhaps the most famous. However, the model is so detailed and complicated that it cannot be used readily in numerical simulations. In appendix B, some widely-used neuron models are discussed. Luckily, it turns out that very simple neuron models are often sufficient for building realistic simulations of neural networks.

Action potential generation is not a strictly local process. If ion concentrations at one location within the axon change, longitudinal ionic currents within the axon will occur that tend to equalize the ion distribution in the axon. In this way, a change in ion concentration at a particular position along the axon will lead to an induced concentration change in nearby axon parts. This leads in turn to opening of nearby ion channels and the action potential propagates through the axon.

Spikes can propagate from the axon hillock to the synaptic terminal at the end of the axon, but it is possible for an action potential to travel in the other direction as well. If a spike is induced experimentally by a current injection in the middle of an axon, it spreads in both directions along the axon. Under natural circumstances, synaptic input is integrated at the axon hillock and it is only there that an action potential can first arise [11]. Therefore, action potentials are always propagated away from the cell body. Reciprocal information flow from downstream neurons through the axon is not possible.
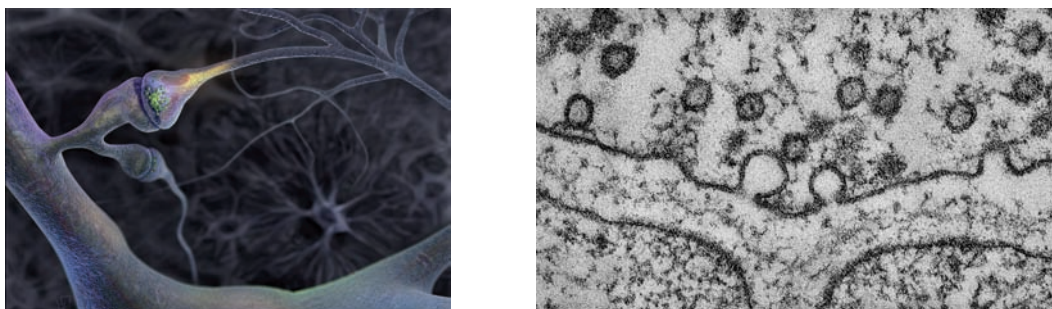
Figure 1.4: *Neurons make contact at synapses (left, artist reconstruction using actual measurements of synaptic structure). The presynaptic axon broadens into a synaptic terminal. The presynaptic membrane often shows a small protrusion, called a dendritic spine. The vesicles containing neurotransmitter are just visible here in green.*
The right side shows transmitter release at the neuromuscular junction. The vesicle release by the terminal in the top half of the picture triggers contraction of the muscle cells below.
Images taken from [262] (left) and [6] (right).

1.2.3 Synaptic input

The synapse connects an incoming neuronal axon to the dendritic tree of another neuron (Fig. 1.4). The last part of the axon broadens to form a presynaptic terminal that is separated from the postsynaptic membrane by a thin (~ 20 nm) gap, called the synaptic cleft. The cell membrane of the presynaptic terminal contains voltage-gated Ca^{2+} channels. As soon as a spike arrives, Ca^{2+} rushes into the terminal. Inside the terminal, vesicles containing neurotransmitter are continuously produced. If Ca^{2+} enters the terminal, some of these vesicles fuse with the cell membrane bordering the synaptic cleft. The neurotransmitter—often consisting of simple molecules derived from amino acids—diffuses across the synaptic cleft to the postsynaptic membrane.

The postsynaptic membrane contains chemically-gated ion channels. These channels feature molecular receptors that are sensitive to neurotransmitter. If neurotransmitter binds to the receptor, the corresponding ion channel opens and an ion current results. Subsequently, the neurotransmitter is taken up by the presynaptic cell for recycling, and eventually the ion channels close. Depending on the type of ion channel, positive or negative charge may flow into or out of the postsynaptic cell. The effect of synaptic input can therefore be *excitatory* (the postsynaptic membrane depolarizes and the cell becomes more excitable) or *inhibitory* (the postsynaptic membrane hyperpolarizes and the cell becomes less excitable).

Calculating the voltage change of the postsynaptic membrane in response to presynaptic activity is a difficult task. Just as in the case of the action potential the permeability of the membrane is not constant and the resulting nonlinear equations are difficult to solve. Fortunately, the excitatory or inhibitory postsynaptic potential (EPSP or IPSP) resulting from a single synaptic input is generally small. It can be shown that for very small or short responses, the synaptic event can be accurately modeled as a pure current pulse without conductance change [36].

Assuming a constant conductance, the change in membrane potential and the current are simply related through Ohm's law, which means that they are proportional. Typically, the current/potential quickly rises and decays exponentially to the resting value. The profile of the postsynaptic response (denoted by ε) to synaptic input at time $t = t_0$ is often described by an α-function (see p. 82)

$$\varepsilon = J \, \alpha(t - t_0, \tau_s) \,. \tag{1.3}$$

The parameter τ_s is the synaptic time constant and J gives the strength of the response.

1.2.4 Electrical conduction through dendrites

The change in membrane voltage at a synapse is transmitted along the dendritic tree. To a first approximation, the dendritic tree can be described as a passive cable-like structure [29, 36]. This cable is characterized by a longitudinal electrical resistivity per unit length (r_l) and a membrane capacitance (c_m) and resistivity (r_m), also per unit length. The longitudinal resistivity and the membrane capacitance increase linearly with the length of the cable and have dimension Ω/m and F/m, respectively. The longitudinal resistivity R_l of a piece of cable of length Δx is found by multiplication $R_l = r_l \Delta x$. The membrane resistivity, on the other hand, decreases with cable length since a larger cable surface means lower across-membrane resistivity. Therefore, r_m is given in units Ωm and the membrane resistivity R_m of a short cable segment is given by $r_m = r_m/\Delta x$.

Introducing the electrotonic length scale $\lambda = \sqrt{r_m/r_l}$ and the membrane time constant $\tau_m = r_m c_m$, the membrane voltage V along the length of the dendrite fulfills the cable equation (for derivation see [29, 36], remember that the resting potential has been set to zero)

$$\lambda^2 \frac{\partial^2 V}{\partial x^2} = \tau_m \frac{\partial V}{\partial t} + V - i_{\text{inject}} \; . \tag{1.4}$$

The input current per unit length is denoted with i_{inject}.

Equation (1.4) is similar to the diffusion equation (or heat equation) and can easily be solved for given input current and boundary conditions [257]. An important property of (1.4) is that no traveling wave solutions are possible. This means that any displacement from equilibrium will lose amplitude as it propagates through the dendrite. In addition, a voltage pulse will broaden as it travels to the soma.

The passive electrical structure of a membrane therefore has a screening effect on synaptic input. Signals from synapses that are located far away from the soma are generally relatively weak and smeared out. Especially for very large dendritic trees, this can be a real problem. There are many dendritic mechanisms that can locally enhance the transmission properties of dendrites. In addition, many dendrites are structured in such a way as to optimally allow the neuron to perform certain computations [13, 17].

1.3 Learning in neural networks

Learning in neuronal networks takes place by changing the connection strength between (groups of) neurons. This insight has been formulated already in 1949 by Donald Hebb in his famous book *The Organization of Behavior* [5, p. 62]

> Let us assume then that the persistence or repetition of a reverberatory activity (or "trace") tends to induce lasting cellular changes that add to its stability. The assumption can be precisely stated as follows: *When an axon of cell A is near enough to excite cell B and repeatedly or persistently takes part in firing it, some growth process or metabolic change takes place in one or both cells such that A's efficiency, as one of the cells firing B, is increased.*

Animal learning is basically the ability to predict patterns occurring in the outside world. In the classical Pavlov conditioning experiment for instance, a dog repeatedly experiences the sound of a bell followed shortly thereafter by the arrival of food. After a while the dog starts drooling at the sound of the bell, even before the food is brought in. The dog has learned the correlation between the sound of the bell and the arrival of food.

This is exactly what Hebb's rule establishes on a neuronal level. If groups of neurons are active shortly after one another, the connections between the neurons making up these groups are strengthened. In other words, Hebb's learning rule enables to learn correlations between neuronal firing patterns and thus, ultimately, correlations between events in the outside world.

1.3.1 Spike-timing-dependent plasticity

In the last decade, much evidence for a Hebbian learning mechanism on the single cell level has been found. It has been shown experimentally that the timing of presynaptic and postsynaptic spikes plays a crucial role. If a presynaptic spike from cell A arrives at a synapse shortly[3] before a postsynaptic spike is generated by the target cell B, the weight of the synaptic connection A→B is increased. On the other hand, if a presynaptic spike arrives after the postsynaptic spike is generated, the synaptic weight is decreased. In this way, input connections that actively help to bring the postsynaptic neuron across the firing threshold are strengthened and useless connections are weakened. This process of synaptic weight changes triggered by the precise timing of pre- and postsynaptic spikes has been dubbed spike-timing-dependent plasticity (STDP) [70].

The first experiments explicitly demonstrating STDP were carried out in the late nineties of the twentieth century [47, 62, 74], but indications of the importance of spike timing for learning have been found at least 15 years earlier [59] (see also the reviews [48, 51]). Only very recently has the connection between STDP and learning been demonstrated explicitly *in vivo* [63]. Many factors influencing STDP have been identified in the last years. Apart from spike timing, plasticity is influenced by the presence or absence of spike bursts, the number of spikes that have been initiated in the recent past, repetition rate of spike pairings, momentary weight of the synapse, location of the synapse on the dendritic tree, neuron type, and perhaps many more variables [49, 53, 60, 67, 72].

In addition to the "classical" Hebbian learning rule, other temporal requirements for learning have been discovered in several neuronal systems. Some synapses are strengthened whenever pre- and postsynaptic spikes occur within a small time interval, regardless of their temporal order. Even anti-Hebbian learning—where input connections are weakened if presynaptic input arrives after a postsynaptic spike and the other way around (e.g. [45, 52])—has been found. A short overview of some of these findings is given in [41, 65].

Although the molecular mechanisms underlying STDP have not been completely understood, it is known that the postsynaptic Ca^{2+} concentration plays an important role, in combination with the activity of a class of ion channels gated by so-called NMDA receptors [46, 61, 65, 73]. Besides the strengthening of individual synaptic weights generation, enlargement, and pruning of synaptic spines also plays an important role in learning [68]. This means that synaptic connections can be lost completely, but also that useful synaptic contacts can proliferate.

1.3.2 Modeling synaptic plasticity

Early attempts to model synaptic plasticity were based on correlations between the mean firing rates of pre- and postsynaptic neurons. The weight change J_{ij} of a synapse connecting presynaptic neuron i with postsynaptic neuron j can be generally written as (see [29])

$$\dot{J}_{ij} = F(J_{ij}, \nu_i^{\text{pre}}, \nu_i^{\text{pre}}) \tag{1.5}$$

where the arbitrary function F may depend on the value of J_{ij} itself and on the firing rates ν_i^{pre} and ν_i^{pre}.

It is possible to construct quite sophisticated models based on this principle (for instance the famous BCM-model [50]) but all rate-based models suffer from a lack of biological plausibility. Although some of the models may give biologically realistic results, it is hard to think of a mechanistic justification for using firing rates. This does not imply that a rate-based model cannot be correct as an effective description of learning processes (see e.g. [56]), but only that the use of firing rates alone will probably not provide a complete theory.

The experimental findings discussed in the previous section strongly suggest a description of plasticity relating weight changes to the timing of individual spikes. The state of a neuron, including

---

3   Typically, the time scale of learning is of the order of tens of ms, roughly comparable to the membrane time constant.

the firing of spikes, can be characterized by its time-dependent membrane potential V. Similarly to Eq (1.5), a general expression for the weight change as a function of the pre- and postsynaptic membrane potential at the synapse can be given [29]

$$\dot{J}_{ij}(t_0) = F\left[J_{ij}(t_0), V_i^{\text{pre}}(t \le t_0), V_j^{\text{post}}(t \le t_0)\right] . \tag{1.6}$$

The weight change can in principle depend on the complete (spiking) history of the membrane potentials up to the time $t = t_0$.

Expanding Eq. (1.6) using a Volterra series [263] around the equilibrium state $V_i^{\text{pre}} = V_j^{\text{post}} = V_r = 0$ clarifies its meaning. The expansion is

$$\dot{J}_{ij}(t_0) = \sum_{m,n=0}^{\infty} \int_{-\infty}^{t_0} \cdots \int_{-\infty}^{t_0} dr_1 \cdots dr_m ds_1 \cdots ds_n \; h_{mn}(J_{ij}, r_1, \ldots, r_m, s_1, \ldots, s_n)$$
$$\times V_i^{\text{pre}}(r_1) \cdots V_i^{\text{pre}}(r_m) V_j^{\text{post}}(s_1) \cdots V_j^{\text{post}}(s_n) \tag{1.7}$$

where the integration kernels are given as functional derivatives of the functional F,

$$h_{mn}(J_{ij}, r_1, \ldots, r_m, s_1, \ldots, s_n) =$$
$$\frac{1}{m!n!} \left[\frac{\delta^{m+n} F[J_{ij}, V_i^{\text{pre}}, V_j^{\text{post}}]}{\delta V_i^{\text{pre}}(r_1) \cdots V_i^{\text{pre}}(r_m) \delta V_j^{\text{post}}(s_1) \cdots V_j^{\text{post}}(s_n)} \right]_{V_i^{\text{pre}} = V_j^{\text{post}} = 0} . \tag{1.8}$$

After some shuffling of terms and introduction of new kernels $\tilde{h}$ the first few terms of the expansion are found as

$$\dot{J}_{ij}(t_0) = \tilde{h}_0 + \int_0^{\infty} dr \; \tilde{h}_1^{\text{pre}}(J_{ij}, t-r) \; V_i^{\text{pre}}(r) + \int_0^{\infty} ds \; \tilde{h}_1^{\text{post}}(J_{ij}, t-s) \; V_j^{\text{post}}(s)$$
$$+ \int_0^{\infty} \int_0^{\infty} dr_1 dr_2 \; \tilde{h}_2^{\text{pre}}(J_{ij}, t-r_1, t-r_2) \; V_i^{\text{pre}}(r_1) V_i^{\text{pre}}(r_2)$$
$$+ \int_0^{\infty} \int_0^{\infty} ds_1 ds_2 \; \tilde{h}_2^{\text{post}}(J_{ij}, t-s_1, t-s_2) \; V_j^{\text{post}}(s_1) V_j^{\text{post}}(s_2) \tag{1.9}$$
$$+ \int_0^{\infty} \int_0^{\infty} dr ds \; \tilde{h}_2^{\text{corr}}(J_{ij}, t-r, t-s) \; V_i^{\text{pre}}(r) V_j^{\text{post}}(s)$$
$$+ \cdots$$

The first term of order 0 is just a constant growth or decay term. The terms of first order take into account the occurrence of pre- or postsynaptic spikes by themselves. The second order term takes into account pairs of spikes occurring at different times and so on. Every higher order term introduces a learning term requiring the interaction of more spikes.

Two assumptions help to simplify this equation considerably.

1. Since action potentials have a very short duration ($\sim 1\,\text{ms}$) compared to typical interspike intervals and the membrane relaxation times ($\gtrsim 20\,\text{ms}$) the presynaptic membrane potential can be written as a sum of delta functions

$$V_i^{\text{pre}} = \sum_f \delta(t - t_i^f) . \tag{1.10}$$

The times t_i^f denote the arrival of the presynaptic spike at the synapse. The postsynaptic membrane potential similarly becomes

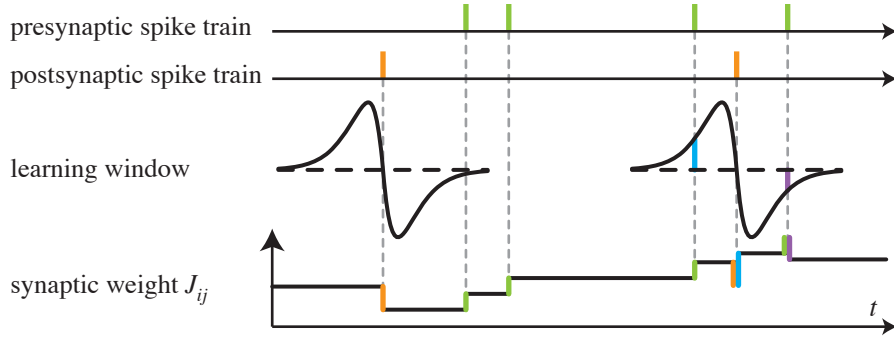$$V_j^{\text{post}} = \sum_g \delta(t - t_j^g) . \tag{1.11}$$

Figure 1.5: *Illustration of the learning process from Eq. (1.14). The top two rows show a hypothetical pre- and postsynaptic spike train. At every presynaptic spike, the weight changes by an amount w^{pre} (green). All postsynaptic spikes induce a weight change w^{post} (orange). All pre-post pairs of spikes introduce a weight change that depends on the learning window. If the temporal separation between the spikes is too large, nothing happens (left part of diagram). If a presynaptic spike closely precedes a postsynaptic spike (right part of diagram), the weight increases (blue) and the opposite situation leads to a decrease of the weight (purple).*

2. All terms that are of second order or higher in V_i^{pre} or V_j^{post} are neglected.

The resulting equation describing the synaptic weight change is (suppressing the J_{ij} dependence of the parameters in the notation)

$$\dot{J}_{ij}(t) = \tilde{h}_0 + \sum_f \tilde{h}_1^{\text{pre}}(t - t_i^f) + \sum_g \tilde{h}_1^{\text{post}}(t - t_j^g) + \sum_{f,g} \tilde{h}_2^{\text{corr}}(t - t_i^f, t - t_j^g). \qquad (1.12)$$

A last assumption now finalizes the simplifications:

3. All weight changes are instantaneous. That is, there is no smooth modification of the weight, but rather an immediate change as soon as a spike occurs.

This idea is expressed by

$$\tilde{h}_1^{\text{pre}}(t - t_i^f) \rightarrow \eta w^{\text{pre}} \delta(t - t_i^f) \qquad (1.13\text{a})$$

$$\tilde{h}_1^{\text{post}}(t - t_i^f) \rightarrow \eta w^{\text{post}} \delta(t - t_i^g) \qquad (1.13\text{b})$$

$$\tilde{h}_2^{\text{corr}}(t - t_i^f, t - t_j^g) \rightarrow \eta W(t_i^f - t_j^g), \qquad (1.13\text{c})$$

introducing the real constants w^{pre} and w^{post} and the real function W, called the learning window. The learning parameter η sets the magnitude of the weight change occurring at one spike and consequently the learning speed. Further, let $\tilde{h}_0 \rightarrow \eta w_0$.

Putting everything together finally gives

$$\dot{J}_{ij}(t) = \eta \left[w_0 + \sum_f w^{\text{pre}} \delta(t - t_i^f) + \sum_g w^{\text{post}} \delta(t - t_j^g) + \sum_{f,g} W(t_i^f - t_j^g) \right]. \qquad (1.14)$$

Most models in the literature have used Eq. (1.14) or an equivalent formulation to describe STDP, often with $w_0 = 0$ (e.g. [54, 55, 57, 66, 69, 70]). The most interesting term in Eq. (1.14) is the learning window $W(t^{\text{pre}} - t^{\text{post}})$, illustrated in Fig. 1.5.

The figure shows that every time a pre- or postsynaptic spike is generated, the synaptic strength changes by a fixed amount. In addition to this, pre/post spike pairs occurring in close temporal

vicinity give rise to a weight change that is determined by the shape of the learning window. The learning window is a function of the difference s between a pre- and postsynaptic spike: $s = t^{\text{pre}} - t^{\text{post}}$. Experiments suggest that $W(s)$ should be positive for negative values for s, when a presynaptic spike precedes a postsynaptic spike. A negative value for $W(s)$ is found for values $s > 0$. For very large interspike intervals common sense and experimental findings dictate that the learning window should vanish. The learning window shown in Fig. 1.5 has these typical characteristics.

1.3.3 Modifications to the basic learning model

Learning models based on spike pair correlations do a good job explaining many plasticity experiments. Be that as it may, including only pairs of spikes into the model does lead to some complications. In experiments, a *repetition protocol* is used. A pair of pre- and postsynaptic spikes with a specific time difference are induced using current injections. Since a single pairing usually does not lead to any measurable weight change, the pairing is repeated a large number of times. As the repetition frequency of the spike pairs is modified, the measured weight change differs. This has to do with the fact that neighboring spike pairs influence each other if their temporal separation becomes small.

Now imagine a series of pre-before-post pairs, leading to weight potentiation. If the frequency of the pairings is increased, the first (presynaptic) spike starts to "feel" the last (postsynaptic) spike of the preceding pair. This means that extra post-before-pre pairs are introduced and the total weight increase should therefore become smaller if the pairing frequency rises. In spite of that, experiments actually show a *stronger* potentiation effect at higher repetition rates (see discussion in [64]).

This problem can be at least partially solved if higher order terms in (1.7) are taken into account. Pfister and Gerstner [64] found that introducing spike triplet interactions into the learning rule produces a better match between theory and experimental results. This improvement comes at the cost of a slightly more complicated theory. In many cases it will suffice to use a simple pair-based learning rule and in this dissertation triplet learning is never used.

Another extension to the basic learning algorithm is the inclusion of metaplasticity [42, 43, 44]. Metaplasticity means that the learning rule itself is changing over time. This may be caused by a temporary depletion of certain molecules or ions, but structural changes are also possible. It has recently been shown that NMDA receptors can laterally diffuse through the cell membrane to reach sites (synapses) of high activity [75]. Metaplasticity will not be further discussed in this dissertation.

1.4 Sensory input

Ultimately, all activity in the brain derives from external input. Through the senses, events occurring in the outside world are converted into spikes and sent to the brain. One of the key questions in neuroscience, and also a question underlying much of the work in this thesis, is how information is encoded into spike trains. A question closely related to this is how sensory information is processed and transformed by the brain to construct a useful representation of the environment. Depending on the context, a particular piece of information contained in a spike train may or may not be important. In fact, the brain *actively* filters all input to enhance any relevant information and suppress irrelevant information.

To describe the response of neurons in a sensory pathway, two characteristics are generally useful: the receptive field of a neuron and the quality of its response.

The receptive field of a neuron consists of the space of all inputs to which a neuron responds. In the visual system receptive fields have been characterized particularly well (see for example

[23])[4]. All neurons in the visual pathway respond optimally to input coming from a single specified spatial position. In addition, most neurons are inhibited if input from a slightly different position is presented and no response is obtained for input from all other directions. There are neurons that are selectively responsive to the presence of (moving) edges within their "best area". This sensitivity is often coupled to a responsiveness to one particular edge orientation.

In the auditory system, neurons are generally very precisely tuned to specific sound frequencies. Although this strains the normal definition of the receptive field somewhat, auditory neurons can be considered to have very narrow receptive fields in the frequency domain.

The second important feature characterizing the response of a sensory neuron is the quality, or sharpness, of the response. For responses as a function of input signal position, a measure of response quality is given by the *vector strength*, described below. The vector strength can also be used to characterize the temporal accuracy of the neuronal response to a periodic input signal. A high value of the vector strength implies that the neuron preferentially spikes at a particular phase of the input signal. This phenomenon is called phase locking. Before the concept of vector strength is explained, it is helpful to discuss vector coding.

Vector coding

The existence of vector coding was discovered by Georgopoulos et al. [4]. They found that in a population of cortical motor neurons, each of the neurons "represented" a particular direction of arm movement. Although the firing rates of the individual neurons were stochastic, the actual direction of arm movement could be predicted if the activity of all the neurons was vectorially summed up. If the preferred direction of cell p is given by $\hat{\mathbf{e}}_p$ and its activity (firing rate) by r_p, the sum-vector $\mathbf{X}$ can be defined as

$$\mathbf{X} = \sum_p r_p \hat{\mathbf{e}}_p \ . \tag{1.15}$$

Georgopoulos et al. found that the direction of arm movement corresponded to the direction of $\mathbf{X}$. Direction is thus determined by the summed population activity of all participating neurons.

The idea of vector coding was soon confirmed (e.g. [12]), and it is now believed to play a role in all motion coding. In some cases, only a couple of neurons suffice to reliably code movement direction [14, 20][253].

Vector strength

It is straightforward to define the accuracy of the vector code. The *vector strength* VS is given by the ratio of the length of the sum-vector $\mathbf{X}$ and the total neuronal activity

$$\text{VS} = \frac{|\mathbf{X}|}{\sum_p r_p} = \left| \frac{\sum_p r_p \hat{\mathbf{e}}_p}{\sum_p r_p} \right| \ . \tag{1.16}$$

From this definition it is clear that VS always lies between 0 and 1. VS $= 0$ means that there is no directional information whatsoever. A value VS $= 1$ means that all active neurons perfectly line up into the same direction.

With a slight modification, the vector strength can also be used to characterize the temporal accuracy of the response to a periodic signal. This was first done by Goldberg and Brown [129]. Considering one neuron receiving periodic input, its spiking times can be related to the instantaneous phase of the input signal. For each spike p, there is a corresponding phase $(\varphi_p)_{\text{mod } 2\pi}$. The sum-vector is defined as

$$\mathbf{X} = \sum_p e^{i\varphi_p} \ , \tag{1.17}$$

---

[4] Early important work on this topic has been done by Hubel and Wiesel [9, 10].

where all spikes have unit weight.

If N is the total number of spikes, the vector strength, or *phase locking strength*, can be defined as

$$\text{VS} = \frac{|\mathbf{X}|}{N} = \left| \frac{\sum_p e^{i\varphi_p}}{N} \right| . \tag{1.18}$$

The correspondence to Eq. (1.16) is evident if one realizes that $e^{i\varphi_p}$ can be interpreted as a unit vector in two-dimensional space.

As in the spatial case, the vector strength in (1.18) is a number between 0 and 1. The value of VS does not depend on the preferred phase of the spike response, but only on the temporal accuracy of the spikes around this phase. A high vector strength means high accuracy. If VS is near 1, all spikes cluster around a single preferred (yet unknown) phase. A low value generally implies poor phase locking.

Some caution is necessary here, since there are cases in which very high accuracy can result in a low vector strength. If, for instance, a neuron always fires a high-precision spike at phase $\varphi = \bar{\varphi}$ and another spike at $\varphi = \bar{\varphi} + \pi$, the spikes add up to give a very low vector strength in spite of their high accuracy.

It is also possible to calculate the vector strength for a continuous function. It is well-known that every periodic function can be expanded as a Fourier series according to

$$f(t) = \sum_{n=-\infty}^{\infty} c_n e^{i\omega n t} \quad \text{with} \quad c_n = \frac{\omega}{2\pi} \int_{-\pi/\omega}^{\pi/\omega} dt \; f(t) e^{-i\omega n t} . \tag{1.19}$$

In case the function $f(t)$ is not perfectly periodical, it is possible to integrate over a large number z of "periods" to find c_n. The value of c_n must then be divided by z to obtain the correct result.

The vector strength can be defined as the ratio of the absolute value of the first Fourier coefficient and the zeroth Fourier coefficient.

$$\text{VS} = \frac{|c_1|}{c_0} = \frac{\left| \int dt \; f(t) e^{-i\omega t} \right|}{\int dt \; f(t)} . \tag{1.20}$$

As a check, a spike train can be substituted into (1.20). The spike train is described by $f(t) = \sum_g \delta(t - t^g)$, where the spikes occur at times $t = t_p$. Using this expression in (1.20) indeed gives (1.18), as expected.

1.5 Neuronal maps

Sensory information is very often processed in neuronal maps. A neuronal map is an array of neurons in which neighboring neurons respond to sensory stimuli that are similar. As an example, visual input in the mammalian brain is processed through multiple cortical layers which are organized according to the topography of the retinal input cells (retinotopic organization) [23]. In this way, neighboring neurons respond to visual input from neighboring points in space. Such a map of space has been discovered in many sensory systems, such as audition, somatosensory input, the lateral line system of amphibians and fish, snake infrared vision, and whisker input in rodents.

Neuronal maps are not limited to spatial representations. A well-known example is the organization of the auditory pathway in frequency-specific layers (tonotopy) [151, 128]. A neuronal map representing modulation frequencies present in auditory input has been claimed as well [157], but this has not been confirmed. Possibly the most striking example of a neuronal map is the *homunculus*[5], a complete representation of the human body surface in the cortex. Several copies of

---

[5] A nice discussion on this topic can be found in [21].

the homunculus can be found, some being related to somatosensory experience, others having a function in motor controlling.

The obvious question to ask is: what is the *function* of a neuronal map? One possible solution, more or less denying the question altogether, is that neuronal maps simply follow the *sensory surface* from their input modality. In this view, the visual layers, e.g., are retinotopically organized *because* they receive their input from the retina. It has been shown already in 1976 by Willshaw and Von der Malsburg [105] that layers of neurons can self-organize into maps under the influence of mutual interaction between the neurons making up the layers. Even if only a rudimentary map-like organization is present, the correlations in neuronal firing will establish a high-quality, fully developed map. In this way, the retina would impose its topography upon the visual processing layers, and the tonotopic organization of the auditory pathway would likewise be just a result of the frequency decomposition in the cochlea.

Still, the map-like organization of sensory information is more than just an epiphenomenon. This becomes clear by looking at sound localization in mammals. Experiments have shown that in early stages of the auditory pathway, sound source location is *not* encoded in a map (see [111, 130, 132, 165]). If an auditory stimulus is presented at different locations, the activity of the whole population of neurons increases or decreases. Instead of coding sound source location through the position of the activity maximum in the population, source location is coded through the total activity in the population. Nonetheless, multiple auditory maps are found in the mammalian brain [101]. If the mammalian brain takes the effort to explicitly construct a spatial map of auditory space, even though no map is initially given, some advantage can be assumed to arise from this.

There is indeed an advantage. The usefulness of a map-like organization of sensory input lies in coding efficiency. Generally, one can assume that neurons coding for related events or properties will be interconnected, either directly or indirectly. If neurons coding for similar locations in sensory space are near to each other, wiring costs are minimized. A beautiful example of this is the connection between sensory and motor maps. Motor neurons are often organized in maps, just like sensory neurons. In the superior colliculus (sc) the connection between the two maps has been studied in great detail.[6] Here, motor maps lie directly on top of the sensory input maps and are in spatial register. The sensory input is used to directly generate appropriate motor output, for example in the form of a gaze shift or eye saccade [96, 100, 101].

Another advantage of maps is found in multimodal integration, in which several sensory input modalities merge to form a unified map of multisensory space. This topic will be discussed in more detail in chapter 4.

---

[6] The sc is not the only brain region containing (spatial) maps, although it has been studied extremely well. Many (aligned) sensory and motor maps are also found in the cortex. These cortical maps are very important, especially in primates and "higher" mammals, and interest in cortical maps is increasing [86].
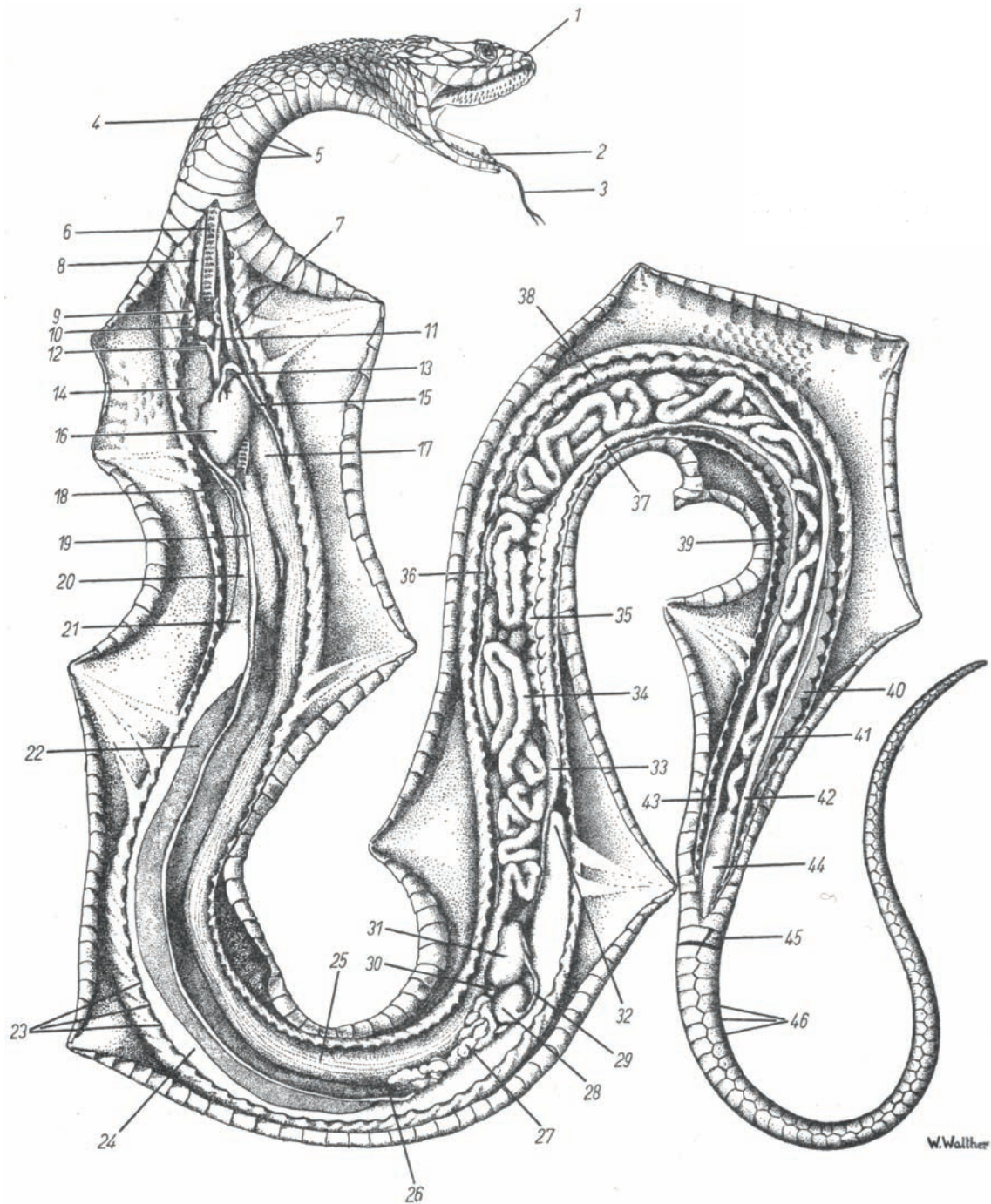
Lüdicke's magnificent review on snake biology was published in 1964 [205]. It counts 298 pages and contains the Gargantuan number of 2421 references. Although the work is of course somewhat outdated, it remains very worthwhile. Unfortunately, it was written in German, and no English translation is available. This figure shows the general anatomy of snakes.

*Now the serpent was more subtil than any beast
of the field which the LORD God had made.*

Genesis 3:1

2. Auditory localization of ground-borne vibrations in snakes

In this chapter, the detection and source localization of substrate vibrational waves by snakes is studied. Although snakes are often taken to be deaf, they can hear air-borne and substrate-based sound. Localization of the latter is possible because of the remarkable anatomy of the snake auditory periphery.[1]

2.1 Introduction

Snakes constitute a group of animals with remarkable sensory capabilities. In addition to vision and olfaction many snakes can detect infrared (IR) radiation. Snakes further possess specialized touch receptors distributed on the head, mainly around the jaws. This chapter focuses on the auditory system of snakes. In contrast to popular believe, snakes are not deaf. They can hear air-borne sound and respond to it. As demonstrated below, snakes are also able to detect substrate vibrations using their auditory system and even localize their source. It seems that the snake ear is in fact particularly well equipped to detect vibrational waves propagating along the surface it rests upon.

Before the snake auditory system will be discussed in section 2.2, a short overview of the most important snake sensory modalities is presented. Section 2.3 presents an analytical model of substrate-vibration reception and section 2.4 will discuss the localization of ground-borne vibrations.

2.1.1 Sensory systems of snakes

Vision

Many snakes depend heavily on visual information for orientation and feeding behavior [186, 188]. Especially in vipers, vision and infrared (IR) vision are important during striking. Evidence shows that hunting performance significantly drops if both vision and IR detection are blocked [191, 201, 202, 220]. Olfaction is important in alerting and post-strike behavior, but blocking of the chemosensory pathway has not as large an impact as blocking of (IR) vision has.

Although vision is not always essential for survival[2] visual input seems to be needed in young snakes for optimal functioning of the other sensory modalities [190, 191].

---

[1] The results presented in this chapter have been published together with Bruce A. Young and J. Leo van Hemmen [189].

[2] A much-cited article discusses an isolated population of tiger snakes [184]. These snakes are often rendered blind from seagull attacks, but survive nonetheless. This is generally taken as evidence for the non-essential role of vision, but—as the authors themselves showed later—the snakes can only survive because there is a large abundance of immobile and easy-to-catch prey in their mini-habitat [183].

The binocular overlap is typically 30º–40º [188]. This provides for reasonable depth estimation, which is of course needed for a successful strike. The eyelids are transparent and fused, such that the eye is always "closed". Focusing is not achieved through deformation of the lens, but rather by shifting it by increasing eye ball pressure [217].

Infrared vision

Perhaps the most spectacular sensory modality of snakes is IR vision. Two groups of snakes, pit vipers and boids, possess specialized organs to detect heat [207]. Infrared vision is used for thermoregulation [204] as well as for hunting [186, 187]. Recently, it was shown that squirrels use IR signaling to chase away hunting rattle snakes [213], which shows that IR vision is also used for interspecific communication.

The IR-radiation-detecting organs consist of grooves (in boids) or cavities (in pit vipers) on the head of the animal. Within the pit a heat-sensitive membrane is suspended. The sensitivity is so high that even temperature differences on the membrane in the order of mK can be detected [185]. To ensure a large enough influx of IR radiation, the aperture of the pit organ must be quite large. This results in a very poor optical quality of the organ; the heat-image on the detection membrane is strongly blurred.

There is an IR map in the snake optic tectum that is aligned with the visual map [197, 203, 208]. Experiments have shown that orientation to a heat source with an accuracy of about 5º is possible [209]. Snakes are thus able to use IR vision accurately in spite of the low optical quality of the pit organ. To achieve this, the snake must enhance the heat-image neuronally. It was recently shown that such an enhancement is indeed possible, thus resolving the paradox [216].

Cephalic touch receptors

In 1969, Proske discovered a specialized mechanoreceptor, which is only found on the facial scales of snakes [211, 212]. The receptors are especially sensitive to mechanical stimulation across the skin [199, 200, 211, 212] and are distributed mainly around the mouth of the animal. The response to a vibrating mechanical probe is strongly phase locked and responses are best for frequencies around a couple of hundred Hz.

The function of these receptors is presently unknown. Although they could hypothetically play a role in detection of substrate vibrations, this seems unlikely. The number of receptors varies greatly between species and even shows large variation within species [198]. *Cerastes cerastes*, the only snake for which behavioral responses to surface vibrations have been demonstrated explicitly, does hardly possess any facial touch receptors (Bruce A. Young, personal communication). The most likely role for these receptors is to assist the snakes in mechanosensory tasks such as positioning the head with respect to prey just before eating it.

Olfaction

Snakes possess two separate chemosensory organs [192, 210]. Air-borne odors are picked up through the nostrils. Less volatile agents can be detected through the vomeronasal organ. The tongue is used to pick up non-volatile molecules during flicking. Following tongue retraction into the mouth, the molecules are deposited onto two paths in the oral cavity. When the mouth is closed, the paths deliver the molecules to the vomeronasal organ through a pair of openings in the roof of the mouth.

It has been proposed that the forked tongue enables snakes to smell "in stereo", the right tip picking up a different odor concentration than the left tip [215]. In this way, scent gradients could be detected which would be especially helpful during trace following. However appealing this idea might be, it is unfortunately wrong. The tongue tips often touch during retraction into the mouth and this would eliminate any spatial chemosensory information.

Generally speaking, the sense of smell is very important in snakes. Especially before prey capture (alertness, trace following) and after striking chemosensory information is used [186, 188].
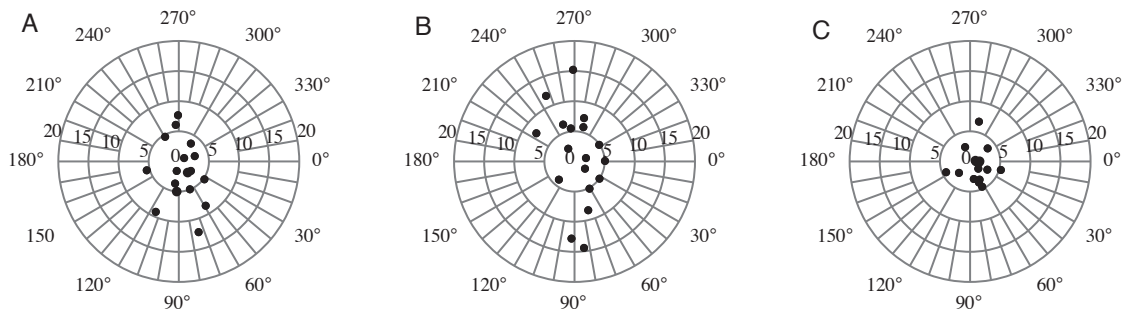
Figure 2.1: *Localization experiments performed by Young and Morain [220]. Strike performance for a number of strikes. The snakes lies with its head at the center and the dots indicate direction and distance of successful strikes. A) Control group; B) strikes following denervation of the olfactory and vomeronasal nerves; C) strikes following denervation and occlusion of both eyes.*
From a comparison between B and C it is clear that vision is an important modality in guiding the strike; the striking distance drops, which indicates less "confidence" on the snake's part. Nonetheless, vision is not absolutely necessary for strike guidance. In fact, no strikes occurred in which the prey was missed altogether. This demonstrates that in absence of all but vibratory cues, Cerastes can reliably detect and strike prey.

In contrary to the sense of IR or normal vision, it is not possible to directly derive spatial information from chemosensory clues. This makes it very difficult for most snakes to hunt if IR and normal vision are not available.

2.2 Snake auditory system

2.2.1 Experimental evidence of snake hearing

Although snakes are often considered to be deaf there is ample evidence that snakes can hear (extensively reviewed in [219]). One of the main experimental difficulties is that snakes often do not seem to respond to air-borne sound, which does by itself not necessarily imply deafness. This difficulty can be coped with if physiological experiments are performed rather than behavioral studies. Especially Wever [218] and Hartline [193, 194, 195, 196] have devoted many physiological studies to snake hearing.

The results of these studies univocally show that snakes can hear. Wever measured cochlear potentials in response to sound and vibration and Hartline has measured midbrain responses to sound and vibration. Both authors found that snakes are reasonably sensitive to air-borne sound. Furthermore, a very high sensitivity to vibration of the head or substrate vibration was demonstrated.

2.2.2 Substrate hearing hypothesis

Although Hartline and Wever found a high auditory sensitivity to head vibrations, they both dismissed the idea that this type of hearing is important. There is a clear anatomical route connecting the snake's lower jaw to the inner ear via the quadrate and columella bones, but the possibility that the snake could pick up any *relevant* auditory clues from the substrate was nonetheless set aside. Wever commented ". . . the critical question is to what extent are the more important events in the environment represented in ground vibrations?"

The believe that substrate vibration is not important was proven false by Young and Morain [220]. In their experiments, Young and Morain showed that the Saharan sand viper *Cerastes cerastes* can localize its prey using ground-borne vibrations only (Fig. 2.1). Although vision plays
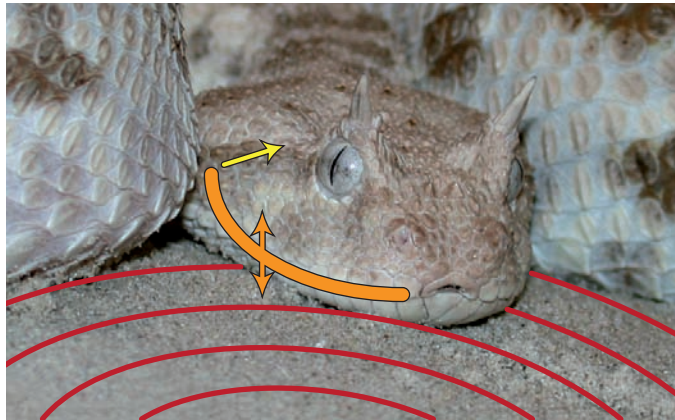
Figure 2.2: *Hunting position of* Cerastes cerastes. *The animal lies slightly buried or just on top of the substrate. Sand waves reach the lower jaw of the snake and are conducted into the inner ear. Photograph taken by Richard Mastenbroek.*

a dominant role during foraging, blocking of the visual and olfactory pathway[3] did not prevent the snake from striking and catching its prey. The experiments showed very clearly that vibration was the dominant cue in this case and a strike was often launched directly after a vibratory event caused by prey motion.

Since the lower jaw is linked to the cochlea through a chain of bones (section 2.2.4), substrate vibrations can be directed into the inner ear of the snake. This pathway was already described in the classical work on snake biology by Lüdicke [205]. *Cerastes* typically lies with its head slightly buried in the sand during hunting (Fig. 2.2), maintaining firm contact with the substrate and enabling maximal sensitivity to surface vibrations.

2.2.3 Auditory sensitivity

Wever and Hartline have independently measured the auditory sensitivity of snakes [193, 194, 195, 196, 218]. Both authors paid mainly attention to the reception of air-borne sound. Three key findings can be distilled from their work.

1. Although there is no obvious mechanism for impedance matching (see section 2.2.5), snakes do have a reasonable sensitivity to air-borne sound. The hearing threshold at best frequency is about 20 dB higher compared to most mammals or birds at that frequency (Fig. 2.3).

2. The sensitivity range of the snake auditory system is very limited. A clear sensitivity maximum is found around 300 Hz and sensitivity falls very sharply away from the minimum at about 20 dB/octave (Fig. 2.3). This means that for every frequency doubling or halving, starting at the best frequency, the just-noticeable sound intensity increases hundredfold. Interestingly, the threshold of snake hearing matches the transmission characteristics of sand (see section 2.3.2).

3. Both authors found a striking sensitivity to vibration of the head, lower jaw or quadrate bone. A maximal vibration sensitivity of about 1 Å was obtained in the experiments. This sensitivity is comparable to the sensitivity of a vibration detection specialist like the sand scorpion [227]. The frequency dependence of the sensitivity follows a similar profile as the sensitivity to air-borne sound. The maximal sensitivity is found around 300 Hz and the sensitivity decreases rapidly away from this best frequency.

---

[3] *Cerastes* does not have IR-detecting pit organs.
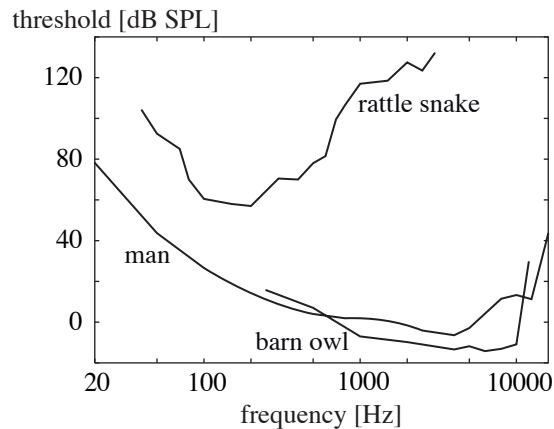
threshold [dB SPL]

Figure 2.3: *Comparison of hearing threshold for man, barn owl and rattle snake (air-borne sound). The hearing capabilities of mammals and birds are generally much better than those of reptiles. In addition to the limited range of sensitivity, the absolute hearing threshold is much higher in snakes than in the other groups. The pronounced sensitivity maximum around* 200 Hz *lies squarely in the range of frequencies that are transmitted well in sand. Data taken from [124, barn owl], [168, man], and [218, rattle snake].*

2.2.4 Ear anatomy

The hearing apparatus of snakes is substantially different from that of mammals or even that of many other reptiles. Snakes do not possess an external ear opening or tympanic membrane, or any other superficial indications of a functional auditory organ [218].

Middle ear

The middle ear of snakes is considerably simpler than that of mammals. The mammalian middle ear basically consists of a cavity in which the three hearing ossicles are suspended [125]. The malleus (hammer) is connected to the inner side of the tympanic membrane and, on its other end, to the incus (anvil). The incus is linked to the stapes (stirrup) which in turn connects to the oval window, the entrance to the cochlea. In snakes the situation is quite different (Fig. 2.4). The stapes (also called columella) connects to the cochlea at one end, but the other end is linked to the relatively large quadrate bone. This bone forms itself the link between the skull of the animal and the lower jaw. Though the osseous jaw-quadrate-stapes chain the inner ear can thus literally hear movements of the lower jaw. In fact, the mammalian hearing ossicles are homologous to the reptilian jaw complex bones, the reptilian quadrate corresponding to the mammalian incus [206].

To enable the snake to swallow large prey, the two halves of the lower jaw are not rigidly linked, but connected only through flexible ligaments. During feeding, both halves of the lower jaw can be dislocated. This implies that the right and left sides of the lower jaw can vibrate independently of each other. In this way stereo hearing of surface vibrations is possible. This is very important, since it enables the snake to locate incoming vibrational waves through the interaural time-of-arrival difference (ITD), as discussed in section 2.4.

A possible problem in detecting jaw vibrations is the fact that the stapes is coupled to the quadrate through a soft-tissue ligament. How can vibration propagate from quadrate to stapes without losing much of its energy? In fact, this problem is not unique to the snake hearing pathway. In mammals, the incus is coupled to the stapes through a flexible ligament as well [125]. Hearing, however, generally takes place at relatively high frequencies ($\gtrsim 100\,\text{Hz}$). At these frequencies the connection between quadrate and stapes may well behave stiffly [261].
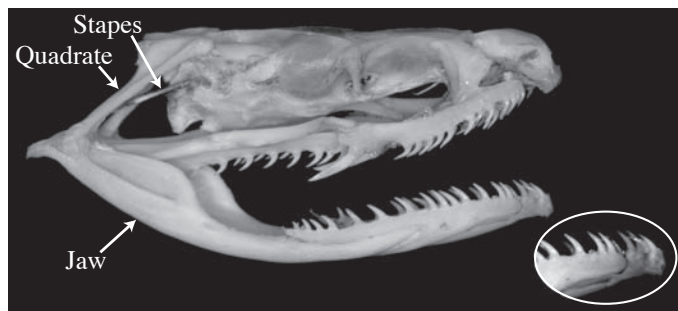
Figure 2.4: *Anatomy of the snake auditory system (here the skull of a red-lipped snake* Crotaphopeltis hotamboeia*). Snakes lack a tympanic membrane and the stapes is coupled to the quadrate bone instead. Through the quadrate, the stapes is coupled to the lower jaw. The inset shows that the two halves of the lower jaw are not rigidly coupled, but can move independently. This is of great importance since it enables the snake to hear substrate vibrations in stereo. Specimen from Zoologische Staatssammlung München.*
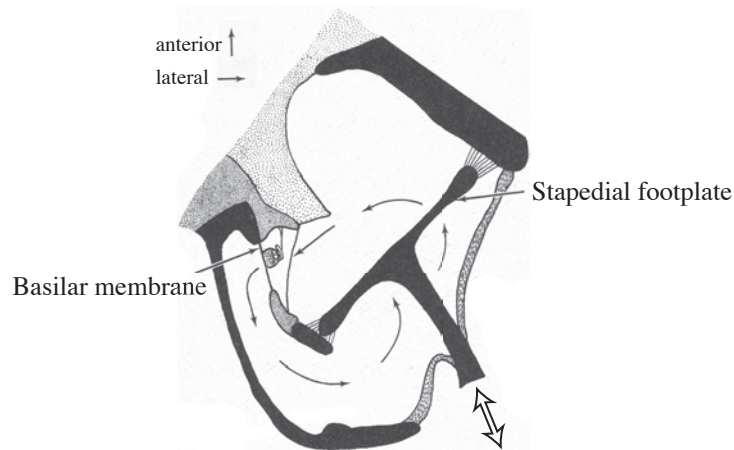
Figure 2.5: *The reentrant fluid circuit is illustrated by this top view of the snake cochlea. Movement of the stapes (indicated by the double arrow) pushes the cochlear fluid through the circular path connecting upper and lower side of the stapedial footplate. The basilar membrane, stretched across the pathway, vibrates with the fluid such that the hair cells are activated. Image adapted from [218].*

Although there is no external ear present, limited sensitivity to air-borne sound is still present in snakes. Much of the incoming sound intensity is simply reflected, but part of the energy can be converted into motion of the quadrate, which in turn drives the stapes.

Inner ear

The inner ear of snakes is also quite remarkable [218]. The stapes enters the cochlea through the oval window, but a round window functioning as a pressure outlet is lacking. There is no need for such an outlet, since the stapedial footplate lies completely within the perilymphatic fluid. The cochlear fluid in front of the footplate is connected by a circular path to the fluid at the back of the footplate. Motion of the footplate does therefore not lead to a build-up of pressure. This reentrant circuit is illustrated in Fig. 2.5.

The basilar membrane is suspended within the fluid and follows its motion. On the membrane, there are only a couple of hundred hair cells generating the neuronal auditory response. The basilar

membrane does not seem to have a strong frequency selectivity, as is the case in mammals.

2.2.5 The impedance matching problem

The (acoustical) impedance Z of a medium defines the relation between pressure and particle velocity in that medium. For a plane monofrequent sound wave propagating in the positive x-direction the pressure and the particle velocity both vary harmonically:

$$p = |p| \, e^{i(\omega t - kx)} \tag{2.1a}$$

and

$$v = |v| \, e^{i(\omega t - kx)} \, . \tag{2.1b}$$

The impedance is defined as

$$Z = \frac{p}{v} \, . \tag{2.2}$$

In a medium with a low acoustical impedance, such as air, a small pressure leads to large particle velocities. If the impedance is large, on the other hand, a high pressure must be applied to invoke substantial particle movement.

On the boundary between two media with differing acoustical impedances part of the incoming wave will be reflected. Imagine a sound wave traveling from a medium (1) with low impedance into a medium (2) with a high impedance. At a given pressure p_1, the particles in the first medium will move with a velocity v_1. Since the particle velocity must be continuous across the boundary between the media, the relation $v_2 = v_1$ must hold. Since the impedance in the second medium is higher, $|p_2| > |p_1|$ is also satisfied. This leads to an inconsistency, since the pressure must be continuous across the boundary as well as the velocity.

To solve this paradox, it is necessary to assume that part of the incoming wave is reflected. This results in a higher pressure $|p_1|$ at the first side of the boundary and at the same time, the net particle velocity $|v_1|$ is reduced. The continuity requirement for pressure and velocity leads to an expression for the fraction of the incoming energy that is transmitted (α_t) or reflected (α_r) [163].

$$\alpha_t = \frac{4Z_1 Z_2}{(Z_1 + Z_2)^2} \, , \qquad \alpha_r = \left(\frac{Z_1 - Z_2}{Z_1 + Z_2} \right)^2 \, , \qquad \alpha_t + \alpha_r = 1 \, . \tag{2.3}$$

For an infinite, homogeneous, and isotropic medium the acoustic impedance is given by the product of medium density and the speed of sound $Z = \rho c$. From this definition, it is clear that water has a much larger acoustic impedance than air, since both propagation velocity and density are significantly higher. Animal tissue consists for a large part of water and therefore, it is to be expected that incoming aerial sound waves will be reflected to a large extend.

One of the key problems that any ear must solve is therefore how to direct as much incoming sound energy into the cochlea. In reality, the cochlear impedance is not quite so high as that of (salt) water, since finite-size and shape effects must be taken into account here. Still, the resulting cochlear impedance, which can be calculated as well as measured, is approximately 360 times as high as that of air (see discussion in [151, p. 16]). This implies that only $\pm 1\%$ of the incoming sound energy would make it into the cochlea without some sort of impedance matching mechanism.

In mammalian ears, the impedance matching problem is solved by linking the tympanic membrane to the cochlea through a chain of ossicles (see previous section). The last ossicle, connected to the cochlear fluid, has a much smaller surface area than the tympanic membrane. This mechanism increases the pressure of incoming sound waves to match the pressure needed to effectively induce motion in the cochlear fluid [125, 126]. In addition, the ossicles introduce a small leverage, which helps to increase cochlear fluid motion amplitude.

In snakes, there is no such mechanism. Although the lateral surface of the quadrate has a much larger area than the footplate of the stapes, much of the incoming sound intensity will

still be reflected by the outer tissue layer of the snake's head. Surface-based hearing provides a good opportunity to circumvent the impedance matching problem and the snake ear seems to be optimally adjusted to exploit this option.

2.3   Detection of ground-borne vibrations

2.3.1   Use of surface vibration for communication

The use of surface vibration for communication occurs quite frequently in the animal kingdom [235]. Especially insects often use substrate vibration [229]. The most frequently used transmission channel is constituted by plant leaves [223, 242, 246].

As transmission channels, plant leaves are very efficient. In three dimensions, the intensity of an isotropic signal decreases with the square of the distance to the source. In two dimensions, the intensity decreases only with the first power of distance. On leaves, however, vibration propagation is often effectively almost one-dimensional, since the vibration is mainly transmitted along the length of the leaf. Geometrical intensity loss due to spreading is then minimal.

The water surface [171, 173] or the silk of spider webs [239, 245] form other substrates for vivid intra- and interspecific communication. In desert or other sandy environments, the sand itself is often used as a communication channel. Many cases of the use of sand-based vibrational communication have been documented. Sand vibration is for example used by the sand-swimming lizard *Scincus scincus* [233, 234], which plunges its head into the sand to "listen" for burying prey. Further examples are provided by antlions [230], and scorpions [228, 253].

A particularly interesting case is the use of honeycomb vibration for interspecific communication in bees. The special physical properties of the hexagonal cells of the honeycomb allow for long-range communication inside the crowded hive [247, 251, 254].

Although most examples of communication through surface vibrations involve arthropods, several studies demonstrated the use of vibrational communication by small mammals (see [243] for a review, or [241] for a recent example). Kangaroo rats seem to use vibrations to scare away snakes and warn each other of the danger [249, 250]. Frogs also seem to use seismic signaling [240] and even elephants are thought to make use of vibratory signals [248].

In light of the discussion above, it must not come as a surprise that snakes are able to detect and use surface vibrations as well. It is well-known that many snakes and other reptiles that live on a sandy substrate can navigate through the surface layer of sand and catch hiding prey (see e.g. [214]). The question than must be answered, however, is *how* they manage to do so.

2.3.2   Propagation of surface waves along a sandy substrate

Although many researchers have demonstrated the use of sand-surface vibration by desert animals, there is surprisingly little known on the propagation of sand waves. Although there is a large body of literature on wave-propagation in granular matter, this literature is mainly concerned with relatively small systems, consisting of perhaps a few dozens of grains in every direction (see for example [236, 237, 238]).

The typical diameter of a sand grain is about 250 μm and even for small distances in the order of a few cm, there are hundreds or even thousands of grains involved in vibration propagation. Experimental and theoretical results for "small" systems of granular matter suggest that the precise configuration of the grains is very important for the propagation of vibrational waves. Intuitively, one would expect that on length scales much larger than the typical grain size, a continuum description of wave propagation should be applicable. Indeed, if the motion amplitude of individual grains is much smaller than the length scale of interest (e.g. the wave length), a continuum description can be used and the movement of individual grains can be ignored [222].

There are two papers describing the propagation of vibrational waves in sand on a scale of several tens of cm [221, 226]. The results presented in these papers imply that a continuum description is indeed possible. If the sand surface is slightly disturbed, approximately 70% of the energy propagates away from the source in the form of Rayleigh waves [231] running along the surface. The remaining 30% is carried away by volume waves propagating into the sand.

Small-amplitude Rayleigh waves behave similarly to water surface waves [231], the sand particles carrying out an elliptic motion that is attenuated exponentially with depth. The wave propagation velocity v_{Ray} is low, about 45–50 m/s. Because of strong attenuation at high and low frequencies, the frequency spectrum of Rayleigh waves peaks below 1000 Hz. Typically, maximum transmission takes place around a few hundred Hz. Together, these results give a wavelength λ in the order of 10 cm, which is indeed much larger that the typical sand grain size ($\sim 250\,\mu$m) or the typical motion amplitude ($\sim 1\,\mu$m).

Prey-generated waves can thus be treated as disturbances propagating through a continuous and homogeneous medium. Actually, since Rayleigh waves behave much the same as water waves it is possible to use methods from naval engineering to calculate the response of the lower jaw resting on the sand to incoming vibration.

2.3.3 Vibrational response of the lower jaw

The next step is now to estimate the lower jaw's response to incoming surface waves. In so doing, three assumptions are made.

1. The substrate is treated as a continuous medium, see the discussion in section 2.3.2 above.

2. The two sides of the lower jaw are modeled as two bodies (cylinders) resting on the surface and moving *independently* of each other. Techniques from naval engineering [259] can then be used to calculate the motion response to incoming surface waves.

3. The Rayleigh wave is not altered much by passing the snake head. This assumption is justified since the wave length is much larger than the head size of the snake so that bending and refraction effects can be ignored.

Figure 2.6 shows the geometry of the problem. Jaw motion can be decomposed into six components. Vertical motion (heave and pitch) should be especially effective in eliciting auditory responses (compare Fig. 2.4). The other four components will not contribute significantly to the auditory input and will be ignored in the following.

The coupled equations of motion (EOMs) describing heave u and pitch ψ are [259]

$$
\begin{aligned}
M\ddot{u} &= \int \mathrm{d}x \; f(x,t,u,\psi) \\
M &= \int \mathrm{d}x \; m(x)\,,
\end{aligned}
\qquad \text{[heave]} \qquad (2.4a)
$$

$$
\begin{aligned}
J\ddot{\psi} &= \int \mathrm{d}x \; (x-\bar{x})f(x,t,u,\psi) \\
J &= \int \mathrm{d}x \; (x-\bar{x})^2 m(x)\,.
\end{aligned}
\qquad \text{[pitch]} \qquad (2.4b)
$$

The coordinate x runs along the length of the jaw and $\bar{x}$ is the jaw center of mass (COM). Since the jaw is a *slender* body, an effective one-dimensional description can be used. M and J denote the total jaw mass and moment of inertia, respectively, and $m(x)$ designates the cross-sectional mass density as a function of position x along the jaw.
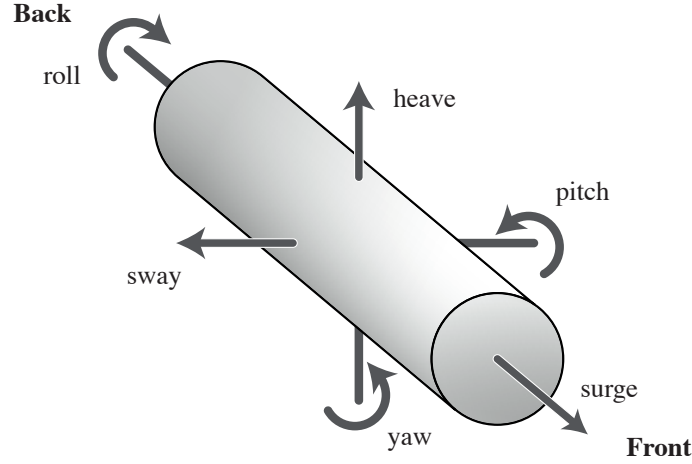
Figure 2.6: *Motion of the lower jaw halves can be decomposed into six components: linear motion along three orthogonal axes and rotation about these axes. Especially motion leading to vertical displacement of the cylinder tip (heave and pitch) is effective in stimulating the cochlea through the attached stapes.*

The force f acting on the jaw is given as a function of the difference between sand surface displacement h_{sand} and jaw displacement h_{jaw},

$$
\begin{aligned}
f &= m_H(x)\ddot{\tilde{h}} + n(x)\dot{\tilde{h}} + c(x)\tilde{h} \,, \\
\tilde{h} &= \tilde{h}(x,t) = h_{\mathrm{sand}} - h_{\mathrm{jaw}} \,.
\end{aligned}
\tag{2.5}
$$

The three terms in the expression for the force density f describe inertia, friction, and buoyancy, respectively. The prefactor m_H is called the *hydrodynamic mass density*, and is determined geometrically from the cross-sectional shape and mass distribution of the floating body under consideration. For a homogeneous cylinder the hydrodynamic mass density equals the ordinary mass density ($m_H = m$) and for a large variety of other cross-sectional shapes the approximation $m_H \approx m$ holds.

The surface wave elevation h_{sand} along the jaw is

$$
\begin{aligned}
h_{\mathrm{sand}} &= a_{\mathrm{sand}} \cos(\mathbf{k} \cdot \mathbf{x} - \omega t) \\
&= a_{\mathrm{sand}} \cos(kx \cos\beta - \omega t)
\end{aligned}
\tag{2.6}
$$

with $\mathbf{k}$ being the wave vector of the surface wave, $k = 2\pi/\lambda$ the wave vector magnitude, β the wave angle of incidence with respect to the jaw's long axis, a_{sand} the amplitude, and ω the wave angular frequency.

The jaw movement as a function of heave u and pitch ψ is given by

$$
h_{\mathrm{jaw}} = u + (x - \bar{x})\psi \,.
\tag{2.7}
$$

To solve the system (2.4),(2.5) a harmonic *ansatz* for the heave and pitch response is taken,

$$
\begin{aligned}
u &= a_u \cos(\epsilon_u - \omega t) \,, \\
\psi &= a_\psi \cos(\epsilon_\psi - \omega t)
\end{aligned}
\tag{2.8}
$$

where the amplitude $a_{u/\psi}$ and phase $\epsilon_{u/\psi}$ of the response are to be determined. Note that the dimension of a_u is that of a length, while a_ψ is dimensionless.

Substituting (2.6) and (2.7) into (2.5) shows that every time derivative introduces a factor ω into (2.5). Since the frequency content of the incoming wave is peaked between 200 and 1000 Hz, the force equation will be strongly dominated by the inertia term and one obtains $f \approx m_H \ddot{h}$. In addition, friction and buoyancy terms must necessarily be small as compared to inertia. This is because the amount of friction and buoyancy depend directly on the jaw motion amplitude. This amplitude is much smaller than the total dimension of the jaw, which determines the inertia.

To make the estimate of the jaw-motion response explicit, a cylindrical shape for the two sides of the lower jaw is assumed. This results in a constant cross-sectional mass density

$$
\begin{aligned}
m_H &= m \\
M &= mL \\
J &= mL^3/12
\end{aligned}
\tag{2.9}
$$

with L as the length of the jaw. The COM lies at the origin ($\bar{x} = 0$) so that the integrals in (2.4) run from $-L/2$ to $L/2$. Furthermore, $\xi := (kL\cos\beta)/2$ is defined. Substituting everything into (2.4) gives

$$
\begin{aligned}
\frac{a_u}{a_{\text{sand}}} \cos(\epsilon_u - \omega t) &= \frac{\sin\xi}{2\xi} \cos(\omega t)\,, \\
\frac{a_\psi}{a_{\text{sand}}} \cos(\epsilon_\psi - \omega t) &= \frac{3(\sin\xi - \xi\cos\xi)}{L\xi^2} \sin(\omega t)\,.
\end{aligned}
\tag{2.10}
$$

Since the above equations must hold for all times t the amplitudes and phases must obey

$$
\frac{a_u}{a_{\text{sand}}} = \frac{\sin\xi}{2\xi}\,, \qquad \frac{a_\psi}{a_{\text{sand}}} = \frac{3(\sin\xi - \xi\cos\xi)}{L\xi^2}\,,
$$
$$
\epsilon_u = 0\,, \qquad\qquad \epsilon_\psi = \pi/2\,.
\tag{2.11}
$$

Using (2.7) and (2.8), the deflection of the jaw tip, where $x = -L/2$ is

$$
h_{\text{jaw}} = a_u \cos\omega t - \frac{L}{2} a_\psi \sin\omega t\,.
\tag{2.12}
$$

The relative amplitude of the deflection at the end of the jaw is then

$$
\begin{aligned}
\frac{a_{\text{jaw}}}{a_{\text{sand}}} &= \sqrt{\left(\frac{a_u}{a_{\text{sand}}}\right)^2 + \left(\frac{L}{2}\frac{a_\psi}{a_{\text{sand}}}\right)^2} \\
&= \sqrt{\frac{9\xi^2\cos^2\xi + (9 + \xi^2)\sin^2\xi - 9\xi\sin 2\xi}{4\xi^4}} \\
&= \frac{1}{2} + \frac{\xi^2}{6} + \mathcal{O}\left(\xi^4\right)\,.
\end{aligned}
\tag{2.13}
$$

Typical parameter values are given in table 2.1. For these values, $|\xi|$ lies between 0 and 0.6, depending on the input angle β, so that an expansion in terms of ξ is permitted. From (2.13) it follows that the lower-jaw amplitude would be about half that of the incoming surface wave. Since the auditory system is sensitive to jaw movement down to Å amplitudes, prey detection using the jaw-quadrate-stapes pathway would be not only possible, but even reasonably efficient.

2.4 Neuronal processing of auditory information

2.4.1 Cochlear response to vibration

The next question that must be answered is what the cochlear response to the incoming vibrational signal looks like. This information is needed to numerically simulate the localization process in

parameter	value
physical parameters	
Rayleigh wave speed	$v_{\text{Ray}}=45\,\text{m/s}$
wave length	$\lambda=15\,\text{cm}$
input angular frequency	$\omega=2\pi\cdot300\,\text{Hz}$
jaw length	$L=3\,\text{cm}$
inter ear distance	$d=3\,\text{cm}$
maximal input ITD	$\text{ITD}_{\text{max}}=667\,\text{μs}$
simulation parameters	
number of cochlea neurons	$N_{\text{cochlea}}=75$
cochlear firing rate	$A=250\,\text{Hz}$
cochlear phase locking strength	$\text{VS}=0.9$
number of map neurons	$N_{\text{map}}=100$
ITD range of map neurons	$\text{ITD}_{\text{map}}\in[-1.33,1.33]\,\text{ms}$
map neuron time constant	$\tau_m=500\,\text{μs}$
map neuron capacitance	$C_m=1$
map neuron resting potential	$V_r=0$
map neuron reset potential	$V_{\text{reset}}=V_r=0$
map neuron threshold	$V_\theta=1$

Table 2.1: *Parameters used in both analytical calculations and computer simulations. The time constants chosen here are typical for the auditory system [156]. The model is quite robust against parameter variation (see also Fig. 2.8).*

the snake's brain. There are no experiments to clarify this matter, but a good model of the signal can be built using two defining characteristics: *spike timing* and *temporal accuracy*. As soon as the cochlear neurons fire, all details about the mechanical input are lost, except for these two properties.

The intensity of the signal could be different at the right and left cochlea. However, measurements have shown that damping of sand-surface waves is very small. Geometrical spreading does of course diminish the amplitude of the surface waves, but if the source distance is more than a couple of cm, the wave front is nearly planar and geometrical spreading can be neglected. Therefore, the signal amplitude may be taken to be equal for the right and left ear.

Due to the interaural distance, the signal will arrive at the right and left cochlea at different times. The resulting interaural time difference (ITD) as a function of the input angle β is given by

$$\text{ITD}(\beta) = \frac{d\sin\beta}{v_{\text{Ray}}}\ . \tag{2.14}$$

Here, d is the interaural distance (or rather, the distance between the COM of the right and left jaw halves) and v_{Ray} is the Rayleigh wave speed as discussed above. The input angle β is the angle between the wave vector of the incoming surface wave and the long axis of the head. The ITD is the only difference between the signals arriving at the right and left ear. Therefore, ITD must be used for binaural source localization.

The other important signal characteristic is the temporal accuracy, or phase locking strength. Although it is unclear how the response of the cochlear neurons to the incoming vibration behaves, it is bound to be periodical with a frequency corresponding to that of the surface wave. Neuron firing is of course noisy, so every neuron will spike at a preferred phase of the input, but the precise timing of the spike will vary and sometimes zero or multiple spikes may be fired within a single cycle. The amount of jitter in the spiking times can be quantified by the vector strength (VS, discussed in section 1.4).

Motivated by these considerations, the cochlear neurons are modeled as stochastically firing Poisson neurons (see appendix B.2.1). The right and left cochlea contain $N_{\text{cochlea}} = 75$ neurons. The time-dependent firing rate of the right population is given by

$$\lambda_R(t) = \frac{A \exp\left[-(\phi_R)^2/2\sigma^2\right]}{\sqrt{2\pi}\sigma \, \text{erf}(\pi/\sqrt{2}\sigma)} \tag{2.15a}$$

and the left population fires at a rate

$$\lambda_L(t) = \frac{A \exp\left[-(\phi_L)^2/2\sigma^2\right]}{\sqrt{2\pi}\sigma \, \text{erf}(\pi/\sqrt{2}\sigma)} \; . \tag{2.15b}$$

The error function (see p. 82) is denoted by "erf" and the normalization factor in the denominator is chosen such that A is the firing rate of a cochlear neuron in spikes per second. The input phase at right and left ear is given by ($-\pi \leq \phi_{R/L} < \pi$)

$$\phi_R = (\omega t)_{\text{mod } 2\pi} \; , \quad \phi_L = [\omega(t + \text{ITD}(\beta))]_{\text{mod } 2\pi} \; . \tag{2.16}$$

Equations (2.15) and (2.16) mean that, depending on the input phase, the firing probability peaks during every cycle of the incoming wave. The phase difference $\phi_R - \phi_L$, determining the timing difference between R and L ear, is given by the ITD between R and L depending on the angle of incidence β.

The parameter σ in (2.15) determines the phase locking of the cochlear neurons and can still be varied. A large value of σ causes broad peaks and implies imprecise firing whereas for a small value of σ the cochlear neurons respond very precisely to a periodic input signal. Using Eq. (1.20) gives the exact value of VS for any given $\sigma \in [0, \infty)$. By tuning σ it is possible to give VS any value between 0 and 1.

Typical values of the phase locking strength have not been measured in snakes, but for lizards the value is known to be larger than 0.9 at low frequencies [146]. In barn owls, VS is even higher [139]. A conservative value of VS = 0.9 is taken in the numerical simulations.

2.4.2 Modeling sound source localization

Once auditory information has been processed by the cochlear hair cells in left and right ear, with a given ITD determined by prey direction β, their phase-locked spikes are sent to the torus semicircularis, where signals from left and right ear come together. A reasonable mechanism for sound localization is constructing a neuronal map of auditory space based on ITD cues, as suggested by Jeffress [136].

This scheme is attractive because of its simplicity and experimental evidence provided by multiple groups of terrestrial vertebrates, including other Diapsid reptiles and their evolutionary descendants [116, 117, 138, 141, 145]. In the Jeffress scheme the auditory input from both cochleas is relayed to a set of map neurons along axonal delay lines (Fig. 2.7).

The map neurons are topographically organized. If a stimulus ITD at the ears is exactly compensated by the axonal delay difference, the map neuron receives *simultaneous* input from both ears and will fire at a maximal rate. If its delay does not match the input ITD, the neuron does not receive coincident input and its firing rate is low(er). Consequently every map neuron is tuned to a *specific* ITD and thus to a specific input direction. The bilateral pathways between ears and map neurons have fixed axonal delays that can effectively be ignored.

In the original model, Jeffress proposed two delay lines coming from the ipsi- and contralateral ear and running in opposite directions (see also the frontispiece to chapter 4 at p. 50). Here, a *pseudo*-Jeffress model is used in which only the contralateral input is delayed and the ispsilateral input arrives simultaneously at all map neurons. Both models have been found in birds [141], and the difference between the models is immaterial for the results in this chapter.
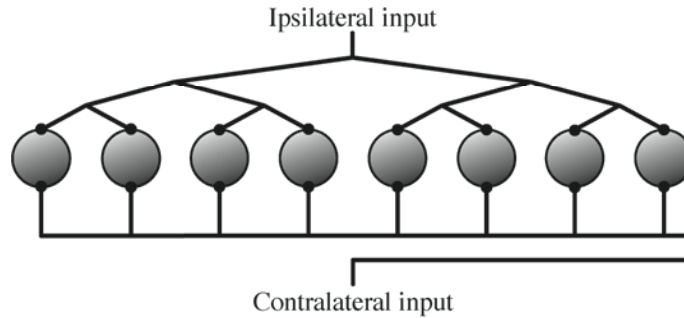
Figure 2.7: *(Pseudo-)Jeffress model of auditory localization. Neurons in the torus semicircularis receive input with a fixed axonal delay from the ipsilateral ear and an axonal-distance-dependent delay from the contralateral ear. The* ITD *is determined by input direction. Through variable delays, different neurons are tuned to different directions [136]. In each brain half, the neurons in the torus semicircularis code for a range of directions from 0° (frontal) to ±90° (ipsilateral). Together, the maps in both brain halves form a complete representation of auditory space.*

The map neurons (Fig. 2.7) are modeled as leaky integrate-and-fire neurons (see appendix B.1.1). The parameters used for the map neurons are given in table 2.1. The input current I_{inject} to the map neurons consists of the sum of excitatory postsynaptic currents (EPSCs) from the cochlear neurons; that is, from (2.15) and (2.16). Every input spike arriving at a synapse between a cochlear neuron and a map neuron leads to an EPSC (ε) in the form of an α-function with synaptic time constant τ_s and weight J

$$\varepsilon = J\alpha(t, \tau_s) \, . \tag{2.17}$$

Simulation results are shown in Fig. 2.8. The number of output spikes of the map neurons in a time interval of 250 ms is color coded. The firing rate is maximal if a map neuron's ITD corresponds to the ITD of the input signal but tuning is quite broad. Many map neurons encoding an ITD roughly matching that of the input respond with a fairly high firing rate.

To estimate the input ITD from the firing rate of the map neurons the rate-weighted mean of the map neuron ITDs is calculated. This is another example of vector coding, as discussed in section 1.4. The estimate comes close to the actual value of the input ITD. For several parameter values the rms error (E_{RMS}) of the ITD estimate varies from 19.5–38.4 µs, corresponding to 1.7°–3.3° in front of the animal. All parameter values match typical values found in auditory systems and parameter tuning is not necessary to achieve satisfying results.

It must be noted that because of the wide tuning curves, it is needed to extend the range of ITDs coded for by the map neurons well beyond the limits of the maximally encountered ITD, given by $\mathrm{ITD}_{\mathrm{max}} = \pm d/v_{\mathrm{Ray}}$. Only then is an accurate estimate possible for ITDs close to $\mathrm{ITD}_{\mathrm{max}}$.

2.5 Discussion

The work discussed in this chapter has shown that detection of surface vibrations in snakes is possible through the pathway of interconnected jaw and ear bones. Although the presence of this pathway has been known to anatomists, no-one has ever tried to analyze the mechanics of this pathway. Furthermore, the jaw-quadrate-stapes pathway has often been thought of as merely a detection device, signifying the presence of a vibration source at the sand surface. It is now clear that the pathway is much more. In addition to detection, precise vibration source localization is possible.

The crucial property of snake anatomy that enables localization is the separation of the right and left halve of the lower jaw. Because of this separation, input to the right and left ear is independent. This is a necessary condition for sound localization. The separation of the lower jaw
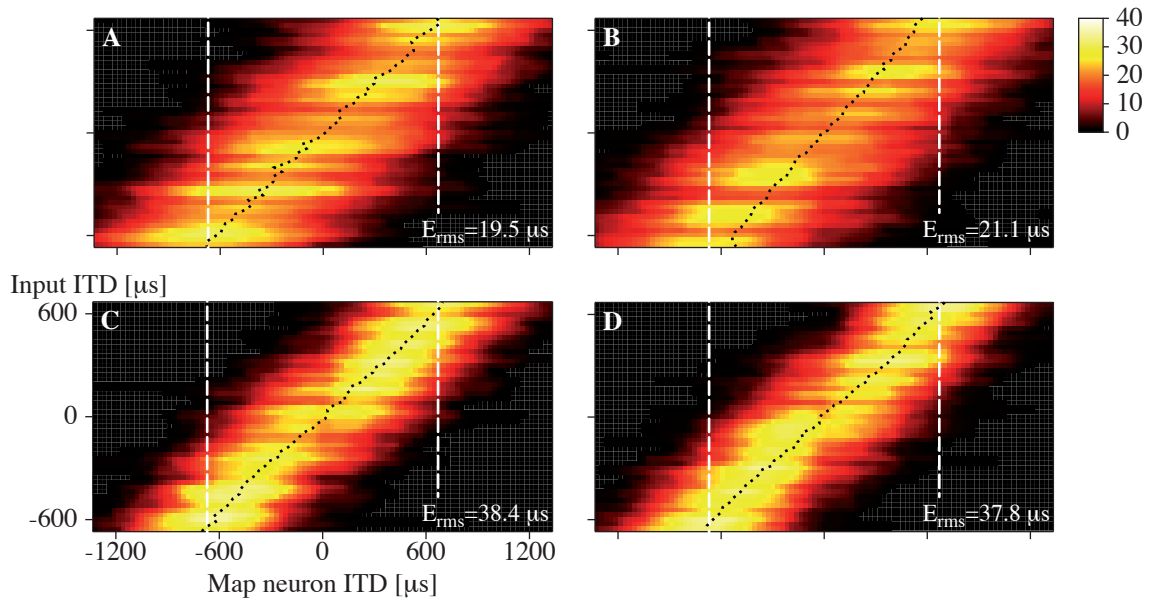
Figure 2.8: *Localization results for several parameter sets. For each input* ITD *and each map neuron, the firing rate is color coded. The black dotted line gives the population mean value of the* ITD, *which corresponds to the neuronal estimate of* ITD. *The white dashed lines denote the physical boundaries to the input* ITD *due to the head size of the snake. The* RMS *error E_{RMS} of the estimate is given in the lower right corner of the plots. In front of the animal, 11.6 μs corresponds to a 1° localization error. The results indicate that a good estimate of* ITD *is possible for several parameter sets.*
A) $\tau_s = 500$ μs, $\tau_{refr} = 1$ ms, $J = 0.021$; B) $\tau_s = 500$ μs, $\tau_{refr} = 2$ ms, $J = 0.021$; C) $\tau_s = 250$ μs, $\tau_{refr} = 1$ ms, $J = 0.016$; D) $\tau_s = 250$ μs, $\tau_{refr} = 2$ ms, $J = 0.016$. Further parameters as in table 2.1.

halves is commonly thought to have evolved for reasons of feeding efficiency. Due to the flexibility of the jaws, snakes can stretch their mouth and swallow very large prey items.

The results presented here suggest that the need for a high-quality vibration detection system has been an extra selection criterion in the evolution of the snake skull anatomy. Unfortunately, the generally very small hearing ossicles (or their homologous bones) do not fossilize well [125][255, 256]. This makes it very difficult to test such hypotheses.

An issue that *can* be experimentally clarified is the neurophysiology underlying auditory localization in snakes. Although the general topography of the auditory pathway is roughly known in snakes [219], there is no direct evidence of a Jeffress-like localization mechanism in reptiles. Such evidence has been found in many birds (e.g. [116, 117, 141, 145]) and it should be possible to apply similar techniques to the hearing pathway in snakes and other reptiles.

The principle finding of this chapter is that vibrational Rayleigh waves traveling over the sand surface can provide accurate temporal information to the auditory pathway of snakes. This information can be used for source localization. Since reptiles and birds are phylogenetically closely related, the assumption that a Jeffress-like neuronal network is used for this localization task seems plausible.

Snakes can thus *hear* vibrations. Experimental evidence is now needed to further unravel the workings of this fascinating auditory system.
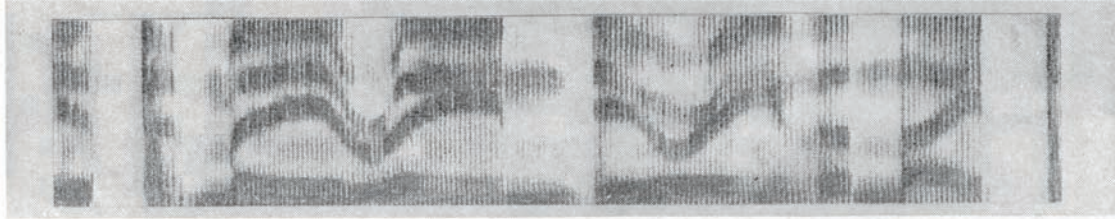
It may rain during the night
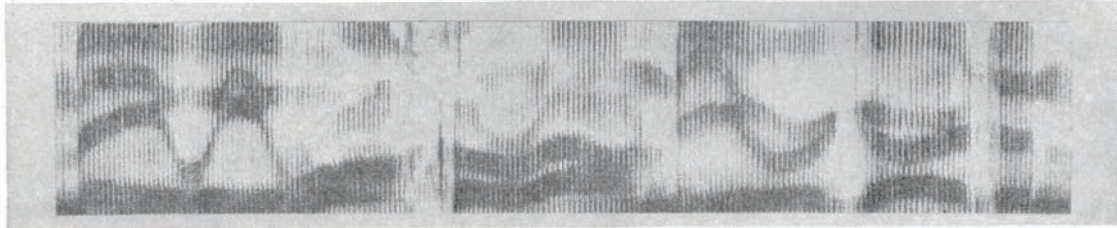
May we walk around your garden?
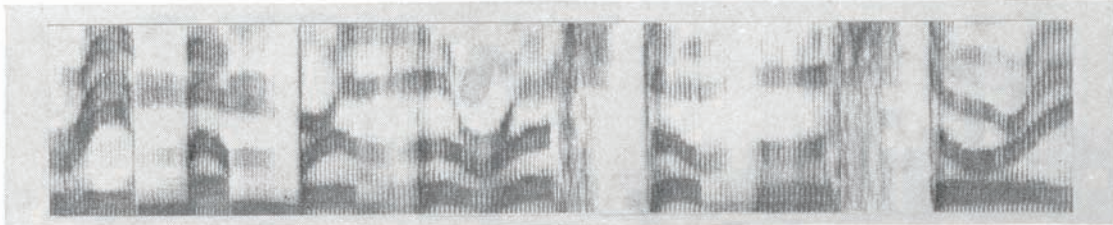
Remember the rest of the story
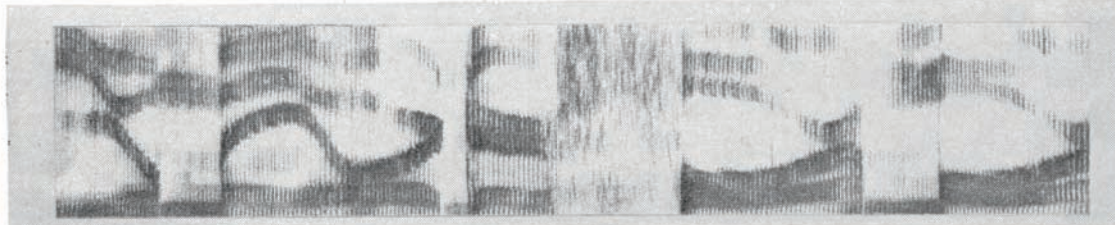
You may order four more
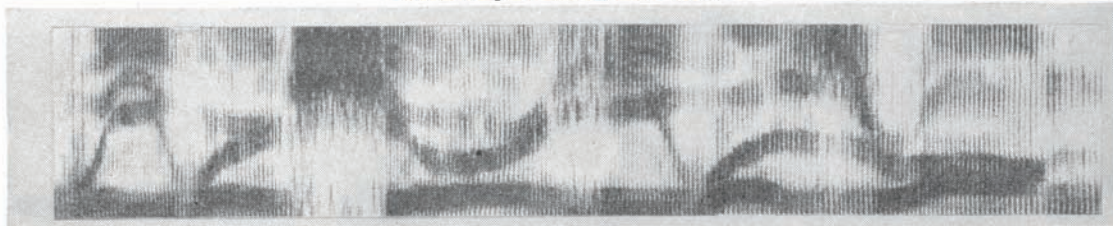
We were sure he was wrong

Potter, Kopp, & Green from Bell Labs invented techniques to measure the frequency content of a signal as a function of time. They used their spectrograms to gain insight in the process of speech production. This figure showing example speech patterns comes from their book Visible Speech, which appeared in 1947 [152]. The periodic amplitude modulations caused by the rhythmic movement of the vocal chord are clearly visible as vertical bands.

3. Neuronal identification of signal periodicity

In this chapter, two neuronal models are discussed that can neuronally extract and identify periodic features from an input signal. A mathematical analysis is presented as well as numerical simulations.[1]

3.1 Periodicity in natural signals

Sound and vibration play a very important role in communication throughout the natural world. Vertebrates possess a highly specialized vibration detector, the ear containing the cochlea, which is used to detect and to decompose signals into their constituent frequencies.

Many naturally occurring vibrations carry information about their source in the form of frequency content *and* temporal structure [142]. To be able to effectively use this information, it is important that a perceiving animal has the ability to decode both spectral and temporal cues present in the signal. Obviously animals without a mechanosensory frequency decomposer (a cochlea) at their disposal need to extract this information by neuronal means. But even animals *with* a cochlea can only extract *spectral* information using this organ. Temporal information, slow variations of amplitude over time, still needs to be decoded neuronally.

Several examples of neural temporal information extraction are known. In the human auditory system, these effects include speech recognition [159, 162], the identification of acoustic events (the "cocktail party effect" [118]), subjective pitch perception [109, 137], and the "missing fundamental" effect [109, 160]. A spectacular example of temporal information extraction is the nearly perfect recognition of speech under conditions of greatly reduced spectral information. With only three bands of noise modulated with the temporal envelopes of speech, the recognition rate of sentences is still above 80% [159]. It has often been suggested that detection of signal periodicity is essential in the recognition of auditory objects [112, 167].

Within the animal kingdom, echo-locating bats provide an interesting example of temporal information extraction. Several species of bat discriminate different insect species by their characteristic wing beat frequency which leads to a species-specific time-varying Doppler shift in the echo [158]. It has been shown that the bullfrog can extract the periodicity of complex stimuli using temporal cues [181]. Surface feeding fish can detect the frequency of vibration of the water surface with an accuracy of about 10% [174] and they use the dispersion of surface waves to determine prey distance [179]. However, the vibration-sensitive *cupulae* located on the skin of the animal [176] have no frequency specificity apart from low-pass filtering the signal [178]. The clawed frog, too, is able to detect small frequency differences in water surface wave trains [177]. All these examples

---

[1] The results presented in this chapter have been published together with Moritz Bürck and J. Leo van Hemmen [127].

clearly show that a neural mechanism to detect temporal information is a common feature shared by many animals.

This statement is supported by physiological findings. In spiders, frequency-specific neurons have been found in the central nervous system [252], although the vibration-detecting *slit sensilla*, located in the joints of their feet [224], do not exhibit frequency tuning. The sensilla rather function as acceleration detectors with a frequency-independent threshold sensitivity [225]. In the mammalian auditory system, neurons sensitive to specific modulation frequencies of auditory signals have been identified. There is a very strong sensitivity to temporal modulation of input in the Inferior Colliculus (IC) [137]. In the IC of the cat a topographical arrangement of amplitude modulation-sensitive neurons has been reported [157], but this has not been confirmed.

In this chapter, two fundamental neuronal architectures for detecting signal periodicity will be mathematically described. In the literature, several models of periodicity detection have been discussed [110, 114, 115, 144, 148]. Most of these models have either been specifically developed for the (human) auditory system and are complicated, involving many different neuron types and connections.[2]

Here, a minimalistic implementation of periodicity detection and identification is discussed without taking into account specific physiological details of the human auditory system. There are two reasons for doing so. First, discussing simple models allows a detailed mathematical treatment leading to comprehension of the abilities and limitations of the circuitry. Second, since periodicity detection is a capability present in many animals, it is important to understand general mechanisms rather than specific realizations in a certain group of animals.

The organization of this chapter is as follows. Section 3.2 gives a short introduction to the characteristics of vibratory signals. Two different models of neuronal periodicity detection are introduced in section 3.3. Mathematical properties of the models are discussed in section 3.4 and section 3.5 is concerned with numerical simulations and in section 3.6, the results are discussed.

3.2 Characterization of vibratory signals

To arrive at a clear understanding of the models discussed in this chapter, it is necessary to briefly describe some properties of vibratory signals. It is important to remember that vibratory signals are not limited to air-borne sound but may propagate in a variety of substrates such as sand [221, 226], the water surface [171, 173], spider webs [239, 245], or leaves [242]. All vibratory signals consist of a time-dependent change in pressure or medium deflection. Fast periodical variations in signal strength are normally designated as *spectral* content, or frequencies, and slow variations are denoted as *temporal* content. In general the distinction between temporal and spectral content is a matter of definition. Here, all periodic signal fluctuations which can be resolved *neuronally* are considered temporal content. That is, signal variations with frequencies lower than approximately 500 Hz are temporal.

Natural signals are composed of a mixture of spectral and temporal components, leading to complex wave forms (Fig. 3.1). The slowly varying amplitude of the signal is called the signal *envelope*. Even if no explicit modulation is imposed on a signal, slow modulations of the signal strength generally occur. This is because of interference effects between the frequency components present in the signal, which lead to a "beating" effect. In vertebrates, the cochlea is responsible for extracting spectral information; temporal clues need to be decoded neuronally. In animals lacking a cochlea or similar structure, the concept of spectral information is useless. All timing information must be extracted neuronally.

---

[2] It is known that hair cells exhibit frequency tuning, without the need for a neuronal network architecture. This is achieved through the interplay between slow and fast ion channels, causing oscillatory current dynamics. The typical range of this frequency sensitivity is about 16–600 Hz (see discussion in [128]). Since this phenomenon is *only* known to occur in cochlear hair cells, it will not be discussed further here.
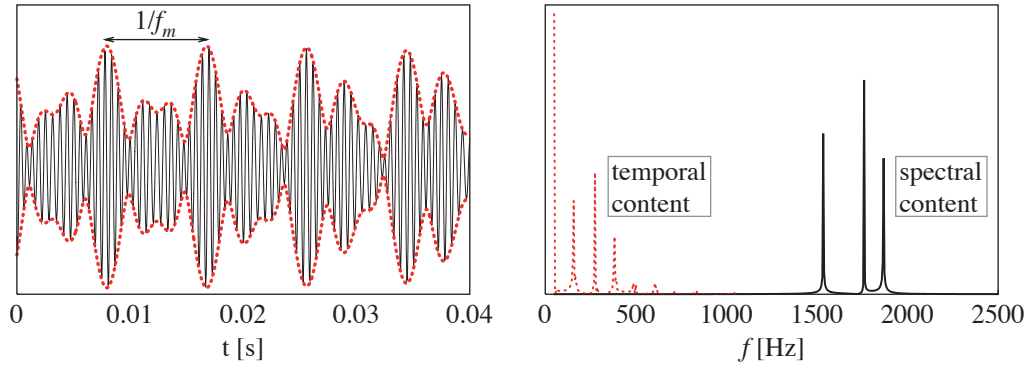
Figure 3.1: *The left panel shows a complex wave signal, composed of three frequency components (solid black) and the signal envelope, or instantaneous amplitude (dotted red). The interference of the frequency components causes amplitude modulation on a slow scale. One of the modulation frequencies ($f_m \sim 100$ Hz) has been indicated in the plot.*
The right panel shows the Fourier transform of the signal (solid black) and the envelope (dotted red). Although the signal consists of three frequencies in the 1500–2000 Hz range, the envelope shows only slow variations, mainly below 500 Hz. Because the envelope has a nonzero mean value the Fourier spectrum shows an additional peak at 0 Hz.

The simplest example of a modulated vibration is sinusoidal amplitude modulation (SAM). An SAM signal $s(t)$ is described by

$$s(t) = A\cos(2\pi f_c t)[1 + m\sin(2\pi f_m t)], \tag{3.1}$$

with $f_m \ll f_c$. The amplitude of the signal is A, f_c is the carrier frequency, f_m is the modulation frequency and m is the modulation depth of the signal. Of course, an SAM signal is not a realistic input. Natural signals typically consist of some superposition of frequencies that are comodulated [149] by a *characteristic profile* instead of a simple sine wave. The fundamental period of this profile is then called the modulation frequency.

On the surface of the water [170, 172, 180][223], in spider webs [244], and on plant leaves [223, 232], discrimination of prey is achieved by using only the frequency content of the incoming signals. In both cases prey-generated signals contain high frequencies ($\gtrsim 50$ Hz). In contrast, background noise such as abiotic signals and vibrations caused by the movement of the animal itself is limited to low frequencies ($\lesssim 15$ Hz). To detect prey, the animal needs to know whether the signal has predominantly high-frequency content or low-frequency content. Amplitude modulations are believed to be of less importance in this case.

3.3 The models

The aim of the models presented here will be to identify slow fluctuations present in a specific input signal. Mathematically, periodic features of a signal $s(t)$ can be detected by calculating its autocorrelation χ (see e.g. [147]), defined by

$$\chi(\Delta) = \lim_{T\to\infty} \frac{1}{2T} \int_{-T}^{T} dt'\ s(t')s(\Delta + t') . \tag{3.2}$$

The autocorrelation has maxima for correlation times Δ corresponding to the frequencies present in the signal, but also for the periods of the envelope fluctuations (Fig. 3.1). The above calculation immediately suggests two neuronal mechanisms for detecting periodicity (Fig. 3.2).
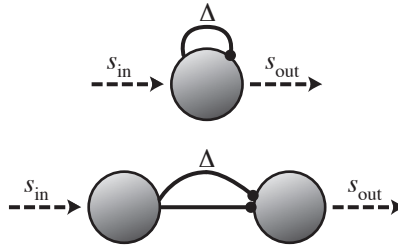
Figure 3.2: *There are basically two possible ways to extract temporal information from a signal using spiking neurons. The first method (upper panel) uses a recurrent loop with time delay Δ. This is called the* recurrent model. *The neuron is driven by a continuous input function s_{in}. If the neuron emits a spike at time $t = t_0$, the firing probability is enhanced at time $t = t_0 + \Delta$. Signal periodicity with characteristic time Δ then leads to a higher number of spikes in the output signal s_{out}.*

The second method (lower panel) is based on the same idea, but uses a feedforward network, and is called the feedforward model. *The first neuron, again driven by s_{in}, sends two spikes to the output neuron with a delay differing by an amount Δ, e.g. using interneurons. Again, correlations in the input signal with period Δ lead to an augmented firing probability for the output neuron.*

The first model consists of an array of neurons that receive an input signal $s_{in}(t)$. As one of the neurons spikes, the output spike is fed into a pathway that ultimately projects onto the neuron itself with a particular delay Δ, corresponding to the correlation time above. This pathway need not be a direct connection from the axon onto the neuron's own dendritic tree. One or more processing steps may occur before the output from the neuron returns but a well-defined delay can be associated with the pathway. This matter will be further discussed in section 3.6.1. Because of the delay loop, the neuron detects correlations on a time scale Δ. An array of such neurons, all with different Δ, can then function as a periodicity analyzer. This model is called the *recurrent model*.

The second model consists of an array of input-output neuron pairs. If one of the input neurons fires, it's spikes are fed into two pathways to the corresponding output neuron. The temporal delays of these pathways differ by an amount Δ. The output neuron will have a high firing probability if spikes arrive from the two different pathways at the same time. Again, the network reveals correlations on time scale Δ. This model is called the *feedforward model*.

Both types of networks have been discussed before in the literature. The first author to propose a network of delay lines to detect signal periodicity has been Licklider [144]. More recent work on feedforward-like models has been done by Borst et al. [110] and Meddis and O'Mard [148]. Both articles proposed a very detailed model, based on specific properties of neuronal circuitry found in the mammalian auditory system. Although Borst et al. and Meddis and O'mard have used neuronal oscillators instead of delay lines, the analysis discussed in this chapter can be applied to their models as well.

Cariani [114, 115] discussed a recurrent-like model. He has used an overly simple model in which formal neurons manipulating strings of 0s and 1s are used. None of these authors have included a detailed mathematical analysis of their models. Before proceeding to mathematically and numerically scrutinize the models the characteristics of both models will be discussed in more detail.

3.3.1 Detailed description of the recurrent model

The recurrent model consists of N_{out} output neurons that all receive the same external continuous input $s_{in}(t)$. All input neurons have a recurrent connection that feeds output spikes back into the neuron itself. The recurrent spikes are characterized by a delay Δ that is different for each neuron and has strength J. The feedback current is described by a general function h (see also the

section 3.4.1) for which an α-function will be taken in the simulations

$$h(t) = \alpha(t - t_0 - \Delta, \tau_s) \,. \tag{3.3}$$

The width of the α-function is given by τ_s, t_0 is the spiking time of the neuron.

The neurons are simulated as leaky integrate-and-fire (LIF) neurons; see appendix B.1.1. To get the model at work the output neurons must fire a first spike to start with, since the feedback loop needs input, which can only come from the neurons themselves. It is not possible to use supra-threshold input since this would imply that *all* output neurons would fire in response to the input, regardless the length of their delay loop. The solution is to use subthreshold input with added internal neuronal noise, see section 3.5.1. Every now and then the neuron will fire. But only if the delay loop length has the right value the neuron will be able to resonate in response to the input. The mechanism described here is called *stochastic resonance* (extensively reviewed in [258]).

3.3.2 Detailed description of the feedforward model

The feedforward model consists of N_{in} input neurons, which are simulated as Poisson neurons; see appendix B.2.1. This is convenient for a mathematical characterization but by no means necessary. The input neurons are driven by an external input $s_{\mathrm{in}}(t)$. If one of the input neurons fires its spike is fed into an axon branching off to N_{out} different output neurons. One spike reaches the output neurons directly and another spike resulting from the same event reaches the output neuron with a delay Δ. A specific delay Δ is associated with every output neuron. In this way, every output neuron will turn out to encode a particular frequency $f = 1/\Delta$.

The output neurons are simulated as leaky integrate-and-fire (LIF) neurons without noise; see appendix B.1.1. If a spike is emitted at time $t = t_0$ by any of the input neurons it leads to two postsynaptic current injections arriving at the output neurons, again in the form of α-functions,

$$\varepsilon_{\mathrm{direct}} = J\alpha(t - t_0, \tau_s) \tag{3.4}$$

and

$$\varepsilon_{\mathrm{delayed}} = J\alpha(t - t_0 - \Delta, \tau_s) \,. \tag{3.5}$$

The former spike travels to the output neuron without delay and the latter arrives with a delay Δ. The synaptic coupling strength is again given by the parameter J.

3.4 Mathematical discussion of the models

This section mathematically discusses the behavior of the two types of periodicity detector. Explicit analysis of LIF neurons is generally quite difficult (for an extensive review, see [24, 25]). Luckily, no explicit analysis of LIF neuron dynamics is needed to gain valuable insight into the dynamics of both models. In fact, the key properties of the models are independent of the specific type of neurons that are used.

3.4.1 Recurrent model

The problem of analytic calculations using integrate-and-fire neurons lies in the nonlinearity of threshold crossing and spike-generation. In the case of the recurrent network discussed here, the problem is even more difficult than usual since the feedback introduces an extra complication into the system. The discussion is simplified by considering Poisson neurons; see appendix B.2.1.
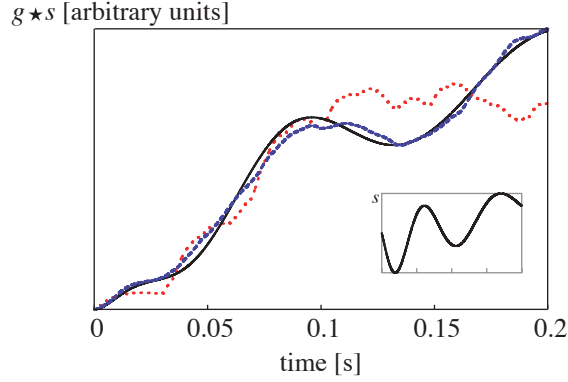
$g \star s$ [arbitrary units]

Figure 3.3: *Stochastic fluctuations in the response of a Poisson neuron are smaller if the firing rate is higher. The convolution of a signal s (inset) with the response kernel h in black is compared with two explicit realizations of the firing process (normalized for comparison). The red dotted curve was obtained using about 40 spikes, the blue dashed curve results from about 300 spikes. Clearly, a high firing rate (or, mathematically equivalent, a large population of Poisson neurons) is needed for Eq. (3.6) to apply.*

The rate function λ of a single Poisson neuron projecting back to itself with a particular delay time Δ is given by the integral equation

$$\lambda(t) = s_{\text{in}}(t) + J \int_{-\infty}^{\infty} \text{d}s \ h(s, \Delta)\lambda(t - s)$$
$$= s_{\text{in}}(t) + J(h \star \lambda)(t) \, . \tag{3.6}$$

The rate function consists of the sum of the external input s_{in} and the delayed input from the recurrent loop, "smeared out" by the kernel h. The feedback strength is given by J and h is chosen to ensure causality ($h(t) = 0$ if $t < 0$) and to have unit weight

$$\int_{-\infty}^{\infty} \text{d}t \ h(t) = 1 \, . \tag{3.7}$$

Since h has a finite width the delay loop smears out the feedback.

In Eq. (3.6) the convolution integral of λ with the kernel h assumes that it is OK to use the expectation value of the firing rate λ to describe the neuron output instead of a specific realization of the output. Effectively, the "spiky" character of the neuron output is ignored. This approach is only correct for high firing rates or, mathematically equivalent, a large number of Poisson neurons with a low firing rate. The total amount of output spikes must be high enough so that the output signal is reliably sampled by the output spikes. An example of such a smooth convolution of λ and h is shown in figure 3.3.

To solve Eq. (3.6) for the output firing rate λ it is useful to take the Fourier transform (see p. 81). The Fourier transform has the convenient property that, when transformed, a convolution becomes an ordinary product. Denoting the Fourier transform of each input term by a capital letter one obtains

$$\Lambda(\omega) = S_{\text{in}}(\omega) + JH(\omega)\Lambda(\omega) \, . \tag{3.8}$$

The solution is given by

$$\Lambda = \frac{S_{\text{in}}}{1 - JH} \, . \tag{3.9}$$

and the solution as a function of time can then be found by taking the inverse Fourier transform

$$\lambda(t) = \mathcal{F}^{-1}\left[\Lambda(\omega)\right](t) \, . \tag{3.10}$$

3. Neuronal identification of signal periodicity

Given any input function s_{in} and response function $h(t)$ it is now possible to explicitly calculate the firing probability of the neuron. In the simulations in this chapter an α-function with synaptic time constant τ_s is used for h [see Eq. (3.3)]. The Fourier transform of this response function is given by

$$H(\omega) = \frac{e^{-i\omega\Delta}}{(1 + i\omega\tau_s)^2} \ . \tag{3.11}$$

Since the interesting part is *identifying* periodicity, it must be known which frequency f corresponds to a certain delay time Δ. A naïve guess would be to simply set $f = 1/\Delta$, but since the response function transforms the recurrent signal in a non-trivial way this relation cannot be expected to hold exactly. Consider therefore the response of the system to an incoming pure sine wave of frequency f. Finding the corresponding Δ that maximizes the amplitude of the response establishes an explicit connection between the delay Δ and the signal frequency that is decoded optimally through this delay.

For harmonic input given by

$$s_{\text{in}}(t) = A\cos(\omega t) = A\cos(2\pi f t) \tag{3.12}$$

the response is

$$\lambda(t) = L\cos(\omega t + \phi) \ , \tag{3.13}$$

where ϕ is a phase that is not relevant for further calculations and L is an amplitude given by

$$L = \frac{A(1 + \xi^2)}{\sqrt{J^2 + (1 + \xi^2)^2 - J\left[2(1 - \xi^2)\cos(\omega\Delta) - 4\xi\sin(\omega\Delta)\right]}} \ , \tag{3.14}$$

with the definition $\xi := \omega\tau_s$. The amplitude L of the response is maximal if the relation

$$\frac{\mathrm{d}L}{\mathrm{d}\Delta} = -2(1 - \xi^2)\sin(\omega\Delta) - 4\xi\cos(\omega\Delta) = 0 \tag{3.15}$$

holds. The delay must therefore satisfy

$$\Delta = \omega^{-1}\left[\arctan\left(\frac{2\xi}{\xi^2 - 1}\right) + n\pi\right] \ , \tag{3.16}$$

with $n = 1$ if $\xi > 1$ and $n = 2$ for $\xi < 1$. If the width of the kernel h approaches zero ($\xi \to 0$, no smearing out of the input) this relation indeed reduces to

$$\Delta = \frac{2\pi}{\omega} = \frac{1}{f} \ . \tag{3.17}$$

A more complicated and realistic example is given by input of the form

$$s_{\text{in}}(t) = \int_0^\infty \mathrm{d}\sigma\ B(\sigma)\cos\left[\sigma t + \phi(\sigma)\right] \ . \tag{3.18}$$

Instead of a single harmonic component a distribution of input frequencies with arbitrary amplitude and phase is now taken. The Fourier transform of the input is given by

$$S_{\text{in}}(\omega) = \int_0^\infty \mathrm{d}\sigma\ B(\sigma)\pi e^{i\phi(\sigma)\omega/\sigma} \times \left[\delta(\sigma - \omega) + \delta(\sigma + \omega)\right] \ . \tag{3.19}$$

Plugging this result into (3.9) and (3.10) gives the solution for the firing rate of the output neuron

$$\lambda(t) = \int_0^\infty \mathrm{d}\sigma\ B(\sigma)\ \Re\left[\frac{e^{i(\phi(\sigma) + \sigma t)}}{1 - Je^{-i\sigma\Delta}/(1 + i\sigma\tau_s)^2}\right] \ , \tag{3.20}$$

where $\Re[x]$ denotes the real part of x. The signal function (3.18) need not be positive, although a negative firing rate certainly does not make sense for a Poisson neuron. In the simulations in chapter 3 half-wave rectified signals are always used (see p. 81). Unfortunately exact calculations are not feasible in this case. In spite of this drawback Eq. (3.20) captures the essence of the network response. If the solution (3.20) is plotted for various input spectra $B(\sigma)$ the amplitude of λ is largest if the length of the delay loop Δ corresponds to a frequency that is present in the input signal. Because of the complicated form of (3.20), it is of limited practical use. A better way to gain insight into the model dynamics is to use numerical simulations, see section 3.5.

3.4.2 Feedforward model

For the analytic description of the feedforward model an input population of Poisson neurons is used. They are, just as before, driven by an input $s_{\mathrm{in}}(t)$ identical for each neuron. The output neurons are taken as LIF neurons. Every output neuron receives input from the Poisson neurons via two distinct pathways: a direct connection and a connection with a delay Δ which is different for each output neuron.

Calculating the expectation value of the current that arrives at the output neurons results in a sinusoidal function. The response of LIF neurons to harmonic input is difficult to calculate but several exact results have been presented by Burkitt [26] as will be discussed below.

Input given by

$$s_{\mathrm{in}}(t) = \frac{A}{2}\left[1 + \cos(\omega t)\right] \tag{3.21}$$

is the starting point of the calculations. The input current that one output neuron with a particular delay time Δ receives from the set of N_{in} input neurons is given by [referring to (3.4) and (3.5)]

$$\varepsilon_{\mathrm{total}} = \varepsilon_{\mathrm{direct}} + \varepsilon_{\mathrm{delayed}}\,. \tag{3.22}$$

The expectation value of the current to the output neurons is given by (see appendix B.2.1)

$$\langle I \rangle = \int_{-\infty}^{\infty} \mathrm{d}s \; s_{\mathrm{in}}(s) \; \varepsilon_{\mathrm{total}}(t - s) \tag{3.23}$$

and the variance of the current is given by

$$\mathrm{var}_I = \int_{-\infty}^{\infty} \mathrm{d}s \; s_{\mathrm{in}}(s) \; \varepsilon_{\mathrm{total}}^2(t - s)\,. \tag{3.24}$$

Equations (3.23) and (3.24) can be evaluated exactly for the given input function (3.21). The current is

$$\langle I \rangle = N_{\mathrm{in}} A J \left\{ 1 + \frac{\cos(\omega\Delta/2)}{(1 + \xi^2)^2} \left[(1 - \xi^2)\cos\left(\omega(t - \Delta/2)\right) + 2\xi\sin\left(\omega(t - \Delta/2)\right) \right] \right\} \tag{3.25}$$

with $\xi = \omega\tau_s$. The amplitude (current arriving at the output neuron) is thus maximal if $\cos(\omega\Delta/2)$ is maximal, implying integer

$$\Delta \cdot \frac{\omega}{2\pi} = \Delta \cdot f \in \mathbb{N}\,. \tag{3.26}$$

That is, a maximal response of the output neurons is to be expected if the input frequency matches the delay of the system. If the input signal contains a periodicity with frequency $\bar{f}$ the neuron with a delay time $\bar{\Delta}$ corresponding to this frequency will respond optimally. All neurons sensitive to a *subharmonic* frequency ($\bar{f}/n$, with $n \in \mathbb{N}$) will also respond, as can be seen from (3.26). This is because an input signal with a periodicity $\bar{f}$ is automatically also periodic with frequency $\bar{f}/n$.

The variance of the current is given by

$$
\text{var}_I = \frac{N_{\text{in}} A J^2}{\tau_s} \left\{ \frac{1}{4} + M + \frac{2\cos(\omega\Delta/2)}{(4+\xi^2)^3} \right.
$$
$$
\left. \times \left[(8-6\xi^2)\cos\left(\omega(t-\Delta/2)\right) + \xi(12-\xi^2)\sin\left(\omega(t-\Delta/2)\right) \right] \right\}
$$

(3.27)

where M is

$$
M = e^{-\Delta/\tau_s} \left\{ \frac{1-\Delta/\tau_s}{4} + \frac{1}{(4+\xi^2)^3} \right.
$$
$$
\times \left[\left(16 - 8\xi^2 + \frac{\Delta}{\tau_s(16-\xi^4)} \right) \cos\left(\omega(t-\Delta)\right) \right.
$$
$$
\left. \left. + 2\xi \left(12 - \xi^2 + \frac{2\Delta}{\tau_s(4+\xi^2)} \right) \sin\left(\omega(t-\Delta)\right) \right] \right\}.
$$

(3.28)

In order to allow correct periodicity detection, the time scale of the periodicity must clearly exceed the time scale τ_s of the individual current response functions ϵ. Therefore, the system can be expected to work best if the relation $\Delta \gg \tau_s$ holds, meaning that the time scale of the periodicity is much larger than that of the post-synaptic response. In the auditory system this condition will generally hold. M can then be neglected because of the exponential prefactor $e^{-\Delta/\tau_s}$ in (3.28). If low-frequency input is presented, the relation $\omega \ll 1/\tau_s$ is valid and thus $\xi = \omega\tau_s \to 0$ can be assumed. The current and its variance are then given by

$$
\langle I \rangle = N_{\text{in}} A J \left[1 + \cos(\omega\Delta/2)\cos\left(\omega(t-\Delta/2)\right) \right]
$$

(3.29)

and

$$
\text{var}_I = \frac{4N_{\text{in}} A J^2}{\tau_s} \left[1/16 + \cos(\omega\Delta/2)\cos\left(\omega(t-\Delta/2)\right) \right] .
$$

(3.30)

The relative variation of the current is proportional to

$$
\frac{\delta I}{I} = \frac{\sqrt{\text{var}_I}}{I} \propto \frac{1}{\sqrt{N_{\text{in}} A \tau_s}} ,
$$

(3.31)

which also holds if the assumptions $\Delta \gg \tau_s$ and $\xi \to 0$ are *not* made. As expected, the current is less sensitive to random fluctuations if the number of input neurons or the input amplitude increases. The fact that the current fluctuates more if τ_s gets smaller is because a very short synaptic time scale tends to enhance the "spiky" character of the current. The system, however, does not become less reliable since a short post-synaptic current enables better coincidence detection by the output neurons [34, 35].

The expression (3.25) for the mean current, which is a good approximation if there are enough input neurons, shows that all output neurons receive a harmonic (sinusoidal) current. The amplitude of the current is largest if the delay matches the periodicity of the input signal. The response of integrate-and-fire neurons to harmonic input is difficult to calculate but it has been done for a slightly different system in [26]. The results show that the periodicity of the input current is retained in the firing of the output neuron. This means that the output signal is phase locked to the current. The vector strength VS (see section 1.4) measures the amount of synchronization or phase locking. VS tends to be larger in the output neuron than in the current itself.

3.4.3 Summary of mathematical results

The most important mathematical property of the recurrent model is the relation between loop delay Δ and optimal coding frequency f. Naïfly, one would expect the relation $\Delta = 1/f$ to hold.

The recurrence loop does not, however, simply projects the output back to the neuron. The response kernel h rather smears out the feedback, changing the exact timing of the recurrent input. The exact relationship between delay and coding frequency is given by Eq. (3.16) for synaptic responses in the form of an α-function.

In the feedforward model, the problem of finding the relation between Δ and f does not arise. Both the direct and the delayed pathway smear out the input spikes in the same manner and therefore, the relative timing of the two signals arriving at the output neuron is fixed. The most important result for the feedforward model is that the amount of phase locking (a measure for the accuracy of spike timing) actually increases. The output neurons fire thus more accurately than the input population does. This is in accordance with physiological findings in the mammalian auditory pathway [137].

For a true understanding of the models, the mathematical description presented above does not suffice. Since the nonlinear process of spike generation cannot be taken into account, numerical simulations are needed to characterize the response of the models to realistic input. The next section discusses such simulations.

3.5   Simulation results

In this section results obtained by numerical simulations are discussed. The neural networks as described in section 3.3 have been implemented through the C^{++} programming language. To test model performance three different kinds of input were used: amplitude-modulated (AM) input, a Gaussian distribution of frequency components, and input mimicking the "missing fundamental" effect, as explained below. The response of the system was characterized by counting the number of output spikes that occurred during one second of input presentation as a function of the coding frequency of the output neuron. The coding frequency of the output neurons was calculated using (3.16) for the recurrent network and (3.26) for the feedforward network. It will become clear that in both networks the neurons encoding the periodicity present in the input signal respond maximally. The networks are thus able to convert a *periodicity code* into a *rate code*.

Half-wave rectification of the signals (see p. 81) was always performed before presenting them to the network. Hair cells, the basic receptor units of the ear and the lateral line system, depolarize following one direction of displacement and hyperpolarize if displacement is in the other direction [133]. Half-wave rectification is therefore automatically performed upon detection in many sensory systems.

The input signal to the network was normalized to deliver the same time-integrated input power in each case. Obviously, it is not realistic to expect external input to a vibration detection system to be normalized but several mechanisms of neuronal *gain adaptation* have been demonstrated experimentally; e.g., in the auditory pathway [121, 135, 161, 166]. Such mechanisms are thought to keep neuronal firing rates within an optimal range [128]. The result of this normalization is effectively a logarithmic dependance of the firing rate on the input amplitude. This compresses the dynamical range and, in addition, relative differences between input amplitudes are coded by a constant difference in firing rates, independent of the input strength.

In the models described in this chapter, power normalization is needed to keep the output firing under control. If the input power is too low, the output neurons cannot fire at all. If, on the other hand, the input power is too high all neurons will fire at a high rate and the discriminative capacity of the system is lost.

3.5.1   Numerical implementation

Both neuronal models have been implemented using the C^{++} programming language. Below, all model parameters are listed, as well as the internal noise mechanism adopted for the neurons in

parameter	value
number of output neurons	$N_{\mathrm{out}} = 491$
output frequency range	10–500 Hz
synaptic time constant	$\tau_s = 1\,\mathrm{ms}$
synaptic strength	$J = 2.5 \times 10^{-5}$
input normalization	$1/T \int_0^T \mathrm{d}t\ s_{\mathrm{in}} = 300$
output neuron	
membrane time	$\tau_m = 1.25\,\mathrm{ms}$
absolute refraction time	$\tau_{\mathrm{refr}} = 1.0\,\mathrm{ms}$
resting potential	$V_r = 0$
reset potential	$V_{\mathrm{reset}} = V_r = 0$
threshold	$V_\theta = 1$
capacitance	$C_m = 1$

Table 3.1: *Simulation parameters for the recurrent model.*

the recurrent model.

Recurrent model

For this model, LIF neurons (appendix B.1.1) were used with the parameters from table 3.1 Internal noise of the neurons has been implemented by adding a noise term I_{noise} to the input of each neuron given by

$$I_{\mathrm{noise}} = \sum_{n=1}^{50} A_{\mathrm{noise}} \cos(2\pi f_{\mathrm{noise}}^n t + \phi_{\mathrm{noise}}^n) \tag{3.32}$$

where the frequencies are chosen from a uniform distribution $f_{\mathrm{noise}}^n \in [0\text{–}1000\,\mathrm{Hz}]$. Phases are uniformly distributed in $\phi_{\mathrm{noise}}^n \in [0\text{–}2\pi]$ and the amplitude of every component is given by $A_{\mathrm{noise}} = 0.01/50$. For each neuron, independent noise is assumed and the noise is added linearly to the input for each neuron.

Feedforward model

For this model, Poisson neurons (appendix B.2.1) were used for the input population and LIF neurons (appendix B.1.1) for the output population. Parameters were taken as in table 3.2

In the following sections, the results of the simulations are presented.

3.5.2 Amplitude-modulated input

Two types of AM input signals are discussed. The first signal is a modulated pure tone

$$s_{\mathrm{in}}(t) = \frac{A}{2}[1 + \cos(2\pi f_m t + \phi)]\cos 2\pi f_c t \tag{3.33}$$

with modulation frequency $f_m = 50\,\mathrm{Hz}$ or $f_m = 200\,\mathrm{Hz}$ and random modulation phase ϕ. The carrier frequency is $f_c = 2000\,\mathrm{Hz}$.

In the second case, a noisy input is constructed by composing a signal from 50 sinusoidal components with frequencies f_{rand}^n chosen from a uniform distribution on $[0\text{–}1000\,\mathrm{Hz}]$ and random phases ϕ_{rand}^n with uniform distribution on $[0\text{–}2\pi]$ so as to obtain

$$s_{\mathrm{noise}}(t) = \sum_{n=1}^{50} \cos(2\pi f_{\mathrm{rand}}^n t + \phi_{\mathrm{rand}}^n)\,. \tag{3.34}$$

parameter	value
number of input neurons	$N_{\text{in}} = 25$
number of output neurons	$N_{\text{out}} = 491$
output frequency range	10–500 Hz
input neuron mean rate	20 Hz
synaptic time constant	$\tau_s = 1\,\text{ms}$
synaptic strength	$J = 3.5 \times 10^{-4}$
output neuron	
membrane time	$\tau_m = 1\,\text{ms}$
absolute refraction time	$\tau_{\text{refr}} = 0.25\,\text{ms}$
resting potential	$V_r = 0$
reset potential	$V_{\text{reset}} = V_r = 0$
threshold	$V_\theta = 1$
capacitance	$C_m = 1$

Table 3.2: *Simulation parameters for the feedforward model.*
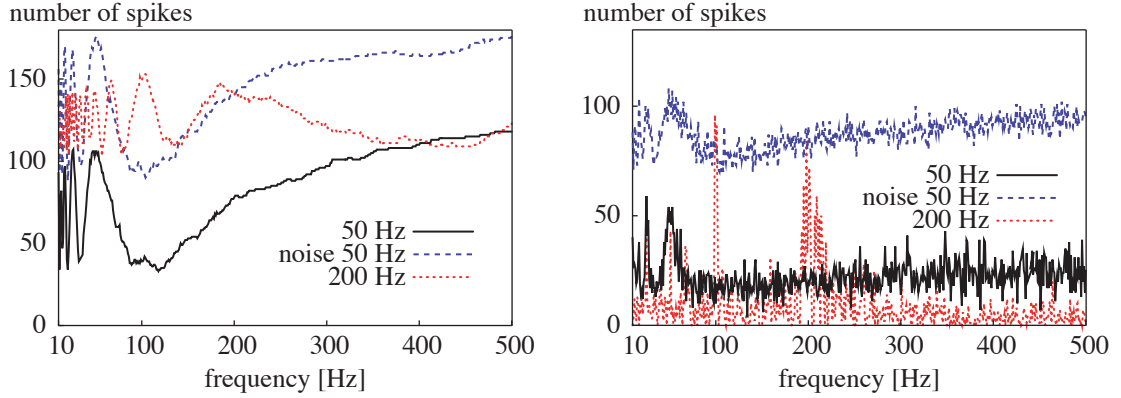

Figure 3.4: *Response to AM input of an array of neurons, each with a different delay and corresponding frequency (horizontal axis). The total number of spikes in one second is shown vertically. Left panel: feedforward model; right panel: recurrent model. The peaks corresponding to the input periodicity clearly appear in the graphs. Evidently, both networks correctly identify the signals.*

This signal is than modulated with modulation frequency $f_m = 50$ Hz:

$$s_{\text{in}}(t) = \frac{A}{2}[1 + \cos(2\pi f_m t + \phi)] \times s_{\text{noise}}. \tag{3.35}$$

In both cases the amplitude has been chosen in such a way that the rectified input signal is normalized appropriately.

The results of these simulations are displayed in Fig. 3.4. Obviously both network types succeed very well in detecting the periodicity of the input signal. Clear peaks in the response occur for the correct frequencies. The response peaks for the subharmonic frequencies are also distinctly recognizable. Although the response of the recurrent model is quite noisy, this drawback may be overcome easily by combining input from several close-by channels.
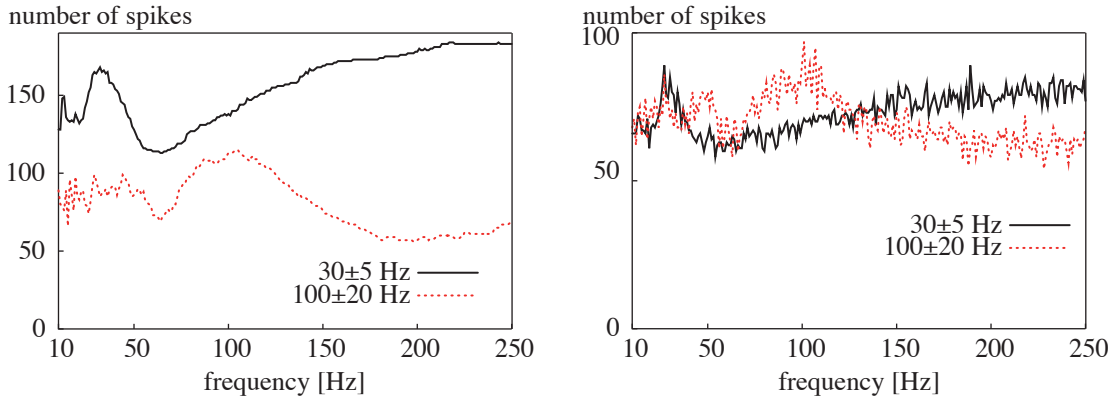
Figure 3.5: *Response of an array of neurons to a distribution of frequencies. Input was presented to an array with neurons, each with a different delay and specific frequency (horizontal axis). The total number of spikes in one second is shown vertically. Left panel: feedforward model; right panel: recurrent model. Similarly to figure 3.4 the signals are reliably identified.*

3.5.3 Gaussian frequency distribution

The second test for the feedforward and recurrent models consists of taking a *distribution* of frequencies as input. To mimic the real biological situation an input signal has been built from 30 different frequency components chosen randomly from a Gaussian probability distribution with a center frequency μ and a width σ. The components were added together with random phases and the resulting signal was half-wave rectified and presented to the network. This signal can for instance be considered as a rough model for a trampling insect on the water surface or in a spider web. The results of these simulations are displayed in Fig. 3.5. It is evident that both frequency profiles with $(\mu, \sigma) = (30\,\text{Hz}, 5\,\text{Hz})$ and $(\mu, \sigma) = (100\,\text{Hz}, 20\,\text{Hz})$ are correctly identified by the two networks.

3.5.4 Missing fundamental

If several pure tones with a *common* fundamental frequency are presented to a listener, the subject often perceives a tone with a pitch corresponding to this fundamental frequency, even though the fundamental frequency itself may not be present in the input signal. Nonetheless a clear neuronal representation of this frequency is formed by the subject. Such an experiment is mimicked by giving both models input consisting of three harmonics

$$s_{\text{in}}(t) = \sum_{n=1}^{3} \cos(2\pi f_n t + \phi_n) \,, \tag{3.36}$$

with $f_1 = 200\,\text{Hz}$, $f_2 = 300\,\text{Hz}$, $f_3 = 400\,\text{Hz}$ and random phases. The response of the feedforward model is shown in Fig. 3.6, together with the response to a pure tone of 100 Hz. Although the peak is not as clear as with pure tone stimulation, a pitch of 100 Hz is still easily recognizable.

Because of the noisy response, the missing fundamental effect is not reproduced very well by the recurrent model. A very good response can sometimes be obtained but this crucially depends on the precise values of the phases ϕ_n, which is not realistic biologically. Results for the recurrent network are therefore not shown here.
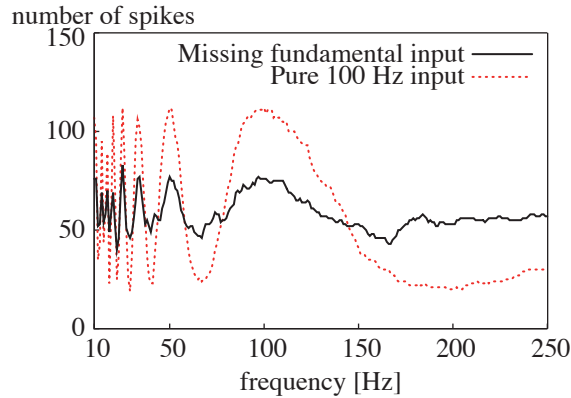
number of spikes

Figure 3.6: *Response of the feedforward network to "missing fundamental" input as in Eq. (3.36) with three frequencies* 200, 300 *and* 400 Hz *compared to the response to a pure* 100 Hz *tone. The peak at* 100 Hz *is clearly recognizable.*
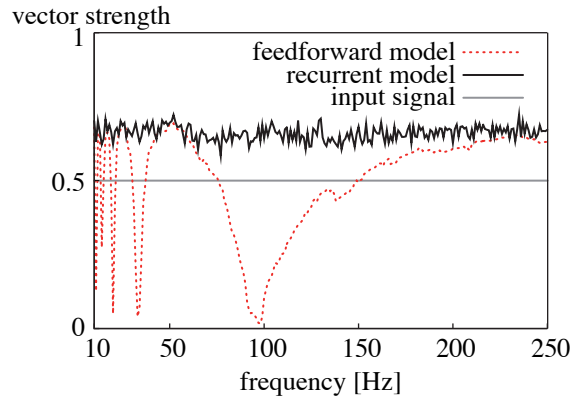
vector strength

Figure 3.7: *Phase locking strength as a function of best frequency for the feedforward and the recurrent model.* 50 Hz *modulated input as in Eq. (3.35). Vector strength of the input signal is 0.5, as indicated by the horizontal line. Surprisingly, output phase locking is stronger than input phase locking in the relevant frequency range.*

3.5.5 Phase locking

A very important concept in auditory or vibratory processing is phase locking. Phase locking describes the capability of neurons to spike preferentially at a specific phase of the input signal. Phase locking is especially important to extract precise temporal clues from a signal; for instance, in sound localization [131, 150]. The amount of phase locking is characterized by the vector strength VS as discussed in section 1.4.

For AM noise input, as in (3.35), the vector strength has been displayed in Fig. 3.7. Interestingly, phase locking is quite good in the recurrent model although the output firing rate fluctuates a lot. This behavior results from the subthreshold input dynamics of the recurrent model. Only the presence of noise in the input assures that every now and then a spike occurs. The occurrence of a spike is of course much more likely if the input amplitude is large and consequently the output firing tends to be phase-locked to the input periodicity. For the feedforward model phase locking is good if the decoding frequency of the output neurons matches the periodicity of the input. Again, spike generation is most likely when the input amplitude is large *and* the delay time matches the frequency of the input signal. Phase locking results. Remarkably, phase locking strength of the
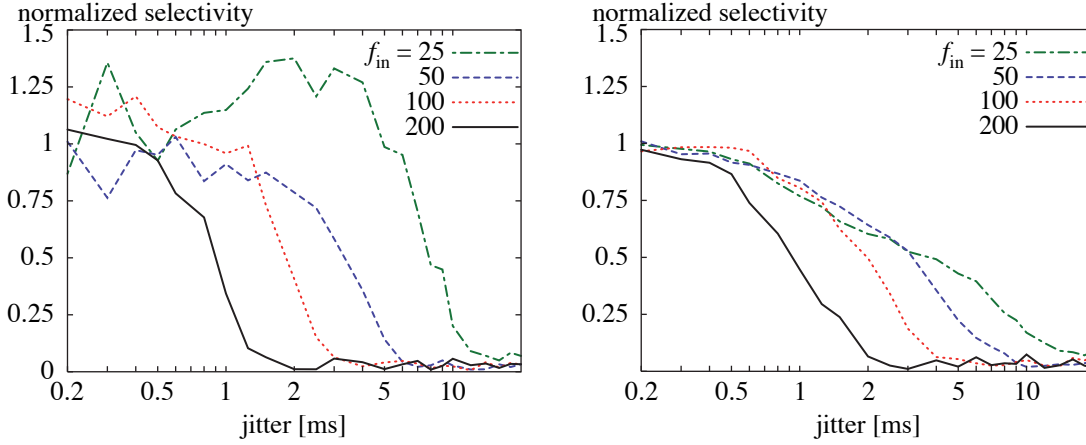
Figure 3.8: *The selectivity as defined in (3.37) for the feedforward (left) and recurrent (right) model for several input signal frequencies f_{in} as a function of jitter. The selectivity Q is normalized with respect to the value in the absence of jitter. As expected, increasing jitter leads to a decrease in selectivity. For both the feedforward and the recurrent model a jitter of approximately 20% of the input period leads to a 50% decrease in selectivity.*

output is significantly larger than the VS of the input signal for both models.

3.5.6 Temporal jitter of delays

The ability to identify signal periodicity crucially depends on the timing of the delays Δ. It is therefore important to investigate the effect of temporal jitter in the delays on identification performance. To do so, four different pure tones with frequency f_{in} were presented to both networks and stochastic jitter was added to the delay time for every emitted spike. The jitter is Gaussian distributed with mean 0 and a standard deviation from 0.2 ms to 20 ms. For each trial (a specific combination of input frequency and jitter strength) the *selectivity Q* was calculated. Q is defined by

$$Q = \frac{\left| \sum_j r_j e^{2\pi i \Delta_j f_{in}} \right|}{\sum_j r_j} \ . \tag{3.37}$$

Here Δ_j is the temporal delay corresponding to output neuron j and r_j is its firing rate. This definition has again the form of a vector strength. If the output firing rate peaks for neurons with the correct delay ($\Delta_j f_{in}$ integer) the value of the numerator in Eq. (3.37) will be large. If much temporal jitter is present all output neurons will respond, even if their delay does *not* match the input signal frequency. In this case the phases in the numerator of Eq. (3.37) will cancel out and Q will have a low value.

In Fig. 3.8 the selectivity for different input frequencies and jitter magnitudes is plotted, normalized to the selectivity without jitter. As could be expected, the selectivity deteriorates if jitter is present in the delays. For high input frequencies the sensitivity to temporal jitter is largest. For low frequencies, say $\lesssim 25$ Hz, both models are quite robust and can cope with temporal jitter up to ~ 10 ms. A jitter of about 20% of the input periodicity leads to roughly 50% decrease in selectivity. The amount of jitter thus determines the fastest input periodicity that can still be identified. For a temporal jitter of 1 ms this upper limit is approximately 200 Hz.

3.6 Discussion

3.6.1 Performance limits

The capability to distinguish different frequencies hinges on the fact that the delay times Δ are well known and constant. Only then is it possible to reliably assign a particular frequency to the output neurons. In reality the time it takes for the signal to complete the delay line may vary somewhat.

As shown in section 3.5.6 the system works best for relatively low frequencies up to about 200 Hz. Even if the delay were much more accurate than has been suggested here, it would not be possible to detect very high frequencies reliably. The width of the post-synaptic current response presents a fundamental limit to the delay time that can be detected. In the experimental literature it has been found that AM sensitivity reaches a frequency as high as 1000 Hz but the vast majority of neurons is sensitive to modulation frequencies in the range of 10–300 Hz, most of them lying in the even more restricted range of 30–100 Hz. This finding is valid for various animals [140, 143, 153, 154, 155]. Relevant biological stimuli on the water surface and in spider webs also tend to contain most of their information in the low frequency range $\lesssim 250$ Hz [173][239]. These findings agree very well with the simulations and calculations presented here.

In section 3.3 it was made clear that the delay times Δ need not necessarily arise from a direct connection between two neurons but that they could be the result of a number of interneurons. These interneurons then have to be driven by a very reliable synapse: every input spike should trigger an output spike, and the delay between input and output spike should be fixed. A very prominent example of such a reliable "one-to-one" synapse in the auditory pathway is the so-called *Calyx of Held* at the end of the auditory nerve.

Although this specific type of reliable synapse is only found in the lower auditory pathway its existence demonstrates that fast and reliable synapses are present in the auditory system, a neuronal system of exceptional acuity. For example, in the mammalian auditory brain-stem nuclei neurons can preserve the relative timing of action potentials passed through sequential synaptic levels [164]. In the avian auditory system, too, single presynaptic stimuli can produce short (and thus precise) suprathreshold spikes with a time constant of about 0.5 ms resulting in reliable information transmission [169]. Another possibility to reliably transfer precisely-timed signals is the use of synfire chains [27]. Depending on the input strength, synfire chains can relay information with a temporal precision around 1 ms, accurate enough for use in long-delay feedback and feedforward loops.

Thus, one can conclude that relatively long and well-defined delay times Δ can be realized in biological systems by means of interneurons, posing no fundamental problem to the models.

3.6.2 Conclusions

In this chapter, a quantitative analysis of two different models of periodicity detection has been presented. It was shown that both a feedforward architecture and a recurrent loop architecture can be used to extract periodic modulation from input signals. Furthermore, a mathematical characterization has been provided. It has been shown that for both approaches the basic constraints are the same.

As expected, neuronal time constants are a limiting factor for recognizing the periodicity of the input modulation. The non-zero width of the response kernel theoretically limits modulation recognition to about $\lesssim 1000$ Hz. In real biological systems, however, the limiting factor will probably be the accuracy of the delay Δ. Using an estimate $\delta\Delta \approx 0.5$ ms cuts down the accessible detection range to about 200 Hz. This value is reasonably close to the reported limitation of $\lesssim 300$ Hz in biological systems.

Another limitation common to both feedforward and recurrent circuitries is that they detect only the highest modulation frequency components in any signal. Since activity in high-frequency

channels also excites low-frequency channels it is not possible to distinguish subharmonics of a high-frequency signal from a direct low-frequency input. The known phenomenon of the missing fundamental fits well into the behavior of such a simple network for periodicity extraction. Equivalent to the above is the fact that every neuron responds not only to its own specific frequency but also to all of its harmonics. Consequently the perceived similarity between tones one octave apart from each other [122, 123, 134] and the interference of harmonic target-distractor combinations at low frequencies [113] are a natural side-effect of the proposed architecture.

The two models differ in their behavior as far as their robustness is concerned. By design, the recurrent network is much more susceptible to noise and, as a consequence, can be disturbed by noise more easily than the feedforward model. This is a common problem of excitatory recurrent networks in general since in such networks perturbations tend to amplify themselves.

It has been shown that without any specialized architectural features—a generic neuron model and simple delay lines—the modulation frequency components of a signal can be resolved neuronally. Considering the simplicity of the setup, the models already show remarkable properties that are in good agreement with experimental data. It must be stressed that no parameter tuning was needed to obtain these results.

A small number of input neurons suffices to sample the input signal with a high enough accuracy, and neuronal parameters lie in the range of milliseconds, comparable to typical auditory time scales. If a cochlea is present, signal processing is further facilitated by the prior frequency decomposition but the presence of a cochlea is certainly no prerequisite for periodicity analysis. The output of the networks could be enhanced by postprocessing mechanisms. For example, lateral inhibition can be used to detect and sharpen the peaks in the output (consider Figs. 3.4, 3.5 and 3.6 in this regard).

At this point, it should be noted that *extracting* the slowly-varying envelope from an input signal is easily accomplished biologically. Half-wave rectification of the signal and low-pass filtering suffice. This can be done by a slow synapse filtering out all high frequency components, a mechanism that has been demonstrated explicitly to work in the electric fish sensory pathway [182]. Even if the slow envelope of the signal has been extracted, however, the frequency of the envelope oscillations is still unknown. The models presented here, on the contrary, are able to *identify* the frequency of the envelope oscillations. This is of great biological importance since recognition of sounds often depends on the ability to quantitatively determine the periodicity of the input signal.

As an example, human speech consists of several frequency bands that are comodulated by a guttural fundamental frequency called the *voicing frequency* or *fundamental frequency* [108]. A speaker can be distinguished by his own voicing frequency and this immediately suggests a mechanism for the identification and separation of people speaking simultaneously. It is possible to separate contributions from different speakers by focussing attention on specific periodicity frequencies. The now isolated sound source can then be localized using standard mechanisms based on interaural time differences (ITD) recognition, since phase locking to the input remains intact throughout the processing in both models. In such a setting, auditory object recognition would therefore occur before the localization of the object. This agrees with previous experimental work showing that spatial separation of sounds is indeed linked to comodulation of the signal amplitude across several frequency channels [119, 120, 142].
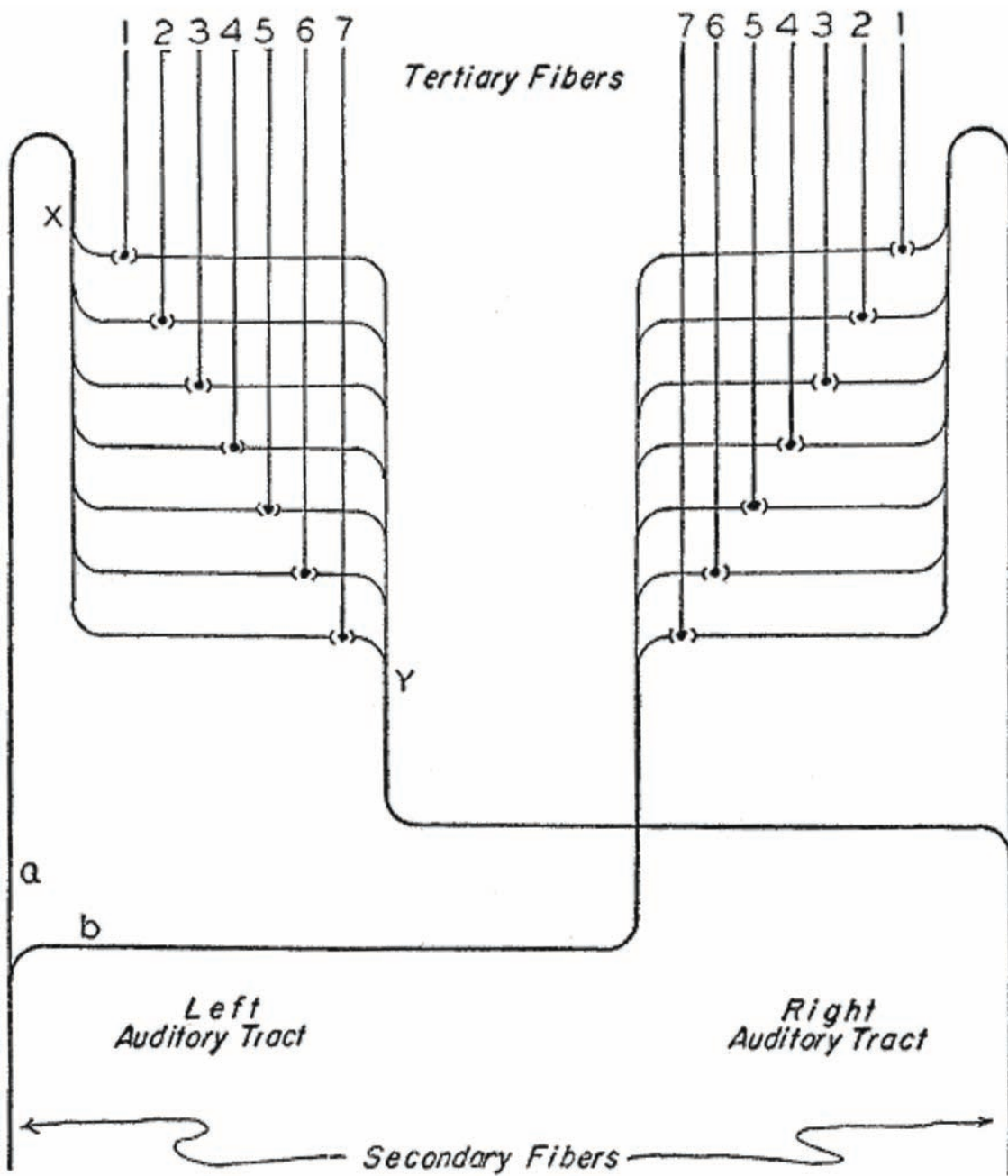
Jeffress was one of the first researchers to suggest an explicit mechanism to form a map-like representation of spatial sensory information. The original illustration of his model of auditory spatial localization (explained in section 2.4.2) is shown here. Diagram taken from [136].

*Ideaal is natuurlijk een voetgangersoversteek-
plaats met een stoplicht plus een ratelapparaat,
voor als er iemand voorbij komt die én blind én
doof is.*

Herman Finkers

4. Multimodal integration and tuning of sensory input

*Multimodal maps play an important role in sensorimotor behavior. An important characteristic
of such maps is that all individual input sensory systems are aligned with each other. Since
the input sensory maps are not aligned at birth, this alignment must be learned. This chapter
discusses two models that can be used for tuning sensory maps. Through a mathematical analysis
and numerical simulations it is demonstrated that a learning mechanism based on inhibitory
teacher input performs superior to a mechanism using an excitatory teacher signal.*[1]

4.1 Introduction

In section 1.5, representation of sensory input and motor commands in neuronal maps was discussed.
An especially interesting role is played by multimodal maps (reviews in [77, 101, 102]). In a
multimodal map, most neurons respond to more than one sensory modality. Such maps are
omnipresent in the brain [86], and it has even be questioned whether genuine monosensory maps
exist at all [102]. A multimodal neuron is defined by its responsiveness to sensory input from more
than one modality.

Several types of interaction are possible if multiple input modalities are stimulated simultaneously
[99, 102]. Very often, the presence of multiple input modalities leads to an increase in firing rate.
This means that the response to two or more simultaneous stimuli is larger than that to either
stimulus when presented alone. Alternatively, a response depression may be found. In this case,
the firing rate decreases if several modalities are activated concurrently. A neutral response is of
course also possible. Then a neuron does respond to several different modalities, but there is no
clear response enhancement or reduction.

A general feature of multimodal maps is that all sensory modalities are spatially aligned. This
means that the spatial response of the neuron is not primarily defined by the type of input that is
present, but rather by the spatial location of that input. Commonly, neural responses are enhanced
if multiple sensory inputs are present at the same location, depression is found if the inputs come
from slightly different spatial positions, and no depression or increase is found if the inputs are far
apart. However, all conceivable types of multimodal interaction are found. A nice example is the
interplay between visual and infrared input in the optic tectum (OT) of rattle snakes [197, 208].

A response enhancement may be super- or subadditive. In the former case, the neuron responds
stronger to the presence of several stimuli than to each stimulus alone, but the combined response is

---

[1] The results presented in this chapter have been published together with J. Leo van Hemmen [79].

still less than the sum of the individual responses. In the latter case, the summed response exceeds even the sum of the individual responses. Such a superadditive response is in particular found for low stimulus amplitude [99]. The response to a faint sound for instance is much more enhanced by simultaneous visual input than the response to a loud sound, which is quite large already.[2]

There are a couple of advantages if neurons are sensitive to more than one modality. First, the chance that any given neuron responds to any event occurring in the vicinity of the animal is larger if this neuron receives input from several sensory systems.

Second, a multimodal response can be used to increase the saliency of multimodal stimuli, especially if superadditive interaction is present. If one assumes that all neurons in a population "compete for attention", those neurons which fire at a high rate have better chances that their output reaches higher layers in the brain for further processing. Many important events have a *multimodal fingerprint*. A predator, for instance, will produce moving visual input, smell, and an auditory input as well, compared to the static and quit sensory input caused by vegetation. The neurons that code for the location of the predator will thus fire at a high rate, enabling attention to be shifted quickly towards the hunter. In short: interesting input leads to a higher firing rate.

Third, multimodal interaction allows for rapid and precise information processing (e.g. object identification) since several pieces of information (e.g. sound, appearance, smell) can be dealt with simultaneously.

The fourth advantage of multimodal responses is higher robustness and reliability of the system. If one or more modalities fail (e.g. because it is dark or the animal is in a noisy environment), this can be compensated by the remaining modalities that are working properly.

For multimodal maps to be of any use, the input from all participating modalities must be calibrated so that a stimulus at a specific spatial location is represented at an unambiguous location on the multimodal map. Ultimately, all sensory modalities together are used to initiate motor responses. Such responses must of course be unequivocal. This provides another argument why sensory maps must be in proper register with each other. Such an alignment of sensory and motor maps is not present at birth and must be *learned* through experience [89, 102].

In this chapter, the question how sensory maps can be aligned to form a calibrated representation of multisensory space will be answered. There are two problems to be solved here. The first problem is that of dynamic adaptation. Many animals can move their sensory organs (eyes, ears, whiskers, etc.) independently of their body. This means that a continuous *dynamical* map alignment is needed. The mechanism underlying this adaptation is not known, but it seems that retinotopic coordinate systems play a key role [80]. Sensory information is often transferred into retinal coordinates using an eye position signal (see discussion in [102]). In addition to this spatial adaptation, temporal contiguity needs to be considered. Since some modalities (notably the auditory pathway) relay their information much faster than others, inputs from different sensory systems cannot be assumed to arrive at the same time in a given multimodal brain region. This problem is dealt with because multimodal neurons can typically integrate inputs over time scales up to 100 ms. Dynamical alignment problems will not be further discussed in this dissertation.

The second problem has to do with the *development* of multimodal alignment. Even if it is clear how dynamic alignment can be achieved, the question remains how static alignment is to be achieved in the first place. A possible answer to this question is given in this chapter, but first a short overview of the relevant research on this topic is presented.

---

[2] Superadditive enhancement can be understood from a probabilistic point of view. The firing rate can be taken to code for the probability that something "noteworthy" presents itself in the spatial receptive field of the neuron. If multiple sensory systems are active simultaneously, this increases the likelihood that something interesting is happening within the receptive field of the neuron. This is encoded through a more than proportional increase in the firing rate. The effect is strongest for small signals [76]

4.1.1 Mechanisms in the development of multimodal integration

For many animals it has been shown that visual input is essential in guiding the development of other sensory systems and multimodal integration. Early work was done on hamster and ferret. Mooney et al. found that somatosensory spatial receptive fields in the superior colliculus (SC) of hamsters are disorganized following destruction of visual input pathways [95]. King et al. have shown that neonatal rotation or lateral deviation of the eye could lead to abnormal auditory spatial maps in the SC [88].

Similar findings were obtained in the cat [103, 104], the clawed frog [175], and in snakes [191]. In psychophysical experiments using congenitally blind and normally sighted subjects, it was shown that in humans multimodal integration also partially depends on visual input in early life for accurate development [82, 97, 98]. Audio-visual integration in barn owls has been studied in great detail (for example reviewed in [89]). This case will be discussed in much more detail below.

It has been shown recently that visual cortex long-term potentiation and depression in mice develops sequentially [84]. Plasticity is gradually lost in development and layers that come later in the processing pathway lose their plasticity later than earlier processing layers. Apparently, the visual cortex layers only settle into their final state after earlier layers have stabilized. The work by Jiang et al. [84] also seems to support the idea that neuronal map formation is often guided by stabilized visual "teacher" input.

Much of the work on multimodal integration has been done in the superior colliculus (SC) or its non-mammalian homologue the optic tectum (OT). Both are known to be a major site of multimodal integration. Inputs from several sensory systems converge in the SC and are used to initiate motor responses [96, 100, 101].

Audio-visual integration in barn owls
In the barn owl, the integration of visual and auditory information has been studied particularly well. The barn owl is an interesting object of study since it is a highly specialized auditory hunter and, in addition, its eyes have a fixed position in the head, preventing any problems related to dynamical coordinate transformations. A variety of experiments, reviewed in [89], have shown that in barn owls integration of auditory and visual input is not functioning optimally in young hatchlings but needs to be learned during several weeks of training in an environment with both visual and auditory stimulation.

Although it has been shown both theoretically and experimentally that an imprecise) map of azimuthal sound source location can be learned in the absence of any visual input [87, 91], a map of sound source elevation cannot be correctly learned without visual information during development. Proper integration of the auditory and visual modality is of course also impossible without visual input.

Input from the visual and auditory system in the barn owl converges in the OT. The last processing stages of the auditory pathway just before the OT are the central nucleus of the inferior colliculus (ICC) and the external nucleus of the inferior colliculus (ICX). Knudsen and his coworkers fitted barn owls with prisms displacing the view field of the animals. This was seen to lead to a change in the auditory input to the OT.

The synaptic connections between ICC and ICX changed in such a way that the auditory map in the ICX acquired the topography of the visual input (Fig. 4.1). The connections between ICX and OT did not change. That is, the multimodal map itself was not adapted, but rather the last input stage *before* multimodal integration was gauged to ensure proper alignment of the visual and auditory input to the multimodal map in the OT.

furthermore, it has been shown that visual input provides a *topographic* teaching input to guide plasticity in the ICC-ICX pathway [83, 90]. This means that plasticity is not induced through a global "error signal" telling the neurons what to do, but rather on a per-neuron basis. It is even possible to induce differently-sized shifts in different parts of the map. Although the precise nature
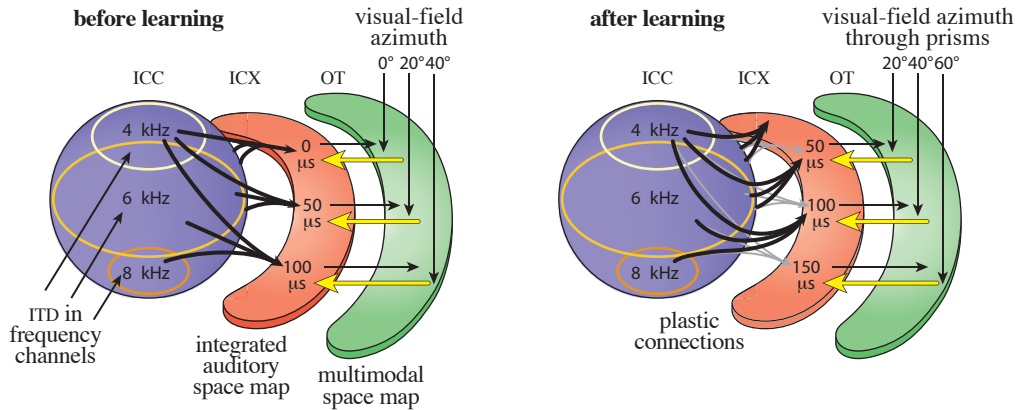
Figure 4.1: *Audio-visual integration in barn owls. In the "normal" situation (left), auditory positional information reaches the ICC in frequency-specific channels. Information on sound source localization is coded in the time-of-arrival difference (ITD) of the sound between the two ears. The frequency-specific maps from the ICC are integrated and relay to the ICX. From there, information is forwarded to the OT where it is integrated with visual input. There is a permanent feedback signal from the OT to the ICX (yellow).*

If abnormal visual input is present (an azimuthal shift is introduced), the feedback signal is used to reorganize the synaptic connections between ICC and ICX to re-establish a match between the map in the ICX and the OT.

Figure redrawn and adapted from [89].

of this teaching signal has not been clarified, inhibitory gain control, or gating, seems to play an important role [81, 106].

It will be shown in this chapter that the presence of inhibitory teacher input is essential for precise and quick tuning of input to multimodal maps.

4.1.2 Two possible models of map tuning

Some time ago Davison and Frégnac [78] presented a mechanism based on spike-timing-dependent plasticity (STDP) that can account for map integration and coordinate transformation between different (sensory) maps. In their model, an array of output neurons receives excitatory input from an input modality and also from a set of teacher neurons. Because of the correlations between the firing rates of the input and teacher neurons, STDP causes strengthening of the "correct" input-to-output connections. In due time the output layer neurons learn to form a topographic spatial representation, even if the teacher input is removed later on.

In this chapter two different methods based on supervised STDP used to gauge input from different sensory modalities and ensure proper map alignment will be discussed. The first model is very much like the one from [78] discussed above, using excitatory input and teacher neuron populations. The second model uses *inhibitory* teaching input (details in section 4.2 below) instead of excitatory teaching input.

A complete mathematical treatment of the learning process is possible, based on the methods developed by Kempter et al. [57]. Such an analysis is presented in section 4.3. In addition, extensive numerical simulations are used to demonstrate the behavior of both learning models (section 4.4).

It will become clear that both models are very robust with respect to parameter variation and noise, but inhibition-mediated learning (IL) is much faster and more robust still than excitation-mediated learning (EL). Furthermore, the quality of the resulting map is not limited by the quality of the teacher signal but rather by the accuracy of the input from the other sensory modality.
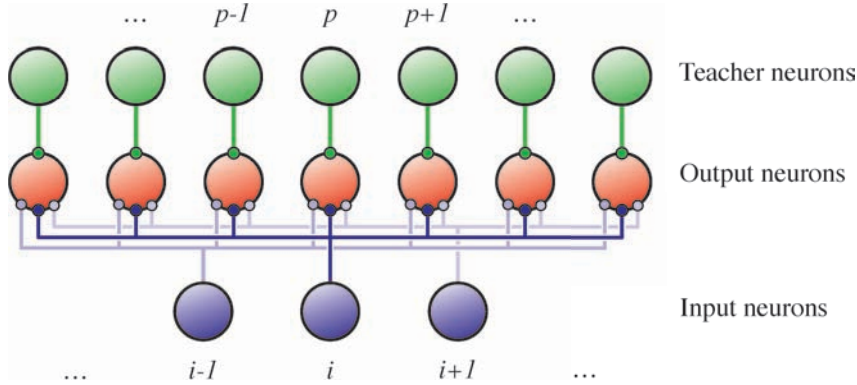
Figure 4.2: *Network topology of the models. There are three layers of neurons. The input layer (I, corresponding to ICC) and the teacher layer (T, corresponding to OT) fire with a rate that depends on the input position y. The output layer (O, corresponding to ICX) is driven by spikes from the input and teacher layer. The synaptic connections from input to output layer are subject to plastic weight changes and the connections from the teacher layer to the output layer remain fixed. Every output neuron receives spikes from one corresponding teacher neuron and from all input neurons.*

4.2 Description of the models

4.2.1 Network topology

For both models a network consisting of three neuron populations is considered (Fig. 4.2). There is an *input* population (I) and a *teacher* population (T) that fire in response to an external sensory stimulus. These two populations are connected to an *output* population (O). The teacher neurons are topographically connected to the output neurons. Every teacher neuron connects to exactly one corresponding output neuron. At the beginning of the learning process the input population is connected to the output population through an all-to-all feedforward network of synapses. The connections between the teacher population and the output population can be either excitatory or inhibitory (see next section) and are considered as fixed. The synapses between the input population and the output neurons are subject to learning through STDP (see section 4.2.3).

The teacher neurons exhibit a map-like response to an external sensory stimulus. That is, each teacher neuron (labeled by index p) has a preferred stimulus position x_p^T, that varies smoothly along the array of teacher neurons.[3] Without loss of generality, all stimulus positions are taken to lie between 0 and 1. The preferred stimulus position of a teacher neuron is then

$$x_p^T = \frac{p-1}{N^T - 1} \, , \tag{4.1}$$

where $p \in [1, N^T]$ is the teacher neuron index and N^T denotes the number of teacher neurons.

The input neurons (labeled by index i) are also tuned to specific directions, denoted by x_i^I. Although a topographical organization of the input neurons is mostly assumed here, this is certainly not a necessary condition (see section 4.4.4).

Before learning starts the synaptic connections are not yet structured and the output neurons do not have a directional preference. During learning an output neuron acquires a preferred stimulus direction that is determined by the preferred direction of the teacher neuron connected to it. Since teacher neurons and output neurons are connected one-to-one, the output neurons are labeled by the same index (p) as the teacher neurons.

---

[3] This chapter is restricted to one-dimensional maps. The approach can be generalized easily to include two-dimensional maps, but the computational costs of simulating learning in such a two-dimensional system become very large, due to the large number of synapses needed.

4.2.2 Sensory input and response of the output population

In the numerical simulations all neurons are modeled as Poisson neurons (see appendix B.2.1). Although this neuron model is very simple, it captures some very important aspect of neuron firing. First, neuronal firing is to some degree stochastic and second, explicit time-dependence of firing probabilities is taken into account. Because of the simplicity of this neuron model, an exact mathematical understanding of the learning process is possible [57].

It is important to note that the Poisson neuron model used here is *not* simply equivalent to a rate coding. Since spike generation is explicitly taken into account, the theory and simulations are much richer than they would be with a pure rate-based modeling approach. In addition, the firing rate functions can have an arbitrary time dependence.

If sensory input is present at position $y \in [0,1]$, the teacher and input neurons fire at a rate λ that depends on the neuron's preferred position

$$\lambda_i^I = A^I g(x_i^I, y) \qquad \text{input population ,} \qquad (4.2\text{a})$$

$$\lambda_p^T = A^T h(x_p^T, y) \qquad \text{teacher population .} \qquad (4.2\text{b})$$

The constants A^I and A^T give the amplitude of the firing rate, and g and h are normalized to have a maximal value of 1. The function g describes the receptive field properties of the input neurons. Typically, g depends on the difference between the input position y and the neuron's preferred position x_i^I, with its maximum for $x_i^I = y$.

As stated above, the teacher-output connections can be either excitatory or inhibitory.

Excitatory teacher input
In the excitatory case (EL) the function h behaves in the same way as described above for g, with a dependence upon the difference between input position and preferred position and maximal value for $x_p^T = y$ (Fig. 4.3, left). For a given stimulus position y, the output neurons corresponding to the teacher neurons with $x_p^T \approx y$ receive strong teacher input, and the other output neurons remain silent. In addition, input from all input neurons will arrive at the output population. Since the input neurons with $x_i^I \approx y$ fire at a high rate, STDP selectively strengthens the connections between input neurons and output neurons that encode the same stimulus position y. After learning, a map will have been built in the output population. This map then responds correctly to the input population alone.

Inhibitory teacher input
In the case of inhibitory teacher input (IL), h behaves differently. The firing rate will be close to zero for teacher neurons with $x_p^T \approx y$, and maximal for neurons that code for any wrong position (Fig. 4.3, right). The output neurons are therefore strongly inhibited, except for a few neurons that correspond to the teacher neurons that are minimally active. This mechanism is called *selective disinhibition*. The output neurons that are not inhibited can fire freely and are now solely driven by the input population. Again, STDP potentiates connections between input neurons and output neurons that code the same position and weakens the wrong connections.

As will become clear below, both EL and IL allow for a topographical map to develop in the output population. This map is aligned with the teacher map, and after learning the output neurons respond correctly to the input neurons even if no teacher signal is present. Still, the learning process in the two models differs in one important aspect. Because with IL, the output population's firing is determined solely by the input population, the output neurons are trained to respond correctly to the input population *only*. In the case of EL, the output population learns to optimally react to a *combination* of input from the input population and the teacher population. This has two major consequences.
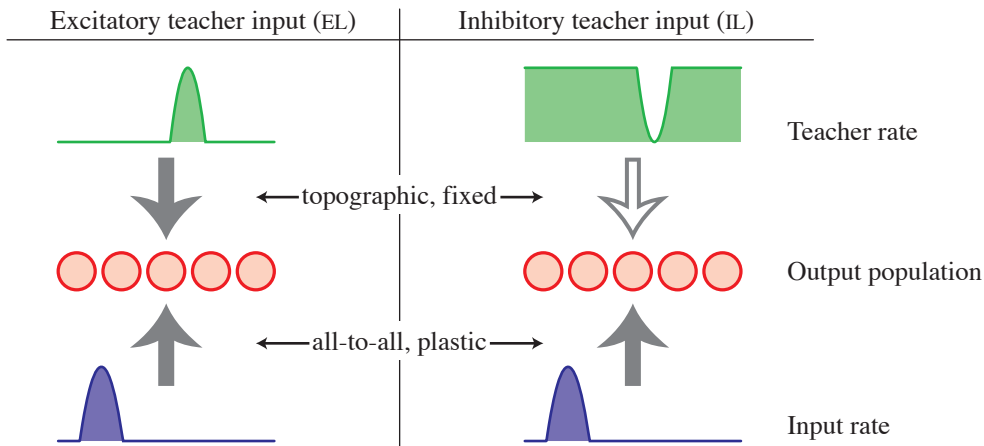
Figure 4.3: *Firing rates of input and teacher population. Both the input and the teacher population are organized in a map. For an external stimulus at a certain location, the firing rate strongly peaks at a well-defined location in the input and the teacher map. The input and teacher map can, however, be misaligned. The output population receives spikes from the input and from the teacher layer.*
Left: In the EL model, the output neurons receive excitatory input from both the input and the teacher population. The output neurons corresponding to the teacher neurons with the highest rate will fire most, and the connections from the active input neurons to this set of output neurons will therefore be strengthened by STDP.
Right: In the IL model the output neurons are all silenced by the inhibitory teacher input, except for a small number of neurons receiving no inhibition. These neurons are driven by the input population and—as for the EL model—the connections between the active input neurons and the active output neurons are strengthened.
Both models are able to form a high-quality map based on the input and the teacher signal. The resulting map is automatically aligned with that in the teacher population.

1. With IL, the firing rate of the output neurons is determined solely by the input population. This holds during training, but also if no teaching input is present anymore. That is, after an initial transient at the start of the learning process the output firing rate is always normalized (see for instance [57, 58, 70]). For EL, on the other hand, the output firing rate is determined by the input population *and* the teacher population. This means that the output rate may vary greatly, depending on whether teacher input is present or not.

2. If the temporal structure of the firing of the input neurons is nontrivial (viz., time coding rather than rate coding) it is advantageous to retain this temporal structure also in the output population. If the output neurons receive excitatory input from both the input and the teacher population, the timing cues that are present in the input population spikes are "contaminated" by the simultaneous input from the teacher neurons. In the IL case, the teacher input does not interfere with the input population signal. Any important temporal structure can therefore be retained in the output neuron firing statistics.

Output population firing rate

The rate function λ for the input population and the teacher population is given by Eqs. (4.2a) and (4.2b). The rate function of the output neurons depends on the firing of the input and teacher

neurons. It is given by

$$\lambda_p^O(t) = \left[\sum_{i=1}^{N^I} \sum_f J_{ip}(t_i^f) \varepsilon^I(t - t_i^f) + J^T \sum_g \varepsilon^T(t - t_p^g) \right]^+ . \qquad (4.3)$$

The firing times of the input neurons are denoted by t_i^f, and those of the teacher neurons by t_p^g. The strength of the synaptic connection from input neuron i to output neuron p is given by $J_{ip}(t)$, which is a function of time, and the strength of the connections between the teacher neuron p and the output neuron p is given by J^T. The postsynaptic response of the output neuron to an incoming spike from an input neuron is given by the kernel ε^I, and ε^T is the response kernel for input from the teacher neurons. Since the teaching input may be negative ($J^T < 0$), the total rate function may become negative, which would not make sense for a probability density. To avoid this, half-wave rectification is applied, as indicated by $[\cdots]^+$ (see p. 81).

4.2.3 Learning protocol

Learning trials

To numerically simulate the behavior of the models, the neurons are trained through many learning trials. In a single trial, an input position y is picked from a uniform distribution on $[0, 1]$, and the firing rates of the input and the teacher neurons in response to this input are calculated (see section 4.2.4). The stochastic firing of the input and teacher population is then simulated during a trial of duration $\mathcal{T}$, and the spikes are sent to the output neuron population, which fires in response. The connections between input and output neurons are dynamically adjusted according to the STDP rules specified below.

At regular times during learning, the quality of the map and the amount by which the weights have changed are measured as described in section 4.2.3.

Plasticity rules

Learning in the brain occurs through spike-timing-dependent plasticity (STDP) as discussed in section 1.3.1. Under normal circumstances and for excitatory synapses, presynaptic spikes that come before postsynaptic spikes lead to an increase in the synaptic weight (potentiation) and presynaptic spikes that arrive after a postsynaptic spike has been triggered lead to a weight decrease (depression). The learning window W describes the dependence of the weight change on the difference between pre- and postsynaptic spike timing.

Many factors influence the precise result of any learning trial, but these influences do not radically alter the basic results of STDP-based learning without bells and whistles attached. This chapter is therefore mainly restricted to learning with independent additive weight changes in dependence upon spike timing only. In section 4.4.5 simulations are briefly discussed that take into account some of the parameters that influence learning in addition to spike timing.

The STDP rule used in this chapter consists of three parts,

1. If a presynaptic spike is emitted, the weight of the synaptic connection is changed by an amount ηw^{pre}.

2. If a postsynaptic spike is emitted, the weight of all synaptic input connections to this neuron changes by an amount ηw^{post}.

3. For every pair of a pre- and postsynaptic spike, the synaptic efficacy changes by an amount $W(s)$ that depends on the difference $s = t_{\mathrm{pre}} - t_{\mathrm{post}}$ between the spiking times t_{pre} and t_{post}.

The shape of the learning window is given by

$$
W(s) = \begin{cases} \eta w^+ \dfrac{|s|}{(\tau^+)^2} e^{-|s|/\tau^+} & s < 0 \\[2ex] -\eta w^- \dfrac{s}{(\tau^-)^2} e^{-s/\tau^-} & s \geq 0 \end{cases} .
\tag{4.4}
$$

The overall learning speed is set by the variable η, which should be small. The parameters w^{pre}, w^{post}, w^+ and w^- are all of order 1.

The synapses connecting input and output population have a starting weight of J_0^I and the weights are capped to always stay between the values $J_{\min}^I$ and $J_{\min}^I$. The synapses between teacher and output population are *not* subject to learning.

Only nearest neighbor spike-pair interaction is considered. This seems biologically plausible, since each back-propagating action potential may be thought to reset the voltage in the dendritic spines. Moreover, only the first presynaptic spike after such a postsynaptic reset may be relevant due to saturation effects; see also [56]. The mathematical theory as developed in [57] is only valid for all-to-all spike pairings and for the sake of comparison, simulations are also carried out in which all spike pairs are taken into account (cf. section 4.4.2).

Performance measures
To gain insight into the performance of the models, some measures are needed to assess the quality of the map in the output population and the speed of learning.

Map quality
To measure how well the output map performs for a given weight distribution the expected output firing rate without teaching input is calculated [see also Eq. (4.15)] for 100 input positions y_l ranging from 0 to 1 in equally-sized steps. The expectation of the output firing rate is

$$
\nu_p^O(y) = \sum_i J_{ip} \nu_i^I(y) .
\tag{4.5}
$$

In this equation, ν denotes a time-averaged firing rate over one learning trial of length $\mathcal{T}$. For each input position, the output neuron $p_{\max}$ with the highest firing rate is determined, and the difference between its preferred position $x_{p_{\max}}$ and the input position y_l is obtained. The localization error E_{RMS} of the map is then the root-mean-square (RMS) value of this difference over all 100 input positions

$$
E_{\mathrm{RMS}} = \sqrt{\sum_l \frac{(x_{p_{\max}} - y_l)^2}{100}} .
\tag{4.6}
$$

A small value for E_{RMS} means that the map is of high quality.

Weight change and learning speed
The overall learning speed is set by the parameter η as described above. However, because the two models that are studied here have different connectivity properties, it is not possible to simply compare the performance of both networks for equal values of η. In the EL model, only a small number of teacher neurons are active simultaneously. In the IL model, a majority of the teacher neurons is always active; cf. Fig. 4.3. A measure of learning speed that is independent of this difference is therefore needed.

To obtain such a measure, the RMS distance d_{RMS} is defined as follows

$$
d_{\mathrm{RMS}} = \sqrt{\sum_{i,p} \frac{[J_{ip}(t) - J_{ip}(t=0)]^2}{N^I N^T}} .
\tag{4.7}
$$

d_{RMS} measures the distance between the initial weight distribution and the weight distribution at some later time t. During learning d_{RMS} changes from 0 at $t = 0$ to some maximal value that is almost identical for both models. Let T be the time it takes to reach a value $d_{\mathrm{RMS}} = 0.01$ (about one tenth of its maximal value for the parameters used in this chapter). The learning speed v_{learn} is now defined by

$$v_{\mathrm{learn}} := \frac{0.01}{T} \ . \tag{4.8}$$

Through the learning speed v_{learn} the EL and IL model can be compared in and *objective* way.

4.2.4 Specification of the model variables

The firing rate of the input and the teacher populations are given by a Gaussian dependence upon the difference between the input position y and the neuron's preferred position x_i^I or x_p^T.

For the EL model this means that the functions g and h in Eq. (4.2) are specified to be

$$\lambda_i^I(y) = A^I g(x_i^I, y) = A^I \exp\left(-\frac{(x_i^I - y)^2}{2\,(\sigma^I)^2}\right), \tag{4.9a}$$

$$\lambda_p^T(y) = A^T h(x_p^T, y) = A^T \exp\left(-\frac{(x_p^T - y)^2}{2\,(\sigma^T)^2}\right) \ . \tag{4.9b}$$

and for the IL model

$$\lambda_i^I(y) = A^I \exp\left(-\frac{(x_i^I - y)^2}{2\,(\sigma^I)^2}\right), \tag{4.10a}$$

$$\lambda_p^T(y) = A^T \left[1 - \exp\left(-\frac{(x_p^T - y)^2}{2\,(\sigma^T)^2}\right)\right] \ . \tag{4.10b}$$

The postsynaptic response of the output neurons to an incoming spike from the input population is taken to be an α function (see p.)

$$\varepsilon^I(t) = \alpha(t, \tau^I) \tag{4.11a}$$

while the response kernel for spikes from the teacher neurons is

$$\varepsilon^I(t) = \alpha(t, \tau^T) \ . \tag{4.11b}$$

The preferred position of the teacher neurons is given by (4.1), viz.,

$$x_p^T = \frac{p - 1}{N^T - 1} \tag{4.12a}$$

and the preferred position of the input neurons is

$$x_i^I = \frac{i - 1}{N^I - 1} \ . \tag{4.12b}$$

The learning speed parameter η varies for different simulations and its value is indicated where needed. In table 4.1, the values of all further parameters are listed. Where different parameter values have been used, it is indicated in the text. It is important to realize that no parameter tuning is needed. Both the EL and IL models are robust against parameter variations, and the values in table 4.1 represent reasonable first guesses for the parameters.

parameter	value
network layout	
number of input neurons	$N^I{=}100$
number of teacher neurons	$N^T{=}100$
number of output neurons	$N^T{=}100$
initial strength of input→output synapses	$J_0^I{=}0.1$
minimal strength of input→output synapses	$J_{\min}^I{=}0.0$
maximal strength of input→output synapses	$J_{\max}^I{=}0.25$
strength of teacher→output synapses	J^T (EL)${=}{+}1$
strength of teacher→output synapses	J^T (IL)${=}{-}1$
postsynaptic response time to input spike	$\tau^I{=}10$ ms
postsynaptic response time to teacher spike	$\tau^T{=}25$ ms
learning parameters	
learning trial length	$\mathcal{T}{=}0.5$ s
simulation time step	$\Delta t{=}0.5$ ms
weight change upon input spike	$w^{\mathrm{pre}}{=}1.5$
weight change upon output spike	$w^{\mathrm{post}}{=}{-}4.0$
learning window potentiation amplitude	$w^+{=}4.0$
learning window depression amplitude	$w^-{=}1.0$
learning window potentiation time	$\tau^+{=}20$ ms
learning window depression time	$\tau^-{=}40$ ms
integral over learning window	$\widetilde{W}{=}3\eta$ s
integral over learning window and response kernel	$\overline{W}{=}29.6\eta$
input and teacher signal	
input tuning curve amplitude	$A^I{=}50\,\mathrm{s}^{-1}$
teacher tuning curve amplitude	$A^T{=}100\,\mathrm{s}^{-1}$
input tuning curve width	$\sigma^I{=}0.015$
teacher tuning curve width	$\sigma^T{=}0.025$

Table 4.1: *Model parameters as used in the analytical calculations and numerical simulations. The value of the learning parameter η varies for different simulations. It is always explicitly specified where needed. The precise values of the parameters are not important. There is a wide range of parameters that enable stable learning (see also the discussion in section 4.3).*

4.3 Mathematical analysis of learning

An exact analytical description of the learning process can be given using the methods developed in [57]. Such a description is quite technical. The problem is that the weight change of a single synapse is determined by the activity of both pre- and postsynaptic neuron. The postsynaptic activity is in turn determined by the activity of all presynaptic inputs and synaptic strengths connecting to this neuron. This means that the weight change of a synapse is interconnected with the weight changes of all other synapses contacting the same output neuron. Before discussing specific results for the EL and IL model, the general form of the learning equation is derived.

4.3.1 The learning equation

The first step is to focus on a single stimulus that is applied at position y. The evolution of the synaptic weights is given by the *learning equation* [57]. For the network architecture used here it

reads

$$\dot{J}_{ip}(t) = w^{\mathrm{pre}}\nu_i^I(y) + w^{\mathrm{post}}\nu_p^O(y) + \int_{-\infty}^{\infty} \mathrm{d}s\ W(s)C_{ip}(s,t,y)\,, \tag{4.13}$$

where the overdot denotes differentiation with respect to time. The learning parameters w^{pre}, w^{post} and the learning window W have been defined in section 4.2.3. The quantities ν_i^I and ν_p^O are the time-averaged expectation values of the input rate and the output rate, respectively. $C_{ip}(s,t)$, finally, is the time-averaged expectation value of the correlation between the spike trains of input neuron i and output neuron p,

$$C_{ip}(s,t) = \overline{\langle S_i^I(t+s)S_p^O(t)\rangle} \tag{4.14}$$

where the brackets denote the expectation value over stochastic realizations of the Poisson process and the overbar denotes the time average over one learning trial of length $\mathcal{T}$. Furthermore, S_i^I denotes the spike train of the input neuron i, and S_p^T is the spike train of the teacher neuron p.

The time-averaged mean input firing rate is just $\nu_i^I(y) = A^I g(x_i^I, y)$ from (4.2a). The time-averaged mean output rate is

$$
\begin{aligned}
\nu_p^O(y) &= \overline{\left[\sum_i J_{ip}(t)\int_0^{\infty}\mathrm{d}t'\ \varepsilon^I(t')\lambda_i^I(t-t') + J^T\int_0^{\infty}\mathrm{d}t'\ \varepsilon^T(t')\lambda_p^T(t-t')\right]^+}\\
&= \left[\sum_i J_{ip}(t)\nu_i^I + J^T\nu_p^T\right]^+\,.
\end{aligned}
\tag{4.15}
$$

The second equality holds because the firing rate functions $\lambda^{I/T}$ are constant in this case and $\int_0^{\infty}\mathrm{d}t\ \varepsilon^{I/T} = 1$.

The expectation of the correlation between input and output spike train is more difficult to obtain. The definition results in

$$\langle S_i^I(t+s)S_p^O(t)\rangle = \left\langle S_i^I(t+s)\left[\sum_j J_{jp}S_j^I(t) + J^T S_p^T(t)\right]^+\right\rangle\,. \tag{4.16}$$

Depending on whether the teacher input is excitatory ($J^T > 0$) or inhibitory ($J^T < 0$), a different result is obtained for the right-hand side of (4.16).

4.3.2 The learning equation for excitatory teacher input

Form of the learning equation
When the teaching input is excitatory ($J^T > 0$), the rectification in (4.16) does nothing since the argument is already positive. The correlation can then be calculated straightforwardly (for detailed methods see [57]), giving

$$C_{ip}(s,t) = \nu_i^I\left(J^T\nu_p^T + J_{ip}(t)\varepsilon^I(-s) + \sum_j J_{jp}(t)\nu_j^I\right)\,. \tag{4.17}$$

The learning equation (4.13) then becomes

$$\dot{J}_{ip} = \sum_j \underbrace{\nu_j^I\left(w^{\mathrm{post}} + \widetilde{W}\nu_i^I + \delta_{ij}\overline{W}\right)}_{A_{ij}} J_{jp} + \underbrace{w^{\mathrm{pre}}\nu_i^I + J^T(w^{\mathrm{post}} + \widetilde{W}\nu_i^I)\nu_p^T}_{B_{ip}} \tag{4.18}$$

with the definitions

$$\widetilde{W} = \int_{-\infty}^{\infty} \mathrm{d}s \ W(s) \, , \quad \overline{W} = \int_{-\infty}^{\infty} \mathrm{d}s \ W(s) \varepsilon^{I}(-s) \, . \tag{4.19}$$

It is very important to note that the *precise form* of the learning window has disappeared from the equation. Only the two integrals over the $W(s)$ defined above play a role.

For every output neuron p, Eq. (4.18) reduces to a matrix-vector equation describing the weight evolution of its input connections:

$$\dot{\mathbf{J}}^{(p)} = \mathsf{A} \cdot \mathbf{J}^{(p)} + \mathbf{B}^{(p)} \, . \tag{4.20}$$

The vector $\mathbf{J}^{(p)}$ contains all the input connections to the output neuron p, and the components of the matrix A and the vector $\mathbf{B}^{(p)}$ are taken from (4.18). The notation stresses that $\mathbf{B}^{(p)}$ depends on which output neuron p is considered. A is the same for all output neurons.

The matrix A and vector $\mathbf{B}^{(p)}$ give the response of the system to sustained input at some particular input position y. To find the average learning result over all positions, the expectation value of (4.20) with respect to y is to be calculated. Such an expectation value, denoted by a hat, is given by

$$\hat{h} = \int_{0}^{1} \mathrm{d}y \ \rho(y) h(y) \, , \tag{4.21}$$

where $\rho(y)$ specifies the probability distribution of the variable y. Taking this average is allowed if learning proceeds slowly enough.

The assumption that all positions are equally likely (justified by the learning protocol, see section 4.2.3) gives $\rho(y) = 1$ and for the components of A and $\mathbf{B}^{(p)}$ this leads to

$$\hat{\mathsf{A}}_{[ij]} = \left(w^{\mathrm{post}} + \delta_{ij} \overline{W} \right) \xi_{j}^{1} + \widetilde{W} \xi_{ij}^{2} \, , \tag{4.22a}$$

$$\widehat{\mathbf{B}}_{[i]}^{(p)} = w^{\mathrm{pre}} \xi_{i}^{1} + w^{\mathrm{post}} J^{T} \xi_{p}^{3} + \widetilde{W} J^{T} \xi_{ip}^{4} \tag{4.22b}$$

where δ_{ij} is the Kronecker delta ($\delta_{ij} = 1$ if $i = j$ and $\delta_{ij} = 0$ if $i \neq j$), and

$$\xi_{i}^{1} = \int_{0}^{1} \mathrm{d}y \ \nu_{i}^{I}(y) \, , \tag{4.23a}$$

$$\xi_{ij}^{2} = \int_{0}^{1} \mathrm{d}y \ \nu_{i}^{I}(y) \nu_{j}^{I}(y) \, , \tag{4.23b}$$

$$\xi_{p}^{3} = \int_{0}^{1} \mathrm{d}y \ \nu_{p}^{T}(y) \, , \tag{4.23c}$$

$$\xi_{ip}^{4} = \int_{0}^{1} \mathrm{d}y \ \nu_{i}^{I}(y) \nu_{p}^{T}(y) \, . \tag{4.23d}$$

The complete evolution of the weights for excitatory learning input is thus described by

$$\dot{\mathbf{J}}^{(p)} = \hat{\mathsf{A}} \cdot \mathbf{J}^{(p)} + \widehat{\mathbf{B}}^{(p)} \tag{4.24}$$

together with (4.22) and (4.23).

Interpretation of the learning equation
The complete equation (4.24) can be solved exactly using Duhamel's formula,

$$\mathbf{J}^{(p)} = \mathsf{S} \cdot \exp(\Lambda t) \cdot \mathsf{S}^{-1} \cdot \left(\mathbf{J}_{t=0}^{(p)} + \hat{\mathsf{A}}^{-1} \cdot \widehat{\mathbf{B}} \right) - \hat{\mathsf{A}}^{-1} \cdot \widehat{\mathbf{B}} \, . \tag{4.25}$$

In this solution, S is the matrix containing as columns the eigenvectors of $\hat{\mathsf{A}}$ and Λ the matrix containing the eigenvalues of $\hat{\mathsf{A}}$ on its diagonal. The matrix S diagonalizes $\hat{\mathsf{A}}$ and therefore $\mathsf{S}^{-1}\hat{\mathsf{A}}\mathsf{S} = \Lambda$.

Unfortunately, this solution is of limited use, since the maximal and minimal values of $\mathbf{J}^{(p)}$ are not taken into account. It therefore makes more sense to focus on the values of the ξ's (4.23) to understand how the learning equation (4.24) behaves. Because the input neurons and the teacher neurons are tuned to specific positions, the averaged firing rates $\nu_i^I(y)$ and $\nu_p^T(y)$ are large if the neuron's preferred position matches y ($x_i^I \approx y$ or $x_p^T \approx y$), and zero if the positions do not match. If the width of the tuning curves is not too large, the integrals in Eq. (4.23) can be extended to range from $-\infty$ to ∞, since only a small domain lying completely within $[0, 1]$ will give a significant contribution anyway.

The value of ξ_i^1 is then just a constant independent of i that is given by the total area under the tuning curve of the input neurons. Similar reasoning applies to ξ_p^3. The value of ξ_{ij}^2 sharply peaks for $x_i^I \approx x_j^I$ (meaning that $i \approx j$) and if the input neurons are organized topographically, this implies that ξ_{ij}^2 is a square matrix with large values around the main diagonal and values very close to zero elsewhere. The same reasoning applies to ξ_{ip}^4. The matrix entries ξ_{ip}^4 are large when $x_i^I \approx x_p^T$ and very small if this is not the case. For the input and teacher firing rates defined in Eq. (4.9) the following expressions are found,

$$\xi_i^1 = A^I \sigma^I \sqrt{2\pi}\,, \tag{4.26a}$$

$$\xi_{ij}^2 = (A^I)^2 \sigma^I \sqrt{\pi} \exp\left(-\frac{(x_i^I - x_j^I)^2}{4\,(\sigma^I)^2}\right)\,, \tag{4.26b}$$

$$\xi_p^3 = A^T \sigma^T \sqrt{2\pi}\,, \tag{4.26c}$$

$$\xi_{ip}^4 = A^I A^T \frac{\sigma^I \sigma^T}{\sqrt{(\sigma^I)^2 + (\sigma^T)^2}} \sqrt{2\pi} \exp\left(-\frac{(x_i^I - x_p^T)^2}{2\,[(\sigma^I)^2 + (\sigma^T)^2]}\right)\,. \tag{4.26d}$$

Parameter dependence of the learning equation

The entries in $\hat{\mathsf{A}}$ and $\widehat{\mathbf{B}}^{(p)}$ can be directly calculated from the parameters in table 4.1. Apart from the parameters $A^{I/T}$, $\sigma^{I/T}$, and $w^{\mathrm{pre/post}}$, the entries are determined by $\widetilde{W}$ and $\overline{W}$. For the parameter set used here, the entries of $\hat{\mathsf{A}}$ and $\widehat{\mathbf{B}}^{(p)}$ are explicitly given by

$$\hat{\mathsf{A}}_{[ij]} = \left[-7.52 + 55.6\,\delta_{ij} + 199 \exp\left(-\frac{(x_i^I - x_j^I)^2}{2\,(0.021)^2}\right)\right] \times \eta\,, \tag{4.27a}$$

$$\widehat{\mathbf{B}}_{[i]}^{(p)} = \left[-22.2 + 484 \exp\left(-\frac{(x_i^I - x_p^T)^2}{2\,(0.029)^2}\right)\right] \times \eta\,. \tag{4.27b}$$

Note that all values are scaled by the learning parameter η. What, then, do Eqs. (4.24) and (4.27) mean?

For a wide parameter range, the matrix $\hat{\mathsf{A}}$ has large positive values around the diagonal and small negative values away from the diagonal. The vector $\widehat{\mathbf{B}}^{(p)}$ has large positive values for $x_i^I \approx x_p^T$ and small negative values otherwise. If learning starts, the weight distribution is still unstructured. This implies that $\hat{\mathsf{A}} \cdot \mathbf{J}^{(p)} \approx \alpha \mathbf{J}^{(p)}$ for some number α that depends on the precise values of the parameters. $\hat{\mathsf{A}}$ causes all weights to increase or decrease by a fixed amount. For the parameters used here, α happens to be about zero and the initial weight evolution is dominated by $\widehat{\mathbf{B}}^{(p)}$. Even if weight evolution is *not* dominated by $\widehat{\mathbf{B}}^{(p)}$, $\hat{\mathsf{A}}$ does not cause structure formation during the initial stages of learning.

The vector $\widehat{\mathbf{B}}^{(p)}$ causes the weights for which $x_i^I \approx x_p^T$ to increase and the others to decrease. In this way a seed of structure is generated, and because of the diagonal form of $\hat{\mathsf{A}}$ this structure

is further increased. At the end all weights connecting input and output neurons with $x_i^I \approx x_p^T$ are maximal, and all other weights vanish. Thus, the EL model indeed leads to correct structure formation and the development of a map in the output neuron population.

As stated above, the "right" learning is obtained for a wide range of parameters. Correct learning occurs because $\hat{A}$ has a diagonal structure with negative entries away from the diagonal. Similarly, $\widehat{\mathbf{B}}^{(p)} > 0$ for $x_i^I \approx x_p^T$ and $\widehat{\mathbf{B}}^{(p)} < 0$ otherwise. The conditions that must be satisfied by the parameters to ensure this behavior are as follows:

- $w^{\text{post}} < 0$. This condition must always be satisfied for weight stabilization to occur [57].

- $w^{\text{pre}} > 0$. This condition makes biological sense since synapses that receive much presynaptic input tend to be strengthened.

- $\overline{W} > 0$. This condition is always satisfied because of the definition (4.19).

- $\widetilde{W}$ may be positive or negative. If it is negative, the absolute value may not be larger than $\left|\overline{W}\right|$. It needs, however, quite an extreme shape of the learning window for this to happen.

- $\sigma^{I/T} \ll 1$. This means that the input and teacher signal are localized sufficiently well. This condition is just a mathematical statement of the fact that input and teacher signal are organized in a map-like fashion.

These conditions are all rather weak. A very broad range of biologically realistic parameters can be chosen that satisfy these conditions. The EL model is therefore very robust with respect to parameter variation.

4.3.3 The learning equation for inhibitory teacher input

Form of the learning equation

If $J^T < 0$ the rectification in (4.16) leads to problems. Since rectification is a nonlinear operation, it cannot simply be pulled out of the expectation value. This problem can be solved by taking a slightly different form for the teacher signal. Instead of taking Eq. 4.10b, it is assumed that inhibition is very large for inputs $\left|y - x_p^T\right| > \sigma^T$ so that the output neuron is perfectly silent. For $\left|y - x_p^T\right| < \sigma^T$ the teacher signal vanishes completely and the output signal is only determined by the positive contributions from the input neurons. This is called *shunting inhibition*. Then, the correlation term becomes

$$\left\langle S_i^I(t+s)S_p^O(t) \right\rangle = \left\langle S_i^I(t+s)\sum_j J_{jp}S_j^I(t) \right\rangle \theta(\sigma^T - \left|x_p^T - y\right|), \qquad (4.28)$$

with θ as Heaviside step function (p. 82). The temporally averaged mean is given by (using again the methods outlined in [57])

$$C_{ip}(s,t) = \nu_i^I \left(J_{ip}(t)\varepsilon^I(-s) + \sum_j J_{jp}(t)\nu_j^I \right) \theta(\sigma^T - \left|x_p^T - y\right|). \qquad (4.29)$$

The learning equation (4.13) now becomes

$$\dot{J}_i^{(p)} = \sum_j \nu_j^I \underbrace{\left(w^{\text{post}} + \widetilde{W}\nu_i^I + \delta_{ij}\overline{W} \right) \theta(\sigma^T - \left|x_p^T - y\right|)}_{D_{ijp}} J_{jp} + \underbrace{w^{\text{pre}}\nu_i^I}_{E_i}. \qquad (4.30)$$

The position-averaged learning equation can be written

$$\dot{\mathbf{J}}^{(p)} = \widehat{\mathsf{D}}^{(p)} \cdot \mathbf{J}^{(p)} + \widehat{\mathbf{E}} \,, \tag{4.31}$$

and the expectation values over the input y are now

$$\widehat{\mathsf{D}}^{(p)}_{[ij]} = \left(w^{\text{post}} + \delta_{ij}\overline{W}\right)\zeta^1_{jp} + \widetilde{W}\zeta^2_{ijp} \,, \tag{4.32a}$$

$$\widehat{\mathbf{E}}_{[i]} = w^{\text{pre}}\zeta^3_i \tag{4.32b}$$

where

$$\zeta^1_{jp} = \int_0^1 \mathrm{d}y \; \nu^I_j(y)\,\theta(\sigma^T - \left|x^T_p - y\right|) \,, \tag{4.33a}$$

$$\zeta^2_{ijp} = \int_0^1 \mathrm{d}y \; \nu^I_i(y)\nu^I_j(y)\,\theta(\sigma^T - \left|x^T_p - y\right|) \,, \tag{4.33b}$$

$$\zeta^3_i = \int_0^1 \mathrm{d}y \; \nu^I_i(y) \,. \tag{4.33c}$$

4.3.4 Interpretation of the learning equation

To understand the complete learning equation (4.31) in the case of inhibitory teacher input, a closer look at the ζ's as defined in (4.33) is needed. As in the case of excitatory teacher input, the integrals in (4.33) are extended to run from $-\infty$ to ∞. This leads to

$$\zeta^1_{jp} = \int_{x^T_p - \sigma^T}^{x^T_p + \sigma^T} \mathrm{d}y \; \nu^I_j(y) \,, \tag{4.34a}$$

$$\zeta^2_{ijp} = \int_{x^T_p - \sigma^T}^{x^T_p + \sigma^T} \mathrm{d}y \; \nu^I_i(y)\nu^I_j(y) \,, \tag{4.34b}$$

$$\zeta^3_i = \int_{-\infty}^{\infty} \mathrm{d}y \; \nu^I_i(y) \,. \tag{4.34c}$$

It can be seen that ζ^1_{jp} peaks for $x^I_j \approx x^T_p$ and is very small elsewhere. Furthermore, ζ^2_{ijp} has a maximal value if $x^I_i \approx x^I_j \approx x^T_p$ and is nearly zero otherwise. Finally, ζ^3_i is constant.

Using the rates from Eq. (4.10) to explicitly calculate the ζ's gives

$$\zeta^1_j = A^I \sigma^I \sqrt{\pi/2}$$
$$\times \left[\operatorname{erf}\left(\frac{x^T_p - x^I_j + \sigma^T}{\sqrt{2}\sigma^I}\right)\right.$$
$$\left. - \operatorname{erf}\left(\frac{x^T_p - x^I_j - \sigma^T}{\sqrt{2}\sigma^I}\right) \right] \,, \tag{4.35a}$$

$$\zeta^2_{ijp} = (A^I)^2 \sigma^I \sqrt{\pi/4}\exp\left(-\frac{(x^I_i - x^I_j)^2}{4\,(\sigma^I)^2}\right)$$
$$\times \left[\operatorname{erf}\left(\frac{2x^T_p - (x^I_i + x^I_j) + 2\sigma^T}{2\,\sigma^I}\right)\right.$$
$$\left. - \operatorname{erf}\left(\frac{2x^T_p - (x^I_i + x^I_j) - 2\sigma^T}{2\,\sigma^I}\right) \right] \,, \tag{4.35b}$$

$$\zeta^3_i = A^I \sigma^I \sqrt{2\pi} \tag{4.35c}$$

where "erf" denotes the error function defined on p. 82.

Parameter dependence of the learning equation

Just as for the EL model above, the learning equation describing the evolution of the input weights to a specific output neuron p reduces to a vector-matrix equation. The shape of the learning window is again found to be irrelevant and only $\widetilde{W}$ and $\overline{W}$ enter the equation. For the parameter values from table 4.1 the matrix and vector components are

$$
\widehat{\mathsf{D}}_{[ij]}^{(p)} = \left\{ 27.8 \left(\delta_{ij} - 0.135 \right) \right.
$$

$$
\times \left[\mathrm{erf} \left(47.1 \left(x_p^T - x_j^I \right) + 1.18 \right) \right.
$$

$$
\left. - \mathrm{erf} \left(47.1 \left(x_p^T - x_j^I \right) - 1.18 \right) \right]
$$

$$
+ 99.7 \exp \left(-\frac{(x_i^I - x_j^I)^2}{2 \, (0.021)^2} \right)
$$

$$
\times \left[\mathrm{erf} \left(33.3 \left(2x_p^T - x_j^I - x_i^I \right) + 1.67 \right) \right.
$$

$$
\left. \left. - \mathrm{erf} \left(33.3 \left(2x_p^T - x_j^I - x_i^I \right) - 1.67 \right) \right] \right\} \times \eta \,, \tag{4.36a}
$$

$$
\widehat{\mathbf{E}}_{[i]} = 2.82 \times \eta \,. \tag{4.36b}
$$

In contrast to the EL case the vector $\widehat{\mathbf{E}}$, being constant, plays no role in structure formation. The matrix $\widehat{\mathsf{D}}^{(p)}$ allows for more interesting behavior.

Although $\widehat{\mathsf{D}}^{(p)}$ looks impressive, its behavior is relatively simple. For a large absolute value of its argument, the error function becomes either -1 or 1. This implies that the differences between the error functions in $\widehat{\mathsf{D}}^{(p)}$ vanish if the separation between x_p^T on the one hand and $x_{i/j}^I$ on the other hand is too large. If $x_j^I \approx x_p^T$ holds, the value of $\widehat{\mathsf{D}}^{(p)}$ is positive if $i \approx j$, and negative otherwise. Calculating $\widehat{\mathsf{D}}^{(p)} \cdot \mathbf{J}^{(p)}$ shows that $\mathbf{J}_{[i]}^{(p)}$ is increased if $x_i^I \approx x_p^T$, and decreased otherwise.

It is still possible that $\widehat{\mathbf{E}}$ interferes with the weight evolution by increasing all weights. Since $\widehat{\mathbf{E}}$ is directly proportional to the product of A^I and σ^I this simply means that the input neurons should not fire too strongly (A^I and σ^I should not be too large). If they would, all weights would evolve towards their maximal value because the input neurons are completely dominating the firing of the output neurons in spite of the inhibition from the teacher map.

The remaining conditions under which the analysis presented here is valid are identical to those discussed for the EL model. If these conditions are fulfilled, a stable weight distribution evolves with strong connection between input and output neurons if their preferred positions match, and weak connections if the preferred positions do not match.

The above mathematical analysis shows that the synaptic weights converge to the correct set, leading to an accurate spatial representation in the output neurons. However, this analysis was limited to the case of all-to-all spike interactions, which need not be biologically realistic (see section 4.2.3). Fortunately, numerical tests have shown that including or dropping all-to-all interactions does not alter the results obtained in this chapter. Below, results of numerical simulations are discussed. These results are then used to further analyze the performance of the EL and IL model.
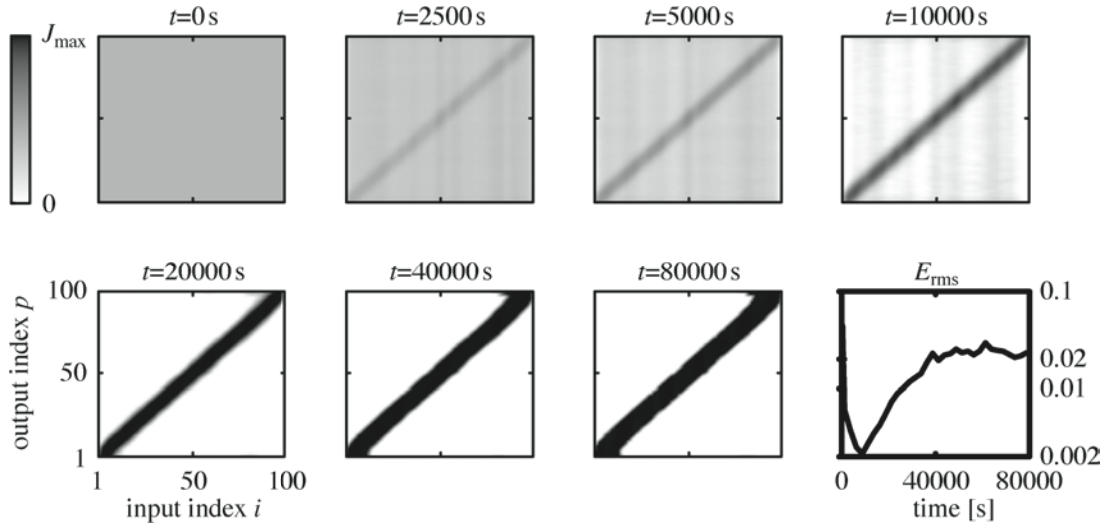
Figure 4.4: *Weight evolution for* EL *with* $\eta = 3 \cdot 10^{-7}$. *The development of a map-like organization is clearly visible as time progresses. The total learning time is in the order of days. The localization error quickly drops to a small value and then slowly approaches a steady-state value, here about 2%.*

4.4 Numerical simulations

In this section, results of numerical simulations are discussed. The learning procedure of section 4.2 has been programmed using the C++ programming language. In the first two subsections, the results for EL and IL are compared with each other and with the analytical results from section 4.3. The most important results will be that inhibition-mediated learning is faster and more accurate than excitation-mediated learning.

The third subsection discusses coordinate transformations between the input and the output map. In addition, map restructuring is analyzed. Although both excitation- and inhibition-mediated learning are able to learn a coordinate transformation, only the IL model is able to drastically restructure *existing* maps. The inhibition-based model is therefores studied in more detail in the last two subsections (sections 4.4.4 and 4.4.5).

4.4.1 Comparing excitatory and inhibitory teacher input

At the start of the discussion, it is useful to get a basic idea of the typical course of the learning process. In Fig. 4.4 the weight distribution at various times during learning is displayed for EL with learning parameter $\eta = 3 \cdot 10^{-7}$.

Horizontally, the preferred position of the input neurons is shown, and vertically, the preferred position of the output neuron as dictated by the learning population. The synaptic strength of the input→output connections is gray-coded. At the lower right of the figure the evolution of the localization error is shown (see section 4.2.3). Clearly visible in the figure is the strengthening of the correct synaptic connections starting from a homogeneous synaptic strength distribution.

Typically, E_{RMS} first drops to a very low value as the weights on the central diagonal get strengthened. As the diagonal band of strong weights broadens, the quality deteriorates to a certain extend. In this case, the accuracy stabilizes at about 2%.

Figure 4.5 shows the RMS deviation [Eq. (4.7)] of the weights from their starting value, and the evolution of the localization error [Eq. (4.6)] for several values of η. Although the learning parameter η varies by a factor of 100, all learning trials show the same behavior. After an initial
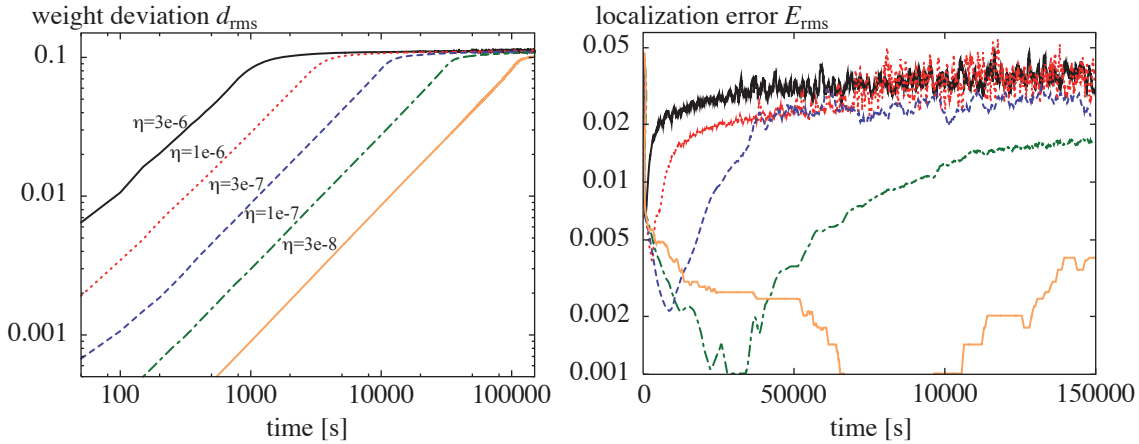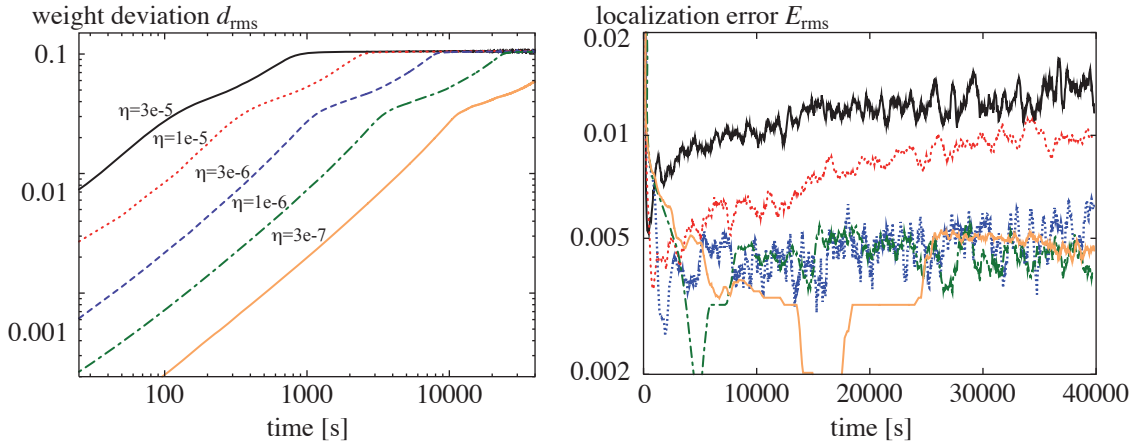
Figure 4.5: *The* RMS *deviation of the weights [left, according to Eq. (4.7)] and the* RMS *error [right, according to Eq. (4.6)] for several values of the learning parameter η in the* EL *case. The vertical scale is logarithmic in both panels. For a large range of η values a steady increase in d_{RMS} is observed. The maximal value of d_{RMS} is always approximately 0.1. The final value of E_{RMS} decreases with the value of η, but even for relatively quick learning, the final error stays below 5%.*
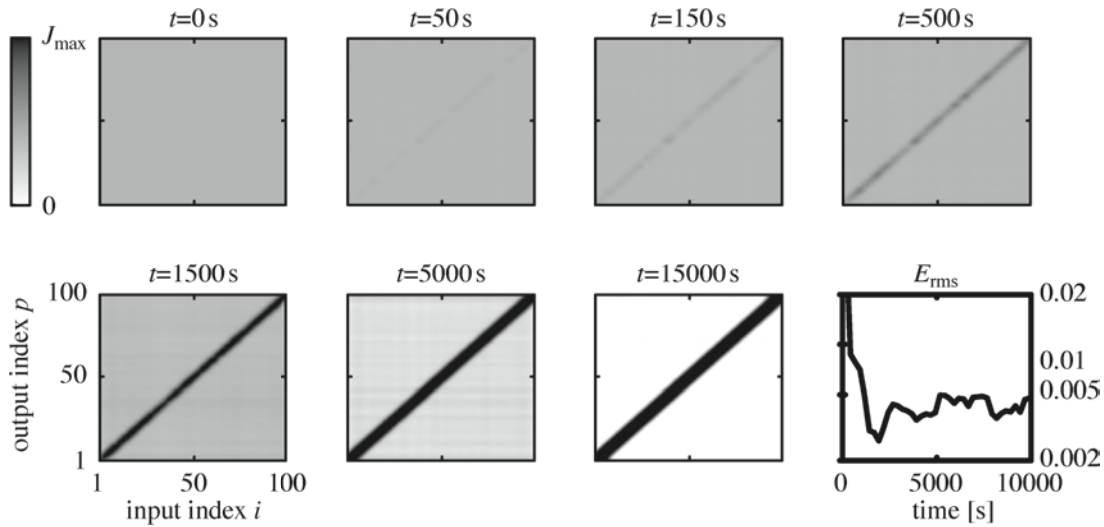
Figure 4.6: *Weight evolution for* IL *input with $\eta = 3 \cdot 10^{-6}$. As in the* EL *case, map formation is clearly visible. In contrast to Fig. 4.4, map evolution proceeds much faster than in the* EL *case. Only several hours of learning time are needed.*

drop of the localization error the quality slowly climbs towards its final value. If smaller values of η are used, the final map quality improves.

In Figs. 4.6 and 4.7 the same plots are shown for the case of inhibitory teacher input with $\eta = 3 \cdot 10^{-6}$. The results are very similar, but there is an important difference. For inhibitory teacher input, the localization error is much smaller than with excitatory teacher input, even if the learning speed is much larger (compare the time scales and the development of the error in Figs. 4.4 and 4.6).

As suggested by Figs. 4.4 to 4.7, the IL scheme is quicker and more accurate than the EL scheme.

Figure 4.7: *The* RMS *deviation of the weights [left, according Eq.* (4.7)*] and the* RMS *error [right, according to Eq.* (4.6)*] for several values of η in the* IL *case. Here too the vertical scales are logarithmic. The same picture as in Fig.* 4.5 *arises. The weight deviation converges to 0.1 and the localization error E_{RMS} decreases for smaller values of the learning speed. The final error ($< 2\%$ even for fast learning) is decidedly smaller than in the* EL *case.*
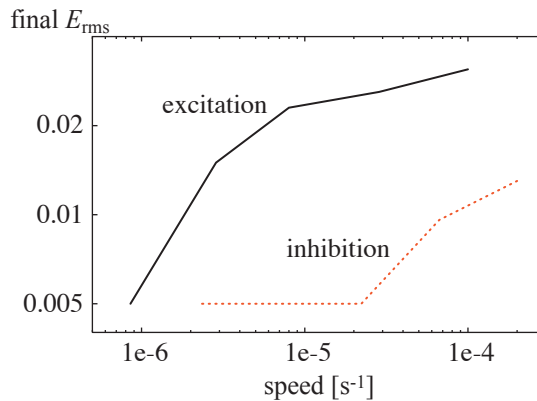
Figure 4.8: *Localization error versus learning speed for excitatory and inhibitory learning input [Eqs.* (4.6) *and* (4.8)*]. The speed of the learning process basically measures the time it takes for the weight distribution to change significantly. Clearly,* IL *outperforms* EL*: at equal values of the learning speed, the quality of the map learned with the* IL *model is far better than the quality of the map formed with the* EL *model. This implies that the* IL *model is more robust than the* EL *model.*

Figure 4.8 makes this difference explicit. If the final E_{RMS} is plotted against the learning speed as calculated by means of Eq. (4.8), there is a large difference between EL and IL. For IL, map quality is very good even for high learning speeds. In practice, the final map quality is reached within a couple of hours learning time. For EL, much slower learning is needed (in the order of days) for the model to remain stable and even then, the final map quality is poor as compared to the quality achieved by IL. Due to the finite number of neurons, the map quality cannot become arbitrarily small, there is a plateau at an error of $\approx 0.5\%$. Decreasing the learning speed any further to obtain a better map is impossible.
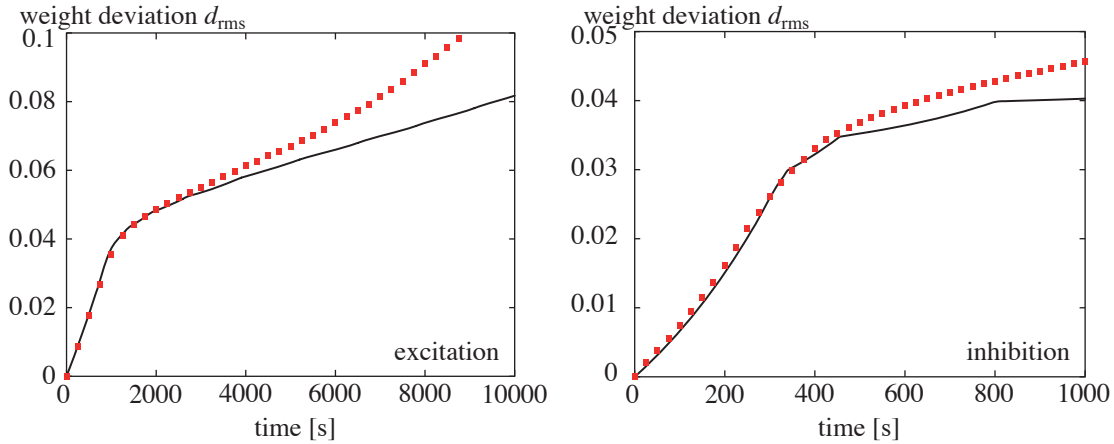
Figure 4.9: *Comparing analytical (solid black) and numerical (dotted red) results for* EL *(left) and* IL *(right). All spike pairs are taken into account instead of just neighboring spike pairs (see also the discussion in section 4.2.3). For* EL $\eta = 3 \cdot 10^{-7}$ *and for* IL $\eta = 3 \cdot 10^{-6}$.
For both models, the analytical and numerical results fit very well. After the first synaptic strengths reach a value $J_{\max}^I$, *the capping of the weights introduces a nonlinearity into the model, and the theoretical description breaks down. This explains the deviation of the theoretical and numerical curves in these plots.*

4.4.2 Comparison with analytical results

This section compares the analytical results from section 4.3 with numerical simulations. To arrive at the analytical result, the deterministic Eqs. (4.24) and (4.31) were integrated, taking into account that the weights must always stay within the range $[J_{\min}^I, J_{\max}^I]$. Figure 4.9 shows the comparison between mathematical theory and numerical experiments for EL and IL.

The agreement between theory and numerical simulation is excellent, proving that the mathematical framework developed in section 4.3 indeed provides a valid description.

Unfortunately, theory does not remain valid throughout the whole learning process. As soon as some of the weights reach the value $J_{\min}^I$ or $J_{\max}^I$, these weights are not allowed to decrease (increase) any further. This cutoff introduces a nonlinearity into the description of the weight change and the theory does not hold any more. The result is that the theoretical curve diverges from the numerical simulation results from $t \approx 2500\,\text{s}$ for EL and $t \approx 400\,\text{s}$ for IL. Here, the seconds are formal ones, depending on the timescale set by η.

4.4.3 Learning spatial transformations

Throughout this chapter, it has been tacitly assumed that the neuronal maps in the input and teacher population are similar. That is, both maps are organized in such a way that the preferred location increases smoothly from 0 to 1 from the leftmost to the rightmost neuron. In reality, this need not be the case.

A good example of such a flexible transformation is provided by the experiments of Knudsen and coworkers [92, 93]. If barn owls with normal visual and auditory capabilities are equipped with prism glasses that shift their visual field, the auditory map in the ICX changes to reflect this deviation. Here, a rather drastic version of this experiment is simulated. After learning has been completed and a stable map is formed, the teacher input is *completely* reversed (Knudsen et al. only introduced a moderate shift in the visual input).

The weight distribution after learning (see Fig. 4.6) is now the starting point for the simulations, but the teacher map will be inverted. That is, the teacher neurons now have a preferred position
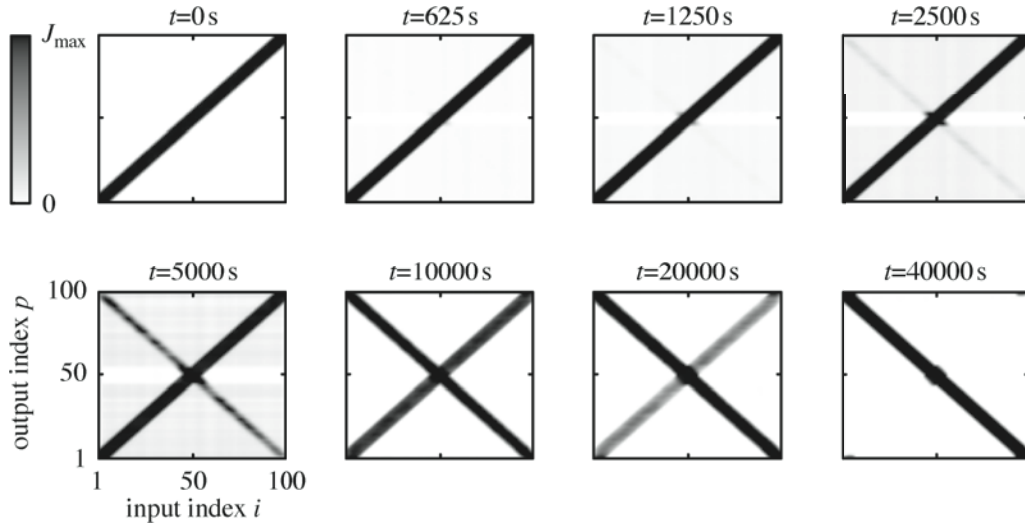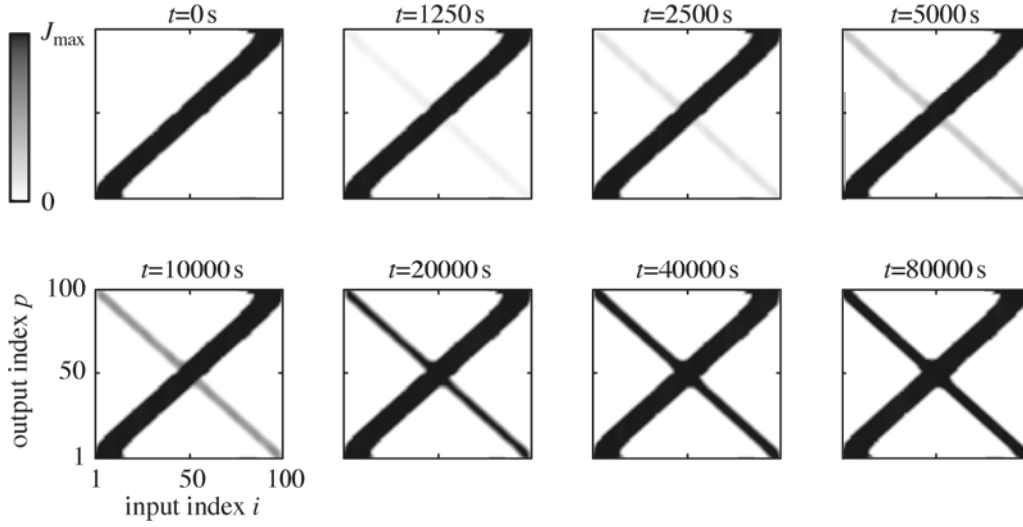
Figure 4.10: *Weight evolution after inverting the teacher map for the IL model. The weights change to form a radically altered map in the output population within just a couple of hours learning time. The quality of the newly developed map is nearly as good as the quality before restructuring.*

running from 1 to 0 instead of a preferred position running from 0 to 1. Based on the new teacher input, the output neurons must learn the correct transformation and the weights connecting input and output population must radically change in order to completely reverse the output map.

The result of this simulation using the IL model is displayed in Fig. 4.10. Clearly, dramatically altering an existing map is unproblematic with inhibition-mediated teacher input. The quality of the resulting inverted map is just as good as that of the original map.

For excitatory learning, the picture is quite different. Although the antidiagonal structure forms correctly, the original diagonal band never vanishes. This is shown in Fig. 4.11. Although there is no teacher input present to strengthen the old—now incorrect—connections, they stay in place solely because of the excitatory input they receive from the input population. If an inhibitory teacher signal is present, this ensureres that the incorrect connections are actively weakened. Reorganizing the map is then unproblematic.

Another example of a spatial transformation has been discussed by Davison and Frégnac [78]. They analyzed the transformation between two cortical maps, one of these containing the angle between upper and lower arm as measured by the proprioceptive system and another one encoding the spatial position of the hand as perceived by the visual system. The coordinate transformation between these two maps is effectively a sine function. Davison and Frégnac showed that such a transformation can indeed be learned using their model, which is very much like the EL model discussed here. Below, it is demonstrated that such a transformation can also be achieved easily through the IL model.

In this test the preferred position of the teacher population is not given by Eq. (4.12a), but instead by a sine function,

$$x_p^T = \frac{1}{2}\left[1 + \sin\left(2\pi\frac{p-1}{N^T-1}\right)\right] . \tag{4.37}$$

The preferred position of the input population is still given by Eq. 4.12b. The result of the corresponding simulation is shown in Fig. 4.12. As was to be expected, learning a sinusoidal transformation is unproblematic in the IL model.

Figure 4.11: *Weight evolution after inverting the teacher map for the* EL *model. The weights change to form a new antidiagonal structure. The old main diagonal remains in place, however, and this leads to a useless map. Since there is no inhibition from the teacher map, the input population can sustain strong connections from the situation before reorganization.*
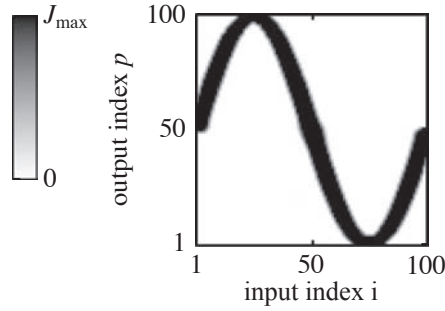

Figure 4.12: *Final weight distribution after a sine-transformation has been learned. Clearly, the* IL *model can be used to account for the learning of coordinate transformations between different modalities.*

4.4.4 Influence of noise

The above comparison of EL and IL suggests that inhibitory learning is quite robust; even at high learning speed, stable learning occurs and radical alterations of the weight distribution are possible. Here the robustness of the IL model with respect to noise is tested in three separate test cases.

In the first test, noise is added to the firing rates of the input and teacher neurons as given by Eqs. (4.9) and (4.10). For each learning trial, when a stimulus at one particular position y is presented, the input firing rate of each input neuron is changed according to

$$\lambda_i^I \to \lambda_i^I \cdot (1 + \chi_i) \tag{4.38}$$

with χ_i a Gaussian distributed stochastic variable with mean 0 and standard deviation 0.25. The teacher firing rate is changed in the same way.

In the second test, the initial weights are not all taken equal but instead the input weights J_{ip} are randomly chosen from a Gaussian distribution with mean J_0^I and standard deviation $0.1J_0^I$.
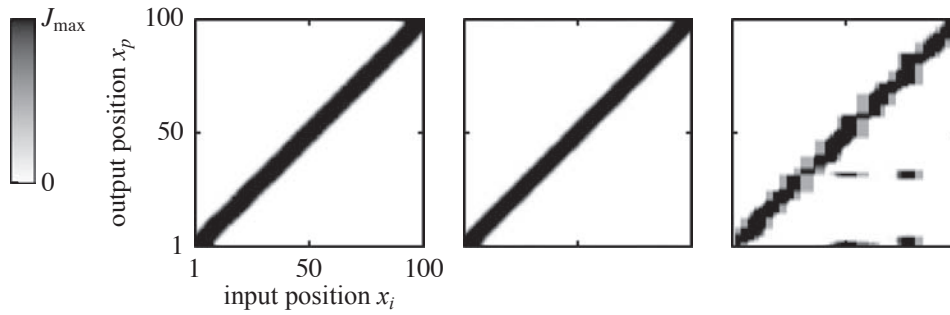
Figure 4.13: *Final weight distribution for several learning runs including noise. Left: noise in input and teacher rate; Middle: random initial synaptic weights; Right: random preferred positions. In all cases the distribution of the synaptic strengths guarantees the presence of a neuronal map in the output layer, although the map is less precise if the input population is not organized in a map.*
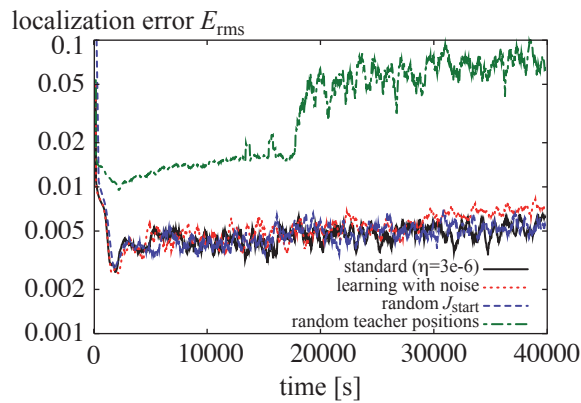
Figure 4.14: *Localization error E_{RMS} if sources of noise are taken into account. Noise in the input and teacher signals and random initial weights do not influence the final quality of the map. If the input neurons are not organized in a map, but rather have random preferred positions, quality is not so good. Still, a localization error below 10% is attained.*

The third test assesses the influence of the absence of map-like organization in the input population. All input neurons do have a preferred position in this setup, but there is no topographical organization. Rather, the preferred direction of every input neuron is randomly taken from a uniform distribution on $[0, 1]$.

The results of these tests are shown in Figs. 4.13 and 4.14. From Fig. 4.13 it is clear that a normal map is built if noise is added to the firing rates or if random input weights are used. This is confirmed by the localization error in Fig. 4.14. In both cases, the output neurons are able to form a high-quality map through STDP.

If the input neurons are not topographically organized the map quality may not become extremely high. Although most output neurons are strongly connected to the correct input neurons, some output neurons get input from the wrong neurons. This is due to the fact that some positions will be "overrepresented" and others will be "underrepresented". This may lead to a chain reaction in which wrong connections from an overrepresented input position start dominating. In the case shown here, the output positions $x_p^O \approx 0.03$ and $x_p^O \approx 0.32$ receive too much input from the wrong input neurons. This causes the poor quality of the output map. In Fig. 4.14 (right) the chain reaction can be recognized. At time $t \approx 18000\,\mathrm{s}$ the localization error suddenly increases. At this time, a stable seed with strong incorrect connections has formed.

If many more input neurons would be present, the change of some positions being under- or overrepresented decreases and the map will have a much higher quality. If, in addition, learning is very slow, the chance that an initial seed of incorrect connections is formed is also smaller.

4.4.5 Influence of model parameters

As discussed in section 4.2.3, linear and independent weight changes are generally used in this chapter. This section further investigates the impact of the learning rules on the simulation results. In addition, the effect of varying the width of the tuning curves of the input and teacher neurons on the learning process is examined.

Multiplicative weight change

Instead of linearly adding weight changes, one might use a learning window in which the weight changes depend on the actual strength of the weight itself. A regularly used learning rule consists of taking a "multiplicative" learning window. This learning window has the following form:

$$
W(s) = \begin{cases}
w^+ \dfrac{|s|}{(\tau^+)^2} e^{-|s|/\tau^+} \cdot (J^I_{\max} - J) & s < 0 \\
-w^- \dfrac{s}{(\tau^-)^2} e^{-s/\tau^-} \cdot J & s \geq 0
\end{cases} .
\tag{4.39}
$$

All parameters used here are identical to those given in table 4.1. The learning window above ensures that the size of weight increases tends to zero as the weight approaches its maximum, and that the amplitude of weight decreases becomes zero as the weight goes to zero. In this way a *soft bound* on the synaptic weight is achieved.

Symmetric weight change

Another possibility is to take a learning window that does not behave in a strictly Hebbian way. Instead of increasing the weight if presynaptic spikes precede postsynaptic spikes and decreasing the weight if a postsynaptic spike precedes a presynaptic spike, a symmetric learning window is taken

$$
W(s) = w^+ \frac{1}{\sqrt{2\pi}\tau^+} e^{-s^2/2(\tau^+)^2} - w^- \frac{1}{\sqrt{2\pi}\tau^-} e^{-s^2/2(\tau^-)^2} .
\tag{4.40}
$$

Again all parameters are as given in table 4.1. Through this window, the weight is increased if pre- and postsynaptic spikes occur in close temporal distance and if the temporal distance is large the weight is decreased. Although this learning rule cannot be used to learn precise temporal structure, correlations between input and output signal can still be learned.

The results of simulations using these two alternative learning windows are shown in Fig. 4.15. There is no influence of altering the learning rules on the quality of the resulting map. Although the learning speed is different for the different rules, the final localization error approaches the same value. In section 4.3 it is shown that indeed learning only depends on the integral over the learning window and on the convolution of the learning window with the output neuron postsynaptic response to input spikes. This simulation confirms that the precise shape of the learning window is irrelevant.

Tuning curve width

As a final numerical experiment, the effect of the accuracy of the input and the teacher neurons has been investigated. It would be expected that a wider tuning curve increases the learning speed [see Eqs. (4.23) and (4.33)], and at the same time decreases the map quality. The behavior of the IL model has been tested for two cases.
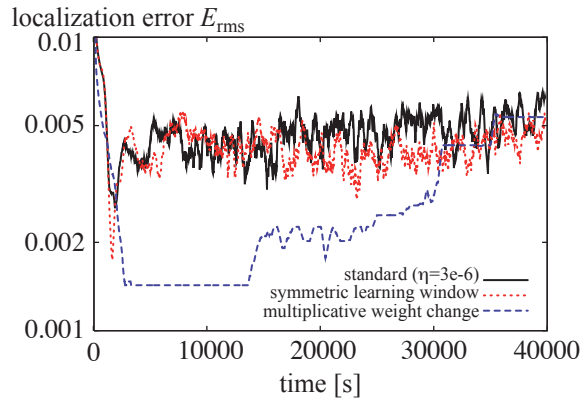
Figure 4.15: *Localization error E_{RMS} for different learning rules. The final localization error does not depend on the precise nature of the learning rule. This finding confirms the mathematical analysis, which predicts that only* integrals *over the learning window are needed to describe the learning process.*
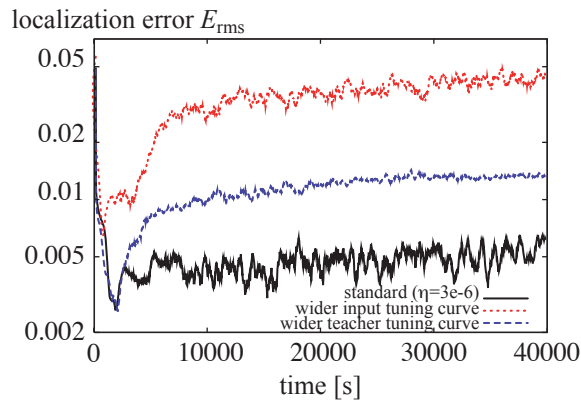

Figure 4.16: *Localization error E_{RMS} for different widths of the tuning curves. A two-fold increase of the width of the teacher tuning curve leads to about the same increase in the localization error. If the width of the input tuning curve is doubled, the error increases approximately five-fold. The quality of the map in the output population thus depends more strongly on the quality of the input map than on the quality of the teacher signal.*

In the first case the width of the input tuning curve (σ^I) was doubled, leaving all other parameters constant. In the second the teacher tuning curve width (σ^T) was doubled. The results are shown in Fig. 4.16.

The figure indicates a clear increase in the localization error if the tuning curve of the input or teacher neurons is wider. If the tuning curve of the teacher neurons is made twice as large, E_{RMS} increases by about the same factor. Changing the input tuning curve has a much larger effect. If σ^I is doubled, the localization error of the output map increases approximately five-fold. Perhaps surprisingly, the quality of the output map is therefore mainly determined by the accuracy of the input neurons and *not* by the precision of the teacher signal.

4.5   Discussion

4.5.1   Inhibitory or excitatory teacher input?

In this last chapter, two different possibilities to gauge neuronal maps using STDP were discussed. Both models can account for map formation based on a topographic teacher template. The first model that suggests itself, using excitatory learning input (EL), is clearly not the most efficient learning paradigm. If inhibitory teacher input (IL) is used, the quality of the map and the learning speed can be expected to be much better. This is because not only strengthening of the correct synaptic connections between input and output layer occurs, but the incorrect connections are also actively suppressed.

Regarding the EL model, the results from this chapter confirm the work done by Davison & Frégnac [78]. Robust map formation is possible and the learning of spatial transformations is no problem. Restructuring of existing maps was not considered by Davison & Frégnac, but it has been shown here that radically altering a completely developed map is not possible by means of an excitatory teacher signal.

The IL model is robust against noise (section 4.4.4) and learning is flexible with regard to parameter variation (section 4.4.5). Spatial transformations can easily be learned and completely developed maps can be radically restructured, as has also been demonstrated biologically (section 4.4.3, compare [92, 93]). This property of the model matches the finding that neuronal maps retain some degree of plasticity even after the developmental stage [85, 93, 94].

Although such an inhibition-mediated learning paradigm need of course not be realized in the brain at every location where neuronal maps are learned, evidence from the barn owl brain [81, 83, 90] strongly suggests that at least in this animal a topographic and inhibitory teacher signal is used.

Especially if map changes must be radical and rapid, the learning algorithm must be very stable. The IL mechanism fulfills this requirement. A complete reorganization of the map such as shown in Fig. 4.10 poses no problem for the IL model but is *not* possible through the EL scheme. With excitatory teacher input it is of course possible to strengthen new synaptic connections, but since the wrong connections are not actively weakened they will continue to exist alongside the newly strengthened ones.

From the work in this chapter it can therefore be predicted that especially if the spatial accuracy and the learning speed of neuronal maps need to be high, inhibition-mediated learning can be expected to play a key role, whereas excitatory-based learning may still do a good job if demands are not so high.

4.5.2   Influence of learning rules and neuron models

Although Hebbian-style plasticity can be implemented in several ways, STDP is the only local mechanism that prevents runaway firing rates and at the same time is able to learn precise temporal input correlations (review in [41]). This chapter has mainly focused on additive weight changes, and a simple neuron model was used to facilitate a mathematical description. As argued above, incorporating more complicated behavior into the learning rules is not expected to not change the results (see sections. 4.2.3 and 4.4.5 and also [64, 71]).

Another question of interest is whether to use all-to-all spike pairings or just neighboring spike pairs. It was argued above that using just neighboring spike pairs is biologically more plausible (see also discussion in [56]). Taking, however, all-to-all spike pairings rather than a finite-range interaction does not change the results of the simulations. Learning proceeds a bit faster if all spike pairs are taken into account, but the map quality again stabilizes at the same level as in the standard case (data not shown).

The shape of the learning window does not strongly influence the learning process. The mathematical analysis has shown that only the integral over the learning window and the convolution of the learning window with the postsynaptic response of the output neurons to input spikes play a role in the dynamics [Eq. (4.19)]. This has been confirmed by numerical simulations (Fig. 4.15).

The fact that the precise shape of the learning window is unimportant has to do with the lack of temporal structure in the input and teacher signal. If for a given input position y the input and teacher rate are constant—as chosen here—the output rate (4.15) will be constant as well. If the firing rates have a richer temporal structure, the mathematical description from section 4.3 breaks down. Preliminary simulations suggest, however, that the output population can learn a map based on temporal features of the input signal. Obviously, this only works for inhibitory teacher input, since excitatory teacher input would interfere with the signal from the input neurons, and the temporal structure would be destroyed. Accordingly, the precise form of the learning window *does* play an important role in learning.

The mathematical discussion explicitly shows the dependence of the learning process upon the model parameters (section 4.3). Especially the width and the amplitude of the tuning curves of the input and teacher neurons are important [as is clear from Eqs. (4.23) and (4.33)]. A wide and high-amplitude tuning curve allows for quicker learning, but of course the resulting map quality is worse, as is brought out by Fig. 4.16.

The effect of the tuning curve width on the accuracy of the resulting map is different for the teacher and the input populations. The dominant influence in determining map accuracy is not the tuning width of the teacher neurons, but rather the precision of the input neurons. It should be possible to experimentally verify this prediction by designing experiments in which learning takes place while the response of one of the input modalities is artificially blurred. For vision and audition this could for example be achieved by equipping animals with distorting glasses or ear plugs.

4.5.3 Origin of the teacher map

One of the questions that remains to be answered is why the visual system always seems to function as a teacher for the other modality. An important property of the visual system is that a spatial map is automatically induced through the input mapping upon the retina *by a lens.* The retina is therefore *intrinsically* ordered in a map-like fashion. Activity waves spreading over the retina have been found in the embryos of many species [107]. Such retinal waves, occurring regularly on a time scale of seconds to minutes, provide coherent input to the visual system, aiding the development of high-quality spatial maps. Even if the animal does not use its eyes, or opens them relatively late in development (as many mammals do), a spatial template from the visual system would be present to guide multimodal integration. In this way, the intrinsic topography from the retina might dictate the organization and alignment of all multimodal maps in the brain.

Appendices

A. Notation

A.1 General issues

Differentiation An overdot means differentiation with respect to time: $\dot{h} = \mathrm{d}h/\mathrm{d}t$.

Fourier transform Fourier transformed functions are generally denoted with a capital letter, whereas functions in the time domain are denoted with a lowercase symbol. The Fourier transform $\mathcal{F}$ is defined as

$$H(\omega) = \mathcal{F}[h(t)](\omega) := \int_{-\infty}^{\infty} \mathrm{d}t \; e^{-i\omega t} h(t) \,. \tag{A.1}$$

The inverse Fourier transform is then

$$h(t) = \mathcal{F}^{-1}[H(\omega)](t) := \frac{1}{2\pi} \int_{-\infty}^{\infty} \mathrm{d}\omega \; e^{i\omega t} H(\omega) \,. \tag{A.2}$$

Root Mean Square In this thesis, several data sets containing both positive and negative numbers are encountered. To quantify the typical magnitude of elements from such a set, the mean is of course not a practical choice. Instead, the root mean square (RMS) value will be used. Given a set x containing N values x_i, the RMS value of x is

$$x_{\mathrm{RMS}} = \sqrt{\frac{\sum_i x_i^2}{N}} \,. \tag{A.3}$$

By definition, the RMS value is always positive.

Half-wave rectification The operation of half-wave rectification simply reduces any function to its positive part. It is denoted by $[\cdots]^+$ and defined by

$$[h(x)]^+ := h(x) \rightarrow \begin{cases} 0 & h(x) < 0 \\ h(x) & h(x) \geq 0 \end{cases} \,. \tag{A.4}$$

A.2 Functions

δ function The δ function ("invented" by Dirac) is not really a function in the normal sense but rather a generalized function or distribution. It can be defined by two properties

$$1. \quad \delta(x - x_0) = 0 \text{ for } x \neq x_0 \,; \tag{A.5}$$

$$2. \quad \int_{x_0 - \epsilon}^{x_0 + \epsilon} \mathrm{d}x \; \delta(x - x_0) = 1 \,. \tag{A.6}$$

The expression $\delta(x - x_0)$ can be seen as a spike of infinite hight and infinitesimal width located at $x = x_0$ such that the surface under the spike equals unity. If the product of a δ

function and an other function h is integrated, this has the effect of sampling the function h at x_0:

$$\int_{-\infty}^{\infty} \mathrm{d}x \ \delta(x - x_0)h(x) = h(x_0) \,. \tag{A.7}$$

θ *function* Heaviside's step function, denoted by θ, is defined as

$$\theta(x) = \begin{cases} 0 & \text{for } x < 0 \\ 1 & \text{for } x > 0 \end{cases} \,. \tag{A.8}$$

The argument x may itself be a function of other variables. The value of $\theta(0)$ is mostly not needed explicitly. For definiteness, however, one can take $\theta(0) = 1/2$.

Alternatively to the definition above, the θ function can be regarded as the integral of the δ function

$$\theta(x) = \int_{-\infty}^{x} \mathrm{d}y \ \delta(y) \,. \tag{A.9}$$

α *function* The α function is often used as a model for postsynaptic responses. It has a quickly rising profile, followed by an exponential decay towards zero. Its definition is

$$\alpha(t, \tau) = \theta(t)\frac{t}{\tau^2}e^{-t/\tau} \,. \tag{A.10}$$

The decay time of the function is set by τ. The normalization is such that $\int_{-\infty}^{\infty} \mathrm{d}t \ \alpha(t, \tau) = 1$. Another common normalization is to give the maximum at $t = \tau$ a value of one, which leads to $\alpha'(t, \tau) = \theta(t) \, t/\tau \, \exp(1 - t/\tau)$.

error function The error function is defined as

$$\mathrm{erf}(z) = \frac{2}{\sqrt{\pi}} \int_0^z \mathrm{d}t \ e^{-t^2} \,. \tag{A.11}$$

It pops up when normalization or integration of a Gaussian function is performed. The error function is odd $[\mathrm{erf}(-z) = -\mathrm{erf}(z)]$ and its value approaches ± 1 for $z \to \pm\infty$.

A.3   Important symbols and parameters

parameter	description	see
membrane voltage and action potentials		
V	membrane potential	App. B.1.1, B.1.2, Eq. (1.4)
E_x	reversal potential	Eq. (1.1), (B.3)
V_r	resting potential	Eq. (1.2), App. B.1.1, B.1.2
τ_m	membrane time constant	App. B.1.1, Eq. (1.4)
τ_{refr}	refraction time	App. B.1.1
τ_s	synaptic time constant	Eq. (1.3)
C_m	membrane capacitance	Sec. 1.2.4, App. B.1.1, B.1.2
$R, g = R^{-1}$	membrane resistivity, conductivity	Eq. (1.2), Sec. 1.2.4, App. B.1.1, B.1.2
I_{inject}	injected neuron current	Sec. 1.2.4, App. B.1.1, B.1.2
response functions and firing rates		
h	general response kernel	Eq. (1.7), Sec. 3.3.1, App. 3.4.1
ε	postsynaptic response	Eq. (1.3), (2.17), Sec. 3.3.2, 4.2.4
J	synaptic strength	Eq. (1.3), (4.3), Sec. 1.3.2, 4.3

A. Notation

λ	Poisson rate function	App. B.2.1, Eq. (2.15), Sec. 4.2
ν	mean firing rate	Eq. (4.13), (4.15)
u	heave response of snake jaw	Sec. 2.3.3
ψ	pitch response of snake jaw	Sec. 2.3.3

learning variables

η	learning parameter	Eq. (1.13), Sec. 4.2.3
w_0, $w^{\mathrm{pre/post}}$	synaptic weight change	Eq. (1.13), Sec. 4.2.3
$W(s)$	learning window	Eq. (1.13), Sec. 4.2.3

miscellaneous

VS	vector strength	Sec. 1.4, 2.4.1, 3.5.5
s	acoustic input signal	Sec. 3.2

B. **Short survey of neuron models**

Building a computational model of a neural network requires a mathematical description of the neurons that are the basic building blocks of the network. There is a huge number of models that have varying degrees of complexity. This appendix discusses some widely-used models of neuronal activity. A more elaborate account of these models (apart from the Izhikevich neuron of section B.2.3) can be found in many textbooks, such as those by Tuckwell [40], Koch [36] or Gerstner and Kistler [29].

The first section focuses on models that are directly rooted in known neuron physiology. The second section discusses more abstract models. Although the latter models are not directly related to neuron physiology, they are still able to capture important aspects of neuronal functioning. The last section of this appendix reflects on the question which neuron model should be chosen from the many possibilities.

B.1 Physiological models

B.1.1 Leaky integrate-and-fire neuron

Perhaps the simplest possible neuron model still directly based on electrophysiological findings is the leaky integrate-and-fire (LIF) neuron. The LIF model is based on the fact that the membrane voltage is determined by the flow of ions, and thus electrical current, through the membrane. Already in 1907, Lapicque recognized that it is possible to model the cell membrane as a simple electrical circuit (translation of the original paper in [37]). In its modern form, the equation describing the membrane potential V reads

$$\dot{V} = -\frac{V - V_r}{\tau_m} + \frac{I_{\text{inject}}}{C_m} \,. \tag{B.1}$$

The voltage change is determined by the ratio between input current I_{inject} and the membrane capacitance C_m. If no input current is present the potential relaxes to a resting value V_r with characteristic membrane time constant $\tau_m = C_m/g$, with g the membrane conductivity.

Equation (B.1) can be represented by the electrical circuit diagram shown in Fig. B.1. The cell membrane of the neuron is reduced to a capacitor and resistance in parallel.

So far, the neuron described by (B.1) does not exhibit spiking behavior. Spiking is achieved by introducing a threshold potential V_θ into (B.1). As soon as the potential crosses this threshold value a spike is defined to occur and the potential is reset to a value V_{reset}. Refractoriness of the neuron can be taken into account by disallowing the neuron to fire for a certain period τ_{refr} after spiking, by changing the threshold voltage temporarily to a higher value, or by temporarily ignoring the input current (see also [29]).

As long as the potential stays below the firing threshold V_θ, the time dependence can be solved exactly. Assuming that the neuron has emitted an action potential and that the potential has been reset to $V = V_{\text{reset}}$ at $t = t_0$ the potential is given by

$$V(t) = V_r + e^{-(t-t_0)/\tau_m} \left[V_{\text{reset}} - V_r + \frac{1}{C_m} \int_{t_0}^{t} \mathrm{d}t' \, e^{(t'-t_0)/\tau_m} I_{\text{inject}}(t') \right] \,. \tag{B.2}$$
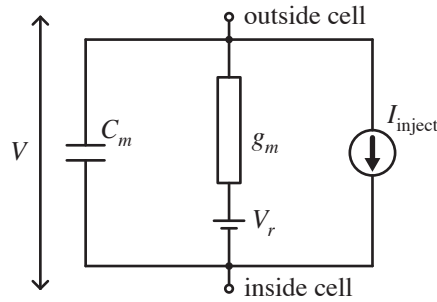
Figure B.1: *A leaky integrate-and-fire neuron can be represented by a simple electrical diagram. The injected current charges a capacitor C_m in parallel with a leak resistance g_m. As soon as the voltage V crosses a threshold value V_θ, a spike is said to occur and the voltage is reset to a value V_{reset}.*
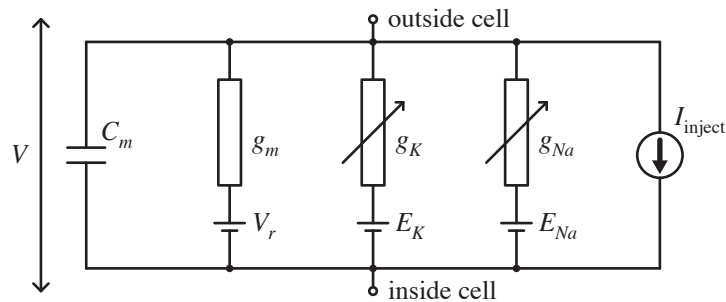
Figure B.2: *The HH model can be visualized by a simple circuit diagram. The parallel ion channels are represented as (variable) resistances. The charge shielding effect of the cell membrane is modeled as a capacitance and the whole system is driven by an external current I_{inject}.*

As soon as spiking is included the analysis becomes very difficult, if not impossible. A review of some analytical results can be found in [24, 25].

B.1.2 Hodgkin-Huxley type neuron

Of the neuron models that are described in this appendix, the Hodgkin-Huxley (HH) type neuron models[1] come closest to being a "true" representation of neuronal functioning. In HH type models, all ion channel types that play a role in action potential generation are individually modeled. The dynamics of one channel type are described by a differential equation giving the fraction of open channels of this type as a function of the potential difference over this channel. Consequently, the conductance contribution of this channel type is then known as a fraction of its maximal conductance (when all channels are open).

The corresponding electrical circuit diagram is shown in Fig. B.2. Originally, the HH model contained two voltage-dependent conductance terms representing the sodium and potassium channels in the membrane. In addition to these two channels, a voltage-independent leak conductance g_m, the membrane capacitance C_m and an input current I_{inject} are taken into account. Below, the slightly more general case with an unspecified number of different ion channels is treated.

The total current through the membrane is given by the sum over all ionic currents plus leak

---

[1]   The original model was developed by Hodgkin and Huxley in 1952 [30], but their approach has been used many times—and continues to be used—by other researchers to construct realistic neuron models [1].

current and injected current. Denoting the channel type by x, the current satisfies

$$I = \sum_x (V - E_x)g_x + (V - V_r)g_m + I_{\text{inject}} \ . \tag{B.3}$$

The reversal potential E_x has been discussed in section 1.2.1, and the leak current is determined by the membrane leak conductance g_m and the resting potential V_r. This leak current occurs because there is always a fraction of ion channels that are not voltage-dependent and which will be open all the time, regardless of the value of the membrane potential. The membrane conductance is thus always nonzero. The equation describing the membrane potential is now given by

$$C_m \dot{V} = I = \sum_x (V - E_x)g_x + (V - V_r)g_m + I_{\text{inject}} \ , \tag{B.4}$$

where C_m is the membrane capacitance.

The interesting dynamics of this equation arise because the channel conductances g_x are not constant but rather a function of the membrane potential V. The conductance contribution g_x for the channel type x is

$$g_x = \bar{g}_x \mu_x^\alpha \lambda_x^\beta \ , \tag{B.5}$$

with $\bar{g}_x$ the maximal conductivity. The parameters α and β are natural numbers and the variables $(\mu_x, \lambda_x) \in [0,1]$ are *activating* and *incactivating* gating variables, respectively. Both μ_x and λ_x satisfy a voltage-dependent differential equation

$$\tau_{\mu_x} \dot{\mu}_x = \mu_{x,\infty} - \mu_x \ , \tag{B.6a}$$

$$\tau_{\lambda_x} \dot{\lambda}_x = \lambda_{x,\infty} - \lambda_x \ , \tag{B.6b}$$

where the variables τ_{μ_x}, τ_{λ_x}, $\mu_{x,\infty}$, and $\lambda_{x,\infty}$ are functions of V. τ_{μ_x} and τ_{λ_x} determine the time scale of the dynamics and $\mu_{x,\infty}$ and $\lambda_{x,\infty}$ give the steady state values of μ_x and λ_x.

The functional dependence of the variables is chosen such that if the membrane voltage V increases from its resting value, the activation variable μ_x grows from its small resting value (the conductance increases) and the inactivation variable λ_x decreases from its resting value, reducing the conductance. The numbers $(\alpha, \beta) \in \mathbb{N}$, which may be zero, determine the impact of the gating variables on the total conductance.

All gating variables satisfy equations of the type (B.6a) and (B.6b). Because the steady state variables $(\mu_{x,\infty}, \lambda_{x,\infty})$ and the timing variables $(\tau_{\mu_x}, \tau_{\lambda_x})$ are different for each ion channel, a complex system of non-linear differential equations arises. This complexity notwithstanding, it is quite easy to understand intuitively how an axion potential arises. If the membrane depolarizes due to some input current, the channels with the shortest activation time constant will quickly open, allowing positive charge (typically sodium ions) to flow in. This further increases the membrane potential. After a short time, other ion channels open (potassium starts flowing *out* of the cell) and the sodium inactivation variable becomes very small, both countering the effect of the charge influx. This mechanism leads to a short peak in the membrane potential followed by a relatively slow decay towards the resting potential.

In their original paper Hodgkin and Huxley used two ion channels determining the membrane permeability for potassium and sodium ions. In modern HH type models, the number of different ionic gates may be as large as a dozen and other ions may play a role in addition to sodium and potassium. Consequentially, a plethora of models has been developed, tailored to match the characteristics of special neuron types found in the brain [1].

B.2 Phenomenological models

B.2.1 Poisson neuron

A Poisson neuron is a simple model neuron with stochastic firing dynamics. The neuron lacks a threshold and may therefore be seen as biologically unrealistic. On the other hand, precisely because of the lacking threshold, the model is linear and can be described very easily mathematically [55, 57], also see [40].

The Poisson neuron model is defined by the following properties:

- The instantaneous firing rate (or rate function) of the neuron, which can be an arbitrary function of time, is given by $\lambda(t)$.

- The probability P that a spike occurs in the small time interval $[t, t + \delta t]$ is given by

$$P_{\text{spike in } [t, t + \delta t]} = \lambda(t)\delta t \,. \tag{B.7}$$

- The probability of getting more than one spike during an interval of length δt is of order $o(\delta t)$, that is,

$$\frac{P_{\text{more than one spike}}}{\delta t} \to 0 \text{ for } \delta t \to 0 \,. \tag{B.8}$$

- The probability of firing a spike does not depend on the previous spiking history of the neuron.

The expectation of the total number of spikes $\langle N \rangle$ that occurs in a given interval $t = [t_0, t_1]$ can be calculated by

$$\langle N \rangle = \int_{t_0}^{t^1} \mathrm{d}t \; \lambda(t) \,. \tag{B.9}$$

Although the spiking probability is independent of the previous spiking history, refractory behavior can be implemented in numerical simulations by using the desired refractory period as step size δt. This possibility should be treated with care, since the analytical expression (B.9) is then invalid.

Although the Poisson neuron model is very simple, it captures some very important aspects of neuron firing. First, neuronal firing is to some degree stochastic, and second, explicit time-dependence of firing probabilities is taken into account. Because of the linearity of Eq. (B.7), an exact mathematical understanding of the learning process is possible [57].

It is to be stressed that the Poisson model is *not* simply equivalent to a rate coding. Since spike generation is explicitly taken into account, the theory and simulations are much richer than they would be with a pure rate-based modeling approach. In addition, the firing rate functions are allowed to have an arbitrary time dependence. The firing rate can therefore vary on a very small time scale, whereas a rate-based description always uses time-averaged firing rates.

The expectation value of the output from a Poisson neuron can be calculated analytically. If a spike occurring at time $t = t_0$ of the Poisson neuron gives rise to a response $h(t - t_0)$, a post-synaptic current, the total response is given by [55]

$$\int_{-\infty}^{t} \mathrm{d}s \; h(t - s)\lambda(s) \,. \tag{B.10}$$

If h is chosen so that causality is ensured, i.e., $h(t) = 0$ for $t < 0$, the expectation of the output is given by

$$\int_{-\infty}^{\infty} \mathrm{d}s \; h(t - s)\lambda(s) \,. \tag{B.11}$$
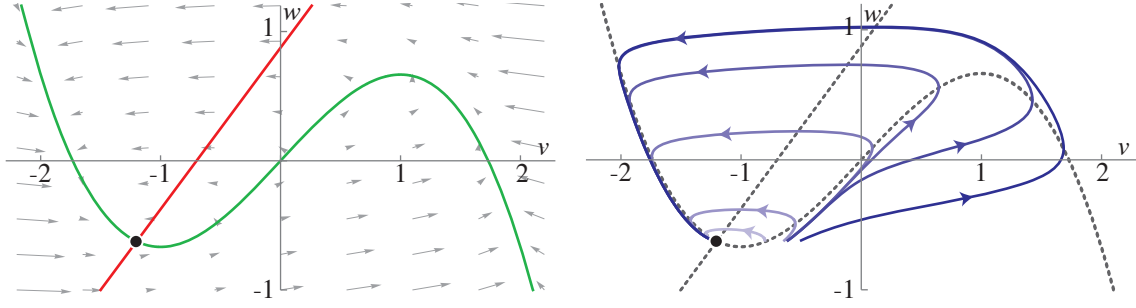
Figure B.3: *Null-clines of the* FN *model (left) and response to a current pulse. Depending on the size of the input pulse, the system can quickly relax to the fixed point, or take a large detour. The "potential variable" v reaches a large value and a "spike" occurs. The transition between these two responses as a function of the current step size is smooth, but occurs so quickly that it can be interpreted as a real threshold.*
Parameter values: $\phi = 0.1$, $a = 0.7$, $b = 0.8$.

Since a Poisson neuron fires stochastically, two realizations of the firing dynamics governed by some particular $\lambda(t)$ will always differ. The variance of the output response can also be calculated explicitly [55] and is given by

$$\int_{-\infty}^{\infty} ds \ h^2(t-s)\lambda(s) \,. \tag{B.12}$$

B.2.2 FitzHugh-Nagumo neuron

Action potential generation in the Hodgkin-Huxley model takes place as a result of the interplay between fast and slow gating variables. If a large enough input is presented,the sodium activation variable rises very rapidly, leading to a quick membrane depolarization. The sodium inactivation variable and the potassium activation follow more slowly, eventually restoring the membrane potential to its resting value.

In the FitzHugh-Nagumo (FN) model [28, 39] the number of dynamic variables is reduced to two. A fast variable, v, that stands for the membrane potential, is coupled to a slowly changing variable, w, that represents the inactivation dynamics of the neuron. The coupled differential equations for v and w are

$$\begin{aligned} \dot{v} &= v - v^3/3 - w + I \\ \dot{w} &= \phi\left(v + a - bw\right). \end{aligned} \tag{B.13}$$

a,b and ϕ are parameters. If ϕ is taken to be small, $\dot{w} \ll \dot{v}$ most of the time unless $\dot{v}$ happens to be very close to zero itself.

This system can be understood using bifurcation theory [260]. In Fig. B.3 the phase diagram of Eq. (B.13) is plotted. In the absence of any input current, the null-clines are given by

$$\dot{v} = 0 \rightarrow w = v - v^3/3 \quad \text{[green]} \tag{B.14a}$$

and

$$\dot{w} = 0 \rightarrow w = \frac{v + a}{b} \qquad \text{[red]} \,. \tag{B.14b}$$

The intersection of the null-clines defines a stable fixed point in the absence of input (Fig. B.3, left).

If a short current pulse is injected, the voltage suddenly jumps to a larger value. If the voltage step is large enough, the voltage variable must increase further (the arrows in the phase diagram
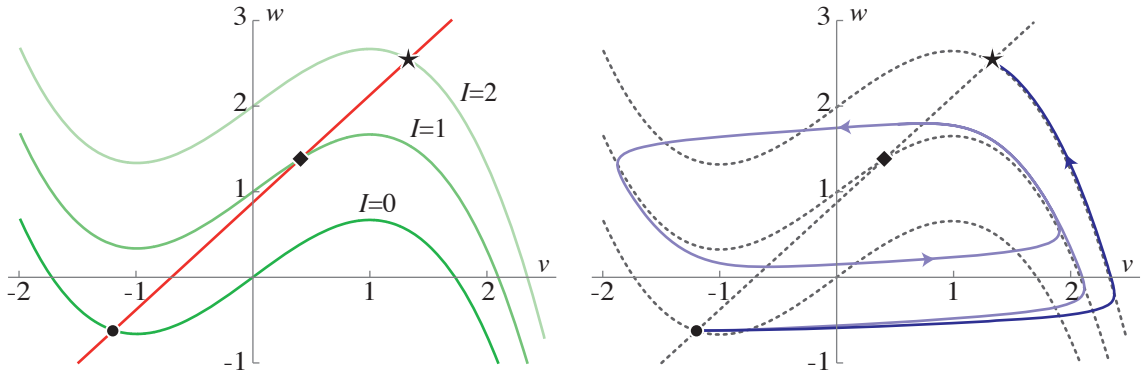
Figure B.4: *Response of the* FN *model to sustained current input. Depending on the size of the input, the system may quickly relax or settle into a limit cycle (regular spike train).*

in Fig. B.3 point to the right), and the only way for the system to relax to the resting state is through a detour involving large values for v and w. This can be interpreted as spiking behavior. For small (sub-threshold) inputs the system directly relaxes to the ground state, and for large (super-threshold) inputs a large voltage excursion (spike) occurs.

The effect of a current step is demonstrated in Fig. B.4. As soon as the current is switched on, the null-cline for v shifts upward. For very small or very large values of the current step (under- or over-stimulation), the new fixed point is stable and the system relaxes to a new stable fixed point. For intermediate current step sizes, the fixed point is unstable. In this case, the system approaches a limit cycle around the fixed point. This can be interpreted as an endless spike train in response to a sustained current input.

Although the equations describing the neuron dynamics in the FN model are quite simple (the only non-linearity is the third power of the potential variable v), interesting and plausible behavior results. The FN model is the most simple neuron model that shows this kind of bifurcation dynamics. For the case shown in Fig. B.4, the three regimes correspond to a fixed point to the left of the local minimum of the v-null-cline (under-stimulation), a fixed point to the right of the local maximum of the v-null-cline (over-stimulation), and a fixed point between the extrema (limit cycle). The two changes in direction of the v-null-cline guarantee that the fixed point changes from stable to unstable to stable if the w-null-cline is shifted upwards.

B.2.3 Izhikevich neuron

Although the FN model provides a very elegant way to understand the behavior of neurons, it is quite limited. The types of responses that can be obtained with the model are quickly exhausted. In many biological systems, highly nontrivial neuronal responses are found. Some neurons respond to constant input, others only to changes in input amplitude. Bursting behavior is regularly found, often with inter-spike and inter-burst intervals that change in time.

To make efficient modeling of such behavior possible, Izhikevich has developed a FN-like model that can reproduce many of the experimentally found spiking responses [31, 32, 33]. Just as in the FN case, there is one slow and one fast variable. The equations describing the system are

$$\dot{v} = 0.04v^2 + 5v + 140 - w + I$$
$$\dot{w} = \phi\left(av - w\right).$$

(B.15)

As soon as the voltage variable v reaches a threshold, a spike is said to occur and both v and w are

reset according to

$$\text{if } v \geq 30, \quad \text{then} \quad \begin{cases} v \to b \\ u \to u + c \end{cases} . \tag{B.16}$$

Depending on the choice for the variables a, b, c, and ϕ, it is possible to obtain a wide range of behaviors.[2] In combination with the threshold, a simple quadratic nonlinearity suffices to generate a whole zoo of neuronal responses. A large advantage of this model is that the computational implementation is very efficient, especially as compared with the HH model.

B.3 Which model to choose?

Depending on the problem at hand, a specific neuron model will be the most suitable choice. If rigorous biological realism is an important criterion, the Hodgkin-Huxley model will often perform well. The equations in the HH model are directly rooted in ion channel physiology and for any type of neuron, an HH-type model can be devised that accurately reproduces this neuron's behavior. The price that must be paid is a very high degree of mathematical complexity. Analytical calculations are generally not feasible. Therefore, HH-type models should only be used where biological realism is of utmost importance.

The Izhikevich neuron is often a much better choice. If realistic spiking behavior is needed, but the physiological details of spike generation are not important, this neuron model can be very helpful. Although an analytical characterization of the spiking behavior is very difficult, the model can be numerically simulated very efficiently. A disadvantage of this model is that extreme care must be taken in specifying the model parameters. Since many qualitatively different neuronal response types can be simulated, it must be known in advance what type of response is needed to obtain biologically realistic results for the system under consideration.

If detailed biological data are lacking—as is often the case—the HH model and the Izhikevich neuron are not very convenient. In this situation, it is better to stick to a simple neuron model. Although some biological precision is lost, a simple neuron model will at least provide a reasonable first approximation. The Fitzhugh-Nagumo neuron has been a very influential model since it allows for an intuitive understanding of the dynamics underlying the much more complicated HH-type models. The FN equations are still quite complicated, although only a relatively limited response repertoire is possible.

A more efficient neuron model is the leaky-integrate-and-fire neuron. The equation describing the membrane potential is exceptionally simple and an analytical characterization of the neuronal response is possible in some cases. The biggest advantage, however, lies in the fact that an extremely efficient numerical implementation of this model is possible. Despite this efficiency, the model commonly does an adequate job. It incorporates (slow) integration of inputs, temporal decay in the absence of input, and has a spiking threshold giving an all-or-none response. If needed noise can be implemented by simply adding a noise term to the input current or by varying the threshold. These properties are exactly the characteristic properties of any real neuron. Therefore, if no reliable biological facts suggests that the LIF neuron is *not* a good choice in a particular situation, the LIF neuron can always be used.

An extremely simplified model of neuronal behavior is given by the Poisson neuron. It lacks a threshold, which makes it amendable to mathematical analysis. A fairly rich response behavior is, however, possible by choosing a suitable expression for the rate function. An important feature of the Poisson neuron is that it is inherently noisy. Neuronal responses are almost always stochastic to some extent, but the Poisson neuron can display an unusually large noise level, depending on the rate function. Still, the advantage of analytical tractability is so substantial, that Poisson neurons are often used.

---

[2] In [33], 20 different types of spiking response are distinguished, which can all be simulated using the Izhikevich neuron model.

B. Short survey of neuron models

Precise neuronal dynamics are not of great importance in this dissertation. The focus is instead on the behavior of (large) neuronal networks. Therefore, all simulations and analytical calculations have been performed using either LIF neurons or Poisson neurons.

Bibliography

To facilitate literature research, the bibliography is thematically organized. A bullet (•) indicates references of high interest or good reviews, and references of historical interest are marked by an **H**. The DOI, or *Digital Object Identifier* is a unique label that allows finding a particular resource on the internet. Just prefixing the DOI with `http://dx.doi.org/` leads to the required article. In contrast to a "normal" internet address, a DOI will never change. In the digital version of this document, all DOIs can be clicked and directly lead to the cited resource.

Brain anatomy and function

[1] • Bean, B.P. (2007) The action potential in mammalian central neurons, Nature Reviews Neuroscience **8** 451–465, DOI: 10.1038/nrn2148.

[2] • Buttler, A.B. & Hodos, W. (2005) *Comparative Vertebrate Neuroanatomy: Evolution and Adaptation* (John Wiley & Sons, New York, NY), 2nd edition.

[3] Comparative mammalian brain collections, Available on-line, maintained by University of Wisconsin, Michigan State University, & National Museum of Health and Medicine, URL: http://brainmuseum.org.

[4] **H** Georgopoulos, A.P., Schwartz, A.B., & Kettner, R.E. (1986) Neuronal population coding of movement direction, Science **233** 1416–1419, DOI: 10.1126/science.3749885.

[5] **H** Hebb, D.O. (1949) *The Organization of Behavior: A Neuropsychological Theory* (John Wiley & Sons, New York, NY).

[6] Heuser, J.E., Group website, URL: www.heuserlab.wustl.edu.

[7] • Hille, B. (2001) *Ion Channels of Excitable Membranes* (Sinauer Associates, Sunderland, MA), 3rd edition.

[8] Hodos, W. & Butler, A.B. (2001) Sensory system evolution in vertebrates, in G. Roth & M.F. Wullimann (editors), *Brain Evolution and Cognition*, pp. 113–133 (John Wiley & Sons, New York, NY).

[9] **H** Hubel, D.H. & Wiesel, T.N. (1962) Receptive fields, binocular interaction and functional architecture in the cat's visual cortex, Journal of Physiology **160** 106–154.2.

[10] **H** Hubel, D.H. & Wiesel, T.N. (1977) Functional architecture of macaque monkey visual cortex, Proceedings of the Royal Society of London B **198** 1–59.

[11] Kole, M.H.P, Ilschner, S.U., Kampa, B.M., Williams, S.R., et al. (2008) Action potential generation requires a high sodium channel density in the axon initial segment, Nature Neuroscience **11** 178–186, DOI: 10.1038/nn2040.

[12] Lee, C., Rohrer, W.H., & Sparks, D.L. (1988) Population coding of saccadian eye movements by neurons in the superior colliculus, Nature **332** 357–360.

[13] • London, M. & Häusser, M. (2005) Dendritic computation, Annual Review of Neuroscience **28** 503–532, DOI: 10.1146/annurev.neuro.28.061604.135703.

[14] Miller, J.P., Jacobs, G.A., & Theunissen, F.E. (1991) Representation of sensory information in the cricket cercal sensory system. I. Response properties of the primary interneurons, Journal of Neurophysiology **66** 1680–1689.

Bibliography

[15] • Nieuwenhuys, R., Donkelaar, H.J. ten, & Nicholson, C. (editors) (1998) *The Central Nervous System of Vertebrates* (Springer, New York, NY).

[16] Schüz, A. (2001) What can the cerebral cortex do better than other parts of the brain?, in G. Roth & M.F. Wullimann (editors), *Brain Evolution and Cognition*, pp. 491–500 (John Wiley & Sons, New York, NY).

[17] Spruston, N. (2008) Pyramidal neurons: Dendritic structure and synaptic integration, Nature Reviews Neuroscience **9** 206–221, DOI: 10.1038/nrn2286.

[18] • Striedter, G.F. (2005) *Principles of Brain Evolution* (Sinauer Associates, Sunderland, MA).

[19] Sylvius neuroanatomical reference, URL: http://www.sylvius.com.

[20] Theunissen, F.E. & Miller, J.P. (1991) Representation of sensory information in the cricket cercal sensory system. II. Information theoretic calculation of system accuracy and optimal tuningcurve widths of four primary interneurons, Journal of Neurophysiology **66** 1690–1703.

[21] • Thompson, R.F. (2000) *The Brain, A Neuroscience Primer* (Worth Publishers, New York, NY), 3rd edition.

[22] **H** Vesalius, A (1543) *De Humani Corporis Fabrica* (Oporinus, Basel), a digital edition has been published by *Octavo digital rare books*, Palo Alto, CA, in 1998.

[23] • Wandell, B.A. (1995) *Foundations of Vision* (Sinauer Associates, Sunderland, MA).

Modeling neurons and neuronal networks

[24] • Burkitt, A.N. (2006) A review of the integrate-and-fire neuron model: I. Homogeneous synaptic input, Biological Cybernetics **95** 1–19, DOI: 10.1007/s00422-006-0068-6.

[25] • Burkitt, A.N. (2006) A review of the integrate-and-fire neuron model: II. Inhomogeneous synaptic input and network properties, Biological Cybernetics **95** 97–112, DOI: 10.1007/s00422-006-0082-8.

[26] Burkitt, A.N. & Clark, G.M. (2001) Synchronization of the neural response to noisy periodic synaptic input, Neural Computation **13** 2639–2672.

[27] Diesmann, M., Gewaltig, M.O., & Aertsen, A. (1999) Stable propagation of synchronous spiking in cortical neural networks, Nature **402** 529–533, DOI: 10.1038/990101.

[28] **H** Fitzhugh, R. (1961) Impulses and physiological states in theoretical models of nerve membrane, Biophysical Journal **1** 445–466.

[29] • Gerstner, W. & Kistler, W. (2002) *Spiking Neuron Models* (Cambridge University Press, Cambridge).

[30] **H** Hodgkin, A.L. & Huxley, A.F. (1952) A quantitative description of membrane current and its application to conduction and excitation in nerve, Journal of Physiology **117** 500–544.

[31] Izhikevich, E.M. (2003) Simple model of spiking neurons, IEEE Transactions on Neural Networks **14** 1569–1572, DOI: 10.1109/TNN.2003.820440.

[32] Izhikevich, E.M. (2004) Which model to use for cortical spiking neurons?, IEEE Transactions on Neural Networks **15** 1063–1070, DOI: 10.1109/TNN.2004.832719.

[33] Izhikevich, E.M. & Hoppensteadt, F. (2004) Classification of bursting mappings, International Journal of Bifurcation and Chaos **14** 3847–3854, DOI: 10.1142/S0218127404011739.

[34] Kempter, R., Gerstner, W., Hemmen, J.L. van, & Wagner, H. (1998) Extracting oscillations: Neuronal coincidence detection with noisy periodic spike input, Neural Computation **10** 1987–2017.

[35] Kempter, R., Gerstner, W., & Van Hemmen, J.L. (1998) How the threshold of a neuron determines its capacity for coincidence detection, Biosystems **48** 105–112, DOI: 10.1016/S0303-2647(98)00055-0.

[36] • Koch, C. (1999) *Biophysics of Computation: Information Processing in Single Neurons* (Oxford University Press, New York, NY).

[37] Lapicque, L. (1907) Recherses quantitatives sur l'excitation électrique des nerfs traitée comme une polarisation, Journal de Physiologie et Pathalogie Générale **9** 620–635, DOI: 10.1007/s00422-007-0189-6, a translation of the original paper by N. Brunel and M.C.W. van Rossum is available: Quantitative investigations of electrical nerve excitation treated as polarization, Biological Cybernetics **97** 341–349 (2007).

[38] **H** McCulloch, W.S. & Pitts, W. (1943) A logical calculus of the ideas immanent in nervous activity, Bulletin of Mathematical Biophysics (presently: Bulletin of Mathematical Biology) **5** 115–133, DOI: 10.1007/BF02478259.

[39] **H** Nagumo, J., Arimoto, S., & Yoshizawa, S. (1962) An active pulse transmission line simulating nerve axon, Proceedings of the IRE **50** 2061–2070, DOI: 10.1109/JRPROC.1962.288235.

[40] • Tuckwell, H.C. (1988) *Introduction to Theoretical Neurobiology*, Cambridge studies in theoretical neurobiology (Cambridge University Press, Cambridge).

Synaptic plasticity

[41] • Abbott, L.F. & Nelson, S.B. (2000) Synaptic plasticity: Taming the beast, Nature Neuroscience **3** 1178–1183, DOI: 10.1038/81453.

[42] Abraham, W.C. (2008) Metaplasticity: Tuning synapses and networks for plasticity, Nature Reviews Neuroscience **9** 387–399, DOI: 10.1038/nrn2356.

[43] Abraham, W.C. & Bear, M.F. (1996) Metaplasticity: The plasticity of synaptic plasticity, Trends in Neurosciences **19** 126–130, DOI: 10.1016/S0166-2236(96)80018-X.

[44] Abraham, W.C. & Tate, W.P. (1997) Metaplasticity: A new vista across the field of synaptic plasticity, Progress in Neurobiology **52** 303–323, DOI: 10.1016/S0301-0082(97)00018-X.

[45] Bell, C.C., Han, V.Z., Sugawara, Y., & Grant, K. (1997) Synaptic plasticity in a cerebellum-like structure depends on temporal order, Nature **387** 278–281, DOI: 10.1038/387278a0.

[46] • Bi, G.Q. (2002) Spatiotemporal specificity of synaptic plasticity: Cellular rules and mechanisms, Biological Cybernetics **87** 319–332, DOI: 10.1007/s00422-002-0349-7.

[47] Bi, G.Q. & Poo, M.M. (1998) Synaptic modifications in cultured hippocampal neurons: Dependence on spike timing, synaptic strength, and postsynaptic cell type, Journal of Neuroscience **18** 10 464–10 472.

[48] Bi, G.Q. & Poo, M.M. (2001) Synaptic modification by correlated activity: Hebb's postulate revisited, Annual Review of Neuroscience **24** 139–166, DOI: 10.1146/annurev.neuro.24.1.139.

[49] Bi, G.Q. & Rubin, J. (2005) Timing in synaptic plasticity: From detection to integration, Trends in Neurosciences **28** 222–228, DOI: 10.1016/j.tins.2005.02.002.

[50] **H** Bienenstock, E.L., Cooper, L.N., & Munro, P.W. (1982) Theory for the development of neuron selectivity: Orientation specificity and binocular interaction in visual cortex, Journal of Neuroscience **2** 32–48.

[51] • Dan, Y. & Poo, M.M. (2004) Spike timing-dependent plasticity of neural circuits, Neuron **44** 23–30, DOI: 10.1016/j.neuron.2004.09.007.

[52] Egger, V., Feldmeyer, D., & Sakmann, B. (1999) Coincidence detection and changes of synaptic efficacy in spiny stellate neurons in rat barrel cortex, Nature Neuroscience **2** 1098–1105, DOI: 10.1038/16026.

[53] Froemke, R.C., Poo, M.M., & Dan, Y. (2005) Spike-timing-dependent synaptic plasticity depends on dendritic location, Nature **434** 221–225, DOI: 10.1038/nature03366.

[54] Gerstner, W., Kempter, R., Hemmen, J.L. van, & Wagner, H. (1996) A neuronal learning rule for sub-millisecond temporal coding, Nature **383** 76–78.

[55] • Hemmen, J.L. van (2001) Theory of synaptic plasticity, in F. Moss & S. Gielen (editors), *Neuro-informatics, Neural Modelling*, volume 4 of *Handbook of Biological Physics*, pp. 771–823 (Elsevier, Amsterdam).

Bibliography

[56] Izhikevich, E.M. & Desai, N.J. (2003) Relating STDP to BCM, Neural Computation **15** 1511–1523.

[57] • Kempter, R., Gerstner, W., & Hemmen, J.L. van (1999) Hebbian learning and spiking neurons, Physical Review E **59** 4498–4514, DOI: 10.1103/PhysRevE.59.4498.

[58] Kempter, R., Gerstner, W., & Hemmen, J.L. van (2001) Intrinsic stabilization of output rates by spike-based Hebbian learning, Neural Computation **13** 2709–2741.

[59] **H** Levy, W.B. & Steward, O. (1983) Temporal contiguity requirements for long-term associative potentiation/depression in the hippocampus, Neuroscience **8** 791–797, DOI: 10.1016/0306-4522(83)90010-6.

[60] Lisman, J. & Spruston, N. (2005) Postsynaptic depolarization requirements for LTP and LTD: A critique of spike timing-dependent plasticity, Nature Neuroscience **8** 839–841, DOI: 10.1038/nn0705-839.

[61] Madison, D.V., Malenka, R.C., & Nicoll, R.A. (1991) Mechanisms underlying long-term potentiation of synaptic transmission, Annual Review of Neuroscience **14** 379–397, DOI: 10.1146/annurev.ne.14.030191.002115.

[62] Markram, H., Lübke, J., Frotscher, M., & Sakmann, B. (1997) Regulation of synaptic efficacy by coincidence of postsynaptic APs and EPSPs, Science **275** 213–215, DOI: 10.1126/science.275.5297.213.

[63] O'Neill, J., Senior, T.J., Allen, K. Huxter, J.R., & Csicvari, J. (2008) Reactivation of experience-dependent cell assembly patterns in the hippocampus, Nature Neuroscience **11** 209–215, DOI: 10.1038/nn2037.

[64] Pfister, J.P. & Gerstner, W. (2006) Triplets of spikes in a model of spike timing-dependent plasticity, Journal of Neuroscience **26** 9673–9682, DOI: 10.1523/JNEUROSCI.1425-06.2006.

[65] Roberts, P.D. & Bell, C.C. (2002) Spike timing dependent synaptic plasticity in biological systems, Biological Cybernetics **87** 392–403, DOI: 10.1007/s00422-002-0361-y.

[66] Rossum, M.C.W. van, Bi, G.Q., & Turrigiano, G.G. (2000) Stable Hebbian learning from spike timing-dependent plasticity, Journal of Neuroscience **20** 8812–8821.

[67] Rubin, J.E., Gerkin, R.C., Bi, G.Q., & Chow, C.C. (2005) Calcium time course as a signal for spike-timing-dependent plasticity, Journal of Neurophysiology **93** 2600–2613, DOI: 10.1152/jn.00803.2004.

[68] Segal, M. (2005) Dendritic spines and long-term plasticity, Nature Reviews Neuroscience **6** 277–284, DOI: 10.1038/nrn1649.

[69] Song, S. & Abbott, L.F. (2001) Cortical development and remapping through spike timing-dependent plasticity, Neuron **32** 339–350, DOI: 10.1016/S0896-6273(01)00451-2.

[70] Song, S., Miller, K.D., & Abbott, L.F. (2000) Competitive Hebbian learning through spike-timing-dependent synaptic plasticity, Nature Neuroscience **3** 919–926, DOI: 10.1038/78829.

[71] Standage, D., Jalil, S., & T., Trappenberg (2007) Computational consequences of experimentally derived spike-time and weight dependent plasticity rules, Biological Cybernetics **96** 615–623, DOI: 10.1007/s00422-007-0152-6.

[72] Tzounopoulos, T., Kim, Y., Oertel, D., & Trussel, L.O. (2004) Cell-specific, spike timing-dependent plasticities in the dorsal cochlear nucleus, Nature Neuroscience **7** 719–725, DOI: 10.1038/nn1272.

[73] Wörgötter, F. & Porr, B. (2005) Temporal sequence learning, prediction, and control: A review of different models and their relation to biological mechanisms, Neural Computation **17** 245–319.

[74] Zhang, L.L., Huizong, W.T., Holt, C.E., Harris, W.A., et al. (1998) A critical window for cooperation and competition among developing retinotectal synapses, Nature **395** 37–44, DOI: 10.1038/25665.

[75] Zhao, J., Peng, Y., Xu, Z., Chen, R.Q., et al. (2008) Synaptic metaplasticity through NMDA receptor lateral diffusion, Journal of Neuroscience **28** 3060–3070, DOI: 10.1523/JNEUROSCI.5450-07.2008.

Neuronal maps and multimodal integration

[76] Anastasio, T.J. & Patton, P.E. (2004) Analysis and modeling of multisensory enhancement in the deep superior colliculus, in G. Calvert, C. Spence, & B.E. Stein (editors), *The Handbook of Multisensory Processes*, chapter 16, pp. 265–283 (MIT Press, Cambridge, MA).

[77] Calvert, G., Spence, C., & Stein, B.E. (editors) (2004) *The Handbook of Multisensory Processes* (MIT Press, Cambridge, MA).

[78] Davison, A.P. & Frégnac, Y. (2006) Learning cross-modal spatial transformations through spike timing-dependent plasticity, Journal of Neuroscience **26** 5604–5615, DOI: 10.1523/JNEUROSCI.5263-05.2006.

[79] Friedel, P. & Hemmen, J.L. van (2008) Inhibition, not excitation, is the key to multimodal sensory integration, Biological Cybernetics **98** 597–618, DOI: 10.1007/s00422-008-0236-y.

[80] Gardner, J.L., Merriam, E.P., Movshon, J.A., & Heeger, D.J. (2008) Maps of visual space in human occipital cortex are retinotopic, not spatiotopic, Journal of Neuroscience **28** 3988–3999, DOI: 10.1523/JNEUROSCI.5476-07.2008.

[81] Gutfreund, Y., Zheng, W., & Knudsen, E.I. (2002) Gated visual input to the central auditory system, Science **297** 1556–1559, DOI: 10.1126/science.1073712.

[82] Hötting, K., Rösler, F., & Röder, B. (2004) Altered auditory-tactile interactions in congenitally blind humans: An event-related potential study, Experimental Brain Research **159** 370–381, DOI: 10.1007/s00221-004-1965-3.

[83] Hyde, P.S. & Knudsen, E.I. (2001) A topographic instructive signal guides the adjustment of the auditory space map in the optic tectum, Journal of Neuroscience **21** 8586–8593.

[84] Jiang, B., Treviño, M., & Kirkwood, A. (2007) Sequential development of long-term potentiation and depression in different layers of the mouse visual cortex, Journal of Neuroscience **27** 9648–9652, DOI: 10.1523/JNEUROSCI.2655-07.2007.

[85] Kaas, J.H. (1991) Plasticity of sensory and motor maps in adult mammals, Annual Review of Neuroscience **14** 137–167, DOI: 10.1146/annurev.ne.14.030191.001033.

[86] Kaas, J.H. & Collins, C.E. (2004) The resurrection of multisensory cortex in primates: Connection patterns that integrate modalities, in G. Calvert, C. Spence, & B.E. Stein (editors), *The Handbook of Multisensory Processes*, chapter 17, pp. 285–293 (MIT Press, Cambridge, MA).

[87] Kempter, R., Leibold, C., Wagner, H., & Hemmen, J.L. van (2001) Formation of temporal-feature maps by axonal propagation of synaptic learning, Proceedings of the National Academy of Sciences of the USA **98** 4166–4171, DOI: 10.1073/pnas.061369698.

[88] **H** King, A.J., Hutchings, M.E., Moore, D.R., & Blakemore, C. (1988) Developmental plasticity in the visual and auditory representations in the mammalian superior colliculus, Nature **332** 73–76.

[89] • Knudsen, E.I. (2002) Instructed learning in the auditory localization pathway of the barn owl, Nature **417** 322–328, DOI: 10.1038/417322a.

[90] Knudsen, E.I. & Brainard, M.S. (1991) Visual instruction of the neural map of auditory space in the developing optic tectum, Science **253** 85–87, DOI: 10.1126/science.2063209.

[91] Knudsen, E.I., Esterly, S.D., & Lac, S. du (1991) Stretched and upside-down maps of auditory space in the optic tectum of blind-reared owls; Acoustic basis and behavioral correlates, Journal of Neuroscience **11** 1727–1747.

[92] **H** Knudsen, E.I. & Knudsen, P.F. (1985) Vision guides the adjustment of auditory localization in young barn owls, Science **230** 545–548, DOI: 10.1126/science.4048948.

[93] Knudsen, E.I. & Knudsen, P.F. (1990) Sensitive and critical periods for visual calibration of sound localization by barn owls, Journal of Neuroscience **10** 222–232.

[94] Linkenhoker, B.A. & Knudsen, E.I. (2002) Incremental learning increases the plasticity of the auditory space map in adult barn owls, Nature **419** 293–296, DOI: 10.1038/nature01002.

[95] **H** Mooney, R.D., Klein, B.G., & Rhoades, R.W. (1987) Effects of altered visual input upon

the development of the visual system and somatosensory representations in the hamster's superior colliculus, Neuroscience **20** 537–555, DOI: 10.1016/0306-4522(87)90109-6.

[96] Opstal, A.J. van & Munoz, D.P. (2004) Auditory-visual interactions subserving primate gaze orienting, in G. Calvert, C. Spence, & B.E. Stein (editors), *The Handbook of Multisensory Processes*, chapter 23, pp. 373–393 (MIT Press, Cambridge, MA).

[97] Putzar, L., Goerendt, I., Lange, K., Rösler, F., et al. (2007) Early visual deprivation impairs multisensory interactions in humans, Nature Neuroscience **10** 1243–1245, DOI: 10.1038/nn1978.

[98] Röder, B., Rösler, F., & Spence, C. (2004) Early vision impairs tactile perception in the blind, Current Biology **14** 121–124, DOI: 10.1016/j.cub.2003.12.054.

[99] Stanford, T.R., Quessy, S., & Stein, B.E. (2005) Evaluating the operations underlying multisensory integration in the cat superior colliculus, Journal of Neuroscience **25** 6499–6508, DOI: 10.1523/JNEUROSCI.5095-04.2005.

[100] Stein, B.E., Jiang, W., & Stanford, T.R. (2004) Multisensory integration in single neurons of the midbrain, in G. Calvert, C. Spence, & B.E. Stein (editors), *The Handbook of Multisensory Processes*, chapter 15, pp. 243–264 (MIT Press, Cambridge, MA).

[101] • Stein, B.E. & Meredith, M.A. (1993) *The Merging of the Senses* (MIT Press, Cambridge, MA).

[102] • Stein, B.E. & Stanford, T.R. (2008) Multisensory integration: Current issues from the perspective of the single neuron, Nature Reviews Neuroscience **9** 255–266, DOI: 10.1038/nrn2331.

[103] Wallace, M.T., Perrault, Jr, T.J., Hairston, W.D., & Stein, B.E. (2004) Visual experience is necessary for the development of multisensory integration, Journal of Neuroscience **24** 9580–9584, DOI: 10.1523/JNEUROSCI.2535-04.2004.

[104] Wallace, M.T. & Stein, B.E. (2007) Early experience determines how the senses will interact, Journal of Neurophysiology **97** 921–926, DOI: 10.1152/jn.00497.2006.

[105] **H** Willshaw, D.J. & Malsburg, C. von der (1976) How patterned neural connections can be set up by self-organization, Proceedings of the Royal Society of London B **194** 431–445.

[106] Winkowski, D.E. & Knudsen, E.I. (2006) Top-down gain control of the auditory space map by gaze control circuitry in the barn owl, Nature **439** 336–339, DOI: 10.1038/nature04411.

[107] Wong, R.O.L. (1999) Retinal waves and visual system development, Annual Review of Neuroscience **22** 29–47, DOI: 10.1146/annurev.neuro.22.1.29.

Auditory system

[108] Avendaño, C., Deng, L., Hermansky, H., & Gold, B. (2004) The analysis and representation of speech, in S. Greenberg, W.A. Ainsworth, A.N. Popper, & R.R Fay (editors), *Speech Processing in the Auditory System*, chapter 2, pp. 63–100 (Springer, New York, NY).

[109] Bendor, D. & Wang, X. (2005) The neuronal representation of pitch in primate auditory cortex, Nature **436** 1161–1165, DOI: 10.1038/nature03867.

[110] Borst, M., Langner, G., & Palm, G. (2004) A biologically motivated network for phase extraction from complex sounds, Biological Cybernetics **90** 98–104, DOI: 10.1007/s00422-003-0459-x.

[111] Brand, A., Behrend, O., Marquardt, T., McAlpine, D., et al. (2002) Precise inhibition is essential for microsecond interaural time difference coding, Nature **417** 543–547, DOI: 10.1038/417543a.

[112] • Bregman, A.S. (1990) *Auditory Scene Analysis* (MIT Press, Cambridge, MA).

[113] Buell, T.N. & Hafter, E.R. (1991) Combination of binaural information across frequency bands, Journal of the Acoustical Society of America **90** 1894–1900, DOI: 10.1121/1.401668.

Bibliography

[114] Cariani, P.A. (2001) Neural timing nets, Neural Networks **14** 737–753, DOI: `10.1016/S0893-6080(01)00056-9`.

[115] Cariani, P.A. (2003) Recurrent timing nets for auditory scence analysis, Proceedings of the International Joint Conference on Neural Networks **2** 1575–1580, DOI: `10.1109/IJCNN.2003.1223934`.

[116] **H** Carr, C.E. & Konishi, M. (1988) Axonal delay lines for time measurement in the owl's brainstem, Proceedings of the National Academy of Sciences of the USA **85** 8311–8315.

[117] Carr, C.E. & Konishi, M. (1990) A circuit for detection of interaural time differences in the brain stem of the barn owl, Journal of Neuroscience **10** 3227–3246.

[118] **H** Cherry, E.C. (1953) Some experiments on the recognition of speech, with one and with two ears, Journal of the Acoustical Society of America **25** 975, DOI: `10.1121/1.1907229`.

[119] Cooke, M. & Ellis, D.P.W. (2001) The auditory organization of speech and other sources in listeners and computational models, Speech Communication **35** 141–177, DOI: `10.1016/S0167-6393(00)00078-9`.

[120] Culling, J.F. & Summerfield, Q. (1995) Perceptual separation of concurrent speech sounds: Absence of across-frequency grouping by common interaural delay, Journal of the Acoustical Society of America **98** 785–797, DOI: `10.1121/1.413571`.

[121] Dean, I., Harper, N.S., & McAlpine, D. (2005) Neural population coding of sound level adapts to stimulus statistics, Nature Neuroscience **8** 1684–1689, DOI: `10.1038/nn1541`.

[122] Demany, L. & Semal, C. (1988) Dichotic fusion of 2 tones one octave apart: Evidence for internal octave templates, Journal of the Acoustical Society of America **83** 687–695, DOI: `10.1121/1.396164`.

[123] Deutsch, D. (1973) Octave generalization of specific interference effects in memory for tonal pitch, Perception and Psychophysics **13** 271–275.

[124] Dyson, M.L., Klump, G.M., & Gauger, B. (1998) Absolute hearing thresholds and critical masking ratios in the european barn owl: A comparison with other owls, Journal of Comparative Physiology A **182** 695–702, DOI: `10.1007/s003590050214`.

[125] Fleischer, G. (1978) *Evolutionary Principles of the Mammalian Middle Ear*, volume 55-5 of *Advances in Anatomy, Embryology and Cell Biology* (Springer, New York, NY).

[126] ● Fletcher, N.H. (1992) *Acoustic Systems in Biology* (Oxford University Press, Oxford).

[127] Friedel, P., Bürck, M., & Hemmen, J.L. van (2007) Neuronal identification of acoustic signal periodicity, Biological Cybernetics **97** 247–260, DOI: `10.1007/s00422-007-0173-1`.

[128] ● Geisler, C.D. (1990) *From Sound to Synapse: Physiology of the Mammalian Ear* (Oxford University Press, Oxford).

[129] **H** Goldberg, J.M. & Brown, P.B. (1969) Response of binaural neurons of dog superior olivary complex to dichotic tonal stimuli: some physiological mechanisms of sound localization, Journal of Neurophysiology **32** 613–636.

[130] ● Grothe, B. (2003) New roles for synaptic inhibition in sound localization, Nature Reviews Neuroscience **4** 540–550, DOI: `10.1038/nrn1136`.

[131] Grothe, B. & Klump, G.M. (2000) Temporal processing in sensory systems, Current Opinion in Neurobiology **10** 467–473, DOI: `10.1016/S0959-4388(00)00115-X`.

[132] Harper, N.S. & McAlpine, D. (2004) Optimal neural population coding of an auditory spatial cue, Nature **430** 682–686, DOI: `10.1038/nature02768`.

[133] Hudspeth, A.J. & Corey, D.P. (1977) Sensitivity, polarity, and conductance change in the response of vertebrate hair cells to controlled mechanical stimuli, Proceedings of the National Academy of Sciences of the USA **74** 2407.

[134] Humphreys, L.J. (1939) Generalization as a function of method of reinforcement, Journal of Experimental Psychology **25** 361–372.

[135] Ingham, N.J. & McAlpine, D. (2004) Spike-frequency adaptation in the inferior colliculus, Journal of Neurophysiology **91** 632–645, DOI: `10.1152/jn.00779.2003`.

[136] **H** Jeffress, L.A. (1948) A place theory of sound localization, Journal of Comparative and

Physiological Psychology **41** 35–39.

[137] • Joris, P.X., Schreiner, C.E., & Rees, A. (2004) Neural processing of amplitude-modulated sounds, Physiological Reviews **84** 541–577, DOI: 10.1152/physrev.00029.2003.

[138] Joris, P.X. & Smith, P.H. (1998) Coincidence detection in the auditory system: 50 years after Jeffress, Neuron **21** 1235–1238, DOI: 10.1016/S0896-6273(00)80643-1.

[139] Köppl, C. (1997) Phase locking to high frequencies in the auditory nerve and cochlear nucleus magnocellularis of the barn owl, *Tyto alba*, Journal of Neuroscience **17** 3312–3321.

[140] Krishna, B.S. & Semple, M.N. (2000) Auditory temporal processing: Response to sinusoidally amplitude-moulated tones in the inferior colliculus, Journal of Neurophysiology **84** 255–273.

[141] Kubke, M.F. & Carr, C.E. (2000) Development of the auditory brainstem of birds: Comparison between barn owls and chickens, Hearing Research **147** 1–20, DOI: 10.1016/S0378-5955(00)00116-7.

[142] Langner, G. (1992) Periodicity coding in the auditory system, Hearing Research **60** 115–142, DOI: 10.1016/0378-5955(92)90015-F.

[143] Langner, G. & Schreiner, C.E. (1988) Periodicity coding in the inferior colliculus of the cat. I. Neuronal mechanisms, Journal of Neurophysiology **60** 1799–1822.

[144] **H** Licklider, J.C.R. (1951) A duplex theory of pitch perception, Experientia **7** 128–134.

[145] MacLeod, K.M., Soares, D., & Carr, C.E. (2006) Interaural timing difference circuits in the auditory brainstem of the emu (*Dromaius novaehollandiae*), Journal of Comparative Neurology **495** 185–201, DOI: 10.1002/cne.20862.

[146] Manley, G.A., Yates, G.K., Köppl, C., & Johnstone, B.M. (1990) Peripheral auditory processing in the bobtail lizard *Tiliqua rugosa* IV. Phase locking of auditory-nerve fibers, Journal of Comparative Physiology A **167** 129–138, DOI: 10.1007/BF00192412.

[147] Meddis, R. & O'Mard, L. (1997) A unitary model of pitch perception, Journal of the Acoustical Society of America **102** 1811–1820, DOI: 10.1121/1.420088.

[148] Meddis, R. & O'Mard, L. (2006) Virtual pitch in a computational physiological model, Journal of the Acoustical Society of America **120** 3861–3869, DOI: 10.1121/1.2372595.

[149] Nelken, I., Rotman, Y., & Bar Yosef, O. (1999) Responses of auditory-cortex neurons to structural features of natural sounds, Nature **397** 154–157, DOI: 10.1038/16456.

[150] Oertel, D. (1999) The role of timing in the brain stem auditory nuclei of vertebrates, Annual Review of Physiology **61** 497–519, DOI: 10.1146/annurev.physiol.61.1.497.

[151] • Pickles, J.O. (1988) *An Introduction to the Physiology of hearing* (Academic Press, London), 2nd edition.

[152] **H** Potter, R.K., Kopp, G.A., & Green, H.C. (1947) *Visible Speech* (D. Van Nostrand Company, New York, NY).

[153] **H** Rees, A. & Møller, A.R. (1983) Responses of neurons in the inferior colliculus of the rat to AM and FM tones, Hearing Research **10** 301–330, DOI: 10.1016/0378-5955(83)90095-3.

[154] Rees, A. & Møller, A.R. (1987) Stimulus properties influencing the repsonses of inferior colliculus neurons to amplitude-modulated sounds, Hearing Research **27** 129–143, DOI: 10.1016/0378-5955(87)90014-1.

[155] Rees, A. & Palmer, A.R. (1989) Neuronal responses to amplitude-modulated and pure-tone stimuli in the guinea pig inferior colliculus, and their modification by broadband noise, Journal of the Acoustical Society of America **85** 1978–1994.

[156] Reyes, A.S., Rubel, E.W., & Spain, W.J. (1996) *In vitro* analysis of optimal stimuli for phase locking and time-delayed modulation of firing in avian nucleus laminaris neurons, Journal of Neuroscience **16** 993–1007.

[157] Schreiner, C.E. & Langner, G. (1988) Periodicity coding in the inferior colliculus of the cat. II. Topograhical organization, Journal of Neurophysiology **60** 1823–1840.

[158] Schuller, G. (1984) Natural ultrasonic echoes from wing beating insects are encoded by collicular neurons in the CF-FM bat, *Rhinolophus ferrumequinum*, Journal of Comparative Physiology A **155** 121–128, DOI: 10.1007/BF00610937.

[159] Shannon, R.V., Zeng, F.-G., Kamath, V., Wygonski, J., et al. (1995) Speech recognition with primarily temporal cues, Science **270** 303–304, DOI: 10.1126/science.270.5234.303.

[160] Smith, J.C., Marsh, J.T., Greenberg, S., & Brown, W.S. (1978) Human auditory frequency-following responses to a missing fundamental, Science **201** 639–641, DOI: 10.1126/science.675250.

[161] Smith, R.L. & Zwislocki, J.J. (1975) Short-term adaptation and incremental responses of single auditory-nerve fibers, Biological Cybernetics **17** 169–182, DOI: 10.1007/BF00364166.

[162] Smith, Z.M., Delgutte, B., & Oxenham, A.J. (2002) Chimaeric sounds reveal dichotomies in auditory perception, Nature **416** 87–90, DOI: 10.1038/416087a.

[163] • Temkin, S. (1981) *Elements of Acoustics* (John Wiley & Sons, New York, NY).

[164] Trussell, L.O. (1999) Synaptic mechanisms for coding timing in auditory neurons, Annual Review of Physiology **61** 477–496, DOI: 10.1146/annurev.physiol.61.1.477.

[165] Werner-Reiss, U. & Groh, J.M. (2008) A rate code for sound azimuth in monkey auditory cortex: Implications for human neuroimaging studies, Journal of Neuroscience **28** 3747–3758, DOI: 10.1523/JNEUROSCI.5044-07.2008.

[166] Westerman, L.A. & Smith, R.L. (1984) Rapid and short-term adaptation in auditory nerve responses, Hearing Research **15** 249, DOI: 10.1016/0378-5955(84)90032-7.

[167] Yost, W.A. (1991) Auditory image perception and analysis: The basis for hearing, Hearing Research **56** 8–18, DOI: 10.1016/0378-5955(91)90148-3.

[168] • Yost, W.A. (1994) *Fundamentals of Hearing: An Introduction* (Academic Press, San Diego, CA), 3rd edition.

[169] Zhang, S. & Trussell, L.O. (1994) A characterization of excitatory postsynaptic potentials in the avian nucleus magnocellularis, Journal of Neurophysiology **72** 705–718.

Fish, amphibians, and the lateral line system

[170] Bleckmann, H. (1988) Prey identification and prey localization in surface-feeding fish and fishing spiders, in J. Atema, R.R. Fay, A.N. Popper, & W.N. Tavolga (editors), *Sensory Biology of Aquatic Animals*, chapter 24, pp. 619–641 (Springer, New York, NY).

[171] • Bleckmann, H. (1994) *Reception of Hydrodynamic Stimuli in Aquatic and Semiaquatic Animals*, number 41 in Progress in Zoology (Gustav Fischer Verlag, Stuttgart, Germany).

[172] Bleckmann, H., Borchard, M., Horn, P., & Görner, P. (1994) Stimulus discrimination and wave source localization in fishing spiders (*Dolomedes triton* and *D. okefinokensis*), Journal of Comparative Physiology A **174** 305–316, DOI: 10.1007/BF00240213.

[173] Bleckmann, H., Breithaubt, T., Blickhan, R., & J., Tautz (1991) The time course and frequency content of hydrodynamic events caused by moving fish, frogs and crustaceans, Journal of Comparative Physiology A **168** 749–757, DOI: 10.1007/BF00224363.

[174] Bleckmann, H., Waldner, I., & Schwartz, E. (1981) Frequency discrimination of the surface-feeding fish *Aplocheilus lineatus* — A prerequisite for prey localization?, Journal of Comparative Physiology A **143** 485–490, DOI: 10.1007/BF00609915.

[175] Claas, B. (1994) Removal of eyes in early larval stages alters the response of the clawed toad, *Xenopus laevis*, to surface waves, Physiology and Behavior **56** 423–428, DOI: 10.1016/0031-9384(94)90284-4.

[176] Coombs, S., Görner, P., & Münz, H. (editors) (1989) *The Mechanosensory Lateral Line: Neurobiology and Evolution* (Springer, New York, NY).

[177] Elepfandt, A. (1986) Wave frequency recognition and absolute pitch for water waves in the clawed frog *Xenopus laevis*, Journal of Comparative Physiology A **158** 235–238, DOI: 10.1007/BF01338566.

[178] • Kalmijn, A.J. (1988) Hydrodynamic and acoustic field detection, in J. Atema, R.R. Fay, A.N. Popper, & W.N. Tavolga (editors), *Sensory Biology of Aquatic Animals*, chapter 4, pp.

83–130 (Springer, New York, NY).

[179] Käse, R.H. & Bleckmann, H. (1987) Prey localization by surface wave ray-tracing: Fish track bugs like oceanographers track storms, Experientia **43** 290–293.

[180] Lang, H.H. (1980) Surface wave discrimination between prey and nonprey by the back swimmer *Notonecta glauca* L. (Hemiptera, Heteroptera), Behavioral Ecology and Sociobiology **6** 233–246, DOI: 10.1007/BF00569205.

[181] Megela Simmons, A. & Ferragamo, M. (1993) Periodicity extraction in the anuran auditory nerve I. "pitch-shift" effects, Journal of Comparative Physiology A **172** 57–69, DOI: 10.1007/BF00214715.

[182] Middleton, J.S., Longtin, A., Benda, J., & Maler, L. (2006) The cellular basis for parallel neural transmission oof a high-frequency stimulus and its low-frequency envelope, Proceedings of the National Academy of Sciences of the USA **103** 14 596–14 601, DOI: 10.1073/pnas.0604103103.

Snakes

[183] Aubret, F., Bonnet, X., Pearson, D., & Shine, R. (2005) How can blind tiger snakes (*Notechis scutatus*) forage successfully?, Australian Journal of Zoology **53** 283–288.

[184] Bonnet, X., Bradshaw, D., Shine, R., & Pearson, D. (1999) Why do snakes have eyes? The (non-)effect of blindness in island tiger snakes (*Notechis scutatus*), Behavioral Ecology and Sociobiology **46** 267–272, DOI: 10.1007/s002650050619.

[185] **H** Bullock, T.H. & Diecke, F.P.J. (1956) Properties of an infra-red receptor, Journal of Physiology **134** 47–87.

[186] • Cock Buning, T. de (1983) Thermal sensitivity as a specialization for prey capture and feeding in snakes, American Zoologist (presently: Integrative and Comparative Biology) **23** 363–375, DOI: 10.1093/icb/23.2.363.

[187] Cock Buning, T. de, Poelmann, R.E., & Dullemeijer, P. (1978) Feeding behaviour and the morphology of the thermoreceptors in Python recticulatus, Netherlands Journal of Zoology **28** 62–93.

[188] • Ford, N.B. & Burghardt, G.M. (1993) Perceptual mechanisms and the behavioral ecology of snakes, in Richard A. Seigel & Joseph T. Collins (editors), *Snakes: Ecology and Behavior*, chapter 4, pp. 117–164 (McGraw-Hill, New York).

[189] Friedel, P., Young, B.A., & Hemmen, J.L. van (2008) Auditory localization of ground-borne vibrations in snakes, Physical Review Letters **100** 48 701, DOI: 10.1103/PhysRevLett.100.048701.

[190] Grace, M.S. & Woodward, O.M. (2001) Altered visual experience and acute visual deprivation affect predatory targeting by infrared-imaging Boid snakes, Brain Research **919** 250–258, DOI: 10.1016/S0169-328X(01)00248-0.

[191] Grace, M.S., Woodward, O.M., Church, D.R., & Calisch, G. (2001) Prey targeting by the infrare-imaging snake *Python*: effects of experimental and congenital visual deprivation, Behavioural Brain Research **119** 23–31, DOI: 10.1016/S0166-4328(00)00336-3.

[192] Halpern, M. (1992) Nasal chemical senses in reptiles: Structure and function, in C. Gans & D. Crews (editors), *Hormones, Brain, and Behavior*, volume 18 of *Biology of the Reptilia*, chapter 7, pp. 423–523 (University of Chicago Press, Chicago, IL).

[193] Hartline, P.H. (1969) *Electrical Responses to Sound and Vibration in the Brains of Snakes*, Ph.D. thesis, University of California, San Diego, CA.

[194] Hartline, P.H. (1971) Mid-brain responses of the auditory and somatic vibration systems in snakes, Journal of Experimental Biology **54** 373–390.

[195] • Hartline, P.H. (1971) Physiological basis for detection of sound and vibration in snakes, Journal of Experimental Biology **54** 349–371.

Bibliography

[196] **H** Hartline, P.H. & Campbell, H.W. (1969) Auditory and vibratory responses in the midbrains of snakes, Science **163** 1221–1223, DOI: 10.1126/science.163.3872.1221.

[197] Hartline, P.H., Kass, L., & Loop, M.S. (1978) Merging of modalities in the optic Tectum: Infrared and visual integration in rattlesnakes, Science **199** 1225–1229, DOI: 10.1126/science.628839.

[198] Jackson, M.K. (1977) Histology and distribution of cutaneous touch corpuscles in some Leptotyphlopid and Colubrid snakes (Reptilia, Serpentes), Journal of Herpetology **11** 7–15.

[199] Jackson, M.K. & Doetsch, G.S. (1977) Functional properties of nerve fibers innervating cutaneous corpuscles within cephalic skin of the Texas rat snake, Experimental Neurology **56** 63–77, DOI: 10.1016/0014-4886(77)90139-X.

[200] Jackson, M.K. & Doetsch, G.S. (1977) Response properties of mechanosensitive nerve fibers innervating cephalic skin of the Texas rat snake, Experimental Neurology **56** 78–90, DOI: 10.1016/0014-4886(77)90140-6.

[201] Kardong, K.V. (1992) Proximate factors affecting guidance of the rattlesnake strike, Zoologische Jahrbücher — Anatomie **122** 233–243.

[202] Kardong, K.V. & Berkhoudt, H. (1999) Rattlesnake hunting behavior: Correlations between plasticity of predatory performance and neuroanatomy, Brain, Behaviour and Evolution **53** 20–28, DOI: 10.1159/000006579.

[203] Kass, L., Loop, M.S., & Hartline, P.H. (1978) Anatomical and physiological localization of visual and infrared cell layers in tectum of pit vipers, Journal of Comparative Neurology **182** 811–820, DOI: 10.1002/cne.901820505.

[204] Krochmal, A.R. & Bakken, G.S. (2003) Thermoregulation in the pits: Use of thermal radiation for retreat site selection by rattlesnakes, Journal of Experimental Biology **206** 2539–2545, DOI: 10.1242/jeb.00471.

[205] **H** Lüdicke, M. (1962-1964) *Ordnung der Klasse Reptilia, Serpentes*, volume VII.I (5) of *Handbuch der Zoologie* (Walter de Gruyter & Co., Berlin).

[206] Meng, J. (2003) The journey from jaw to ear, Biologist **50** 154–158.

[207] • Molenaar, G.J. (1992) Anatomy and physiology of infrared sensitivity of snakes, in C. Gans & P.S. Ulinski (editors), *Sensorimotor Integration*, volume 17 of *Biology of the Reptilia*, chapter 5, pp. 367–453 (University of Chicago Press, Chicago, IL).

[208] Newman, E.A. & Hartline, P.H. (1981) Integration of visual and infrared information in bimodal neurons of the rattlesnake optic tectum, Science **213** 789–791, DOI: 10.1126/science.7256281.

[209] Newman, E.A. & Hartline, P.H. (1982) The infrared "vision" of snakes, Scientific American **246(3)** 98–107.

[210] Parsons, T.S. (1970) The nose and jacobson's organ, in C. Gans & T.S. Parsons (editors), *Morphology B*, volume 2 of *Biology of the Reptilia*, chapter 2, pp. 99–191 (University of Chicago Press, Chicago, IL).

[211] Proske, U. (1969) An electrophysiological analysis of cutaneous mechanoreceptors in a snake, Comparative Biochemistry and Physiology **29** 1039–1046, DOI: 10.1016/0010-406X(69)91006-8.

[212] Proske, U. (1969) Vibration-sensitive mechanoreceptors in snake skin, Experimental Neurology **23** 187–194, DOI: 10.1016/0014-4886(69)90055-7.

[213] Rundus, A.S., Owings, D.H., Joshi, S.S., Chinn, E., et al. (2007) Ground squirrels use an infrared signal to deter rattlesnake predation, Proceedings of the National Academy of Sciences of the USA **104** 14372–14376, DOI: 10.1073/pnas.0702599104.

[214] Schleich, H.H., Kästle, W., & Kabisch, K. (1996) *Amphibians and Reptiles of North Africa* (Koelz Scientific Books, Königstein, Germany).

[215] Schwenk, K. (1994) Why snakes have forked tongues, Science **263** 1573–1577, DOI: 10.1126/science.263.5153.1573.

[216] Sichert, A.B., Friedel, P., & Hemmen, J.L. van (2006) Snake's perspective on heat: Recon-

struction of input using an imperfect detection system, Physical Review Letters **97** 68 105, DOI: 10.1103/PhysRevLett.97.068105.

[217] Underwood, G. (1970) The eye, in C. Gans & T.S. Parsons (editors), *Morphology B*, volume 2 of *Biology of the Reptilia*, chapter 1, pp. 1–97 (University of Chicago Press, Chicago, IL).

[218] • Wever, E.G. (1978) *The Reptile Ear: Its Structure and Function* (Princeton University Press, Princeton, NJ).

[219] Young, B.A. (2003) Snake bioacoustics: Toward a richer understanding of the behavioural ecology of snakes, Quarterly Review of Biology **78** 303–325.

[220] Young, B.A. & Morain, M. (2002) The use of ground-borne vibrations for prey localization in the Saharan sand vipers (Cerastes), Journal of Experimental Biology **205** 661–665.

Vibrational communication and sand waves

[221] Aicher, B. & Tautz, J. (1990) Vibrational communication in the fiddler crab, *Uca pugilator*: 1. Signal transmission through the substratum, Journal of Comparative Physiology A **166** 345–353, DOI: 10.1007/BF00204807.

[222] • Aranson, I.S. & Tsimring, L.S. (2006) Patterns and collective behavior in granular media: Theoretical concepts, Reviews of Modern Physics **78** 641–692, DOI: 10.1103/RevModPhys. 78.641.

[223] Barth, F.G. (1985) Neuroethology of the spider vibration sense, in Friedrich G. Barth (editor), *Neurobiology of Arachnids*, chapter 11, pp. 203–229 (Springer, New York, NY).

[224] • Barth, F.G. (1998) The vibrational sense of spiders, in Ronald R. Hoy, Arthur N. Popper, & Richard R. Fay (editors), *Comparative Hearing: Insects*, chapter 7, pp. 228–278 (Springer, New York, NY).

[225] Barth, F.G. & Geethabali (1982) Spider vibration receptors: Threshold curves of individual slits in the metatarsal lyriform organ, Journal of Comparative Physiology A **148** 175–185, DOI: 10.1007/BF00619124.

[226] Brownell, P.H. (1977) Compressional and surface waves in sand: Used by desert scorpions to locate prey, Science **197** 479–482, DOI: 10.1126/science.197.4302.479.

[227] Brownell, P.H. & Farley, R.D. (1979) Detection of vibrations in sand by tarsal sense organs of the nocturnal scorpion, *Paruroctonus mesaensis*, Journal of Comparative Physiology A **131** 23–30, DOI: 10.1007/BF00613080.

[228] • Brownell, P.H. & Hemmen, J.L. van (2001) Vibration sensitivity and a computational theory for prey-localizing behavior in sand scorpions, American Zoologist (presently: Integrative and Comparative Biology) **41** 1229–1240, DOI: 10.1093/icb/41.5.1229.

[229] Cocroft, R.B. & Rodrigues, R.L. (2005) The behavioral ecology of insect vibrational communication, Bioscience **55** 323–334.

[230] Fertin, A. & Casas, J. (2007) Orientation towards prey in antlions: Efficient use of wave propagation in sand, Journal of Experimental Biology **210** 3337–3343, DOI: 10.1242/jeb. 004473.

[231] • Graff, K.F. (1975) *Wave motion in elastic solids*, Oxford engineering science series (Clarendon Press, Oxford), dover reprint edition 1991.

[232] Hergenröder, R. & Barth, F.G. (1983) The release of attack and escape behavior by vibratory stimuli in a wandering spider (*Cupiennius salei* Keys, Journal of Comparative Physiology A **152** 347–358, DOI: 10.1007/BF00606240.

[233] Hetherington, T.E. (1989) Use of vibratory cues for detection of insect prey by the sandswimming lizard Scincus scincus, Animal Behaviour **37** 290–297, DOI: 10.1016/0003-3472(89) 90118-8.

[234] Hetherington, T.E. (1992) Behavioural use of seismic cue by the sandswimming lizard Scincus scincus, Ethology Ecology and Evolution **4** 5–14.

Bibliography

[235] Hill, P.S.M. (2001) Vibration and animal communication: A review, American Zoologist (presently: Integrative and Comparative Biology) **41** 1135–1142, DOI: `10.1093/icb/41.5.1135`.

[236] Hostler, S.R. & Brennen, C.E. (2005) Pressure wave propagation in a granular bed, Physical Review E **72** 31 303, DOI: `10.1103/PhysRevE.72.031303`.

[237] Hostler, S.R. & Brennen, C.E. (2005) Pressure wave propagation in a shaken granular bed, Physical Review E **72** 31 304, DOI: `10.1103/PhysRevE.72.031304`.

[238] Jaeger, H.M. abd Nagel, S.R. (1996) Granular solids, liquids, and gases, Reviews of Modern Physics **68** 1259–1273, DOI: `10.1103/RevModPhys.68.1259`.

[239] Landolfa, M.A. & Barth, F.G. (1996) Vibrations in the orb web of the spider *Nephila clavipes*: Cues for discrimination and orientation, Journal of Comparative Physiology A **179** 493–508, DOI: `10.1007/BF00192316`.

[240] Lewis, E.R., Narins, P.M., Cortopassi, K.A., Yamada, W.M., et al. (2001) Do male white-lipped frogs use seismic signals for intraspecific communication?, American Zoologist (presently: Integrative and Comparative Biology) **41** 1185–1199, DOI: `10.1093/icb/41.5.1185`.

[241] Lewis, E.R., Narins, P.M., Jarvis, J.U.M., Bronner, G., et al. (2006) Preliminary evidence for the use of microseismic cues for navigation by the Namib golden mole, Journal of the Acoustical Society of America **119** 1260–1268, DOI: `10.1121/1.2151790`.

[242] Magal, C., Schöller, M., Tautz, J., & Casas, J. (2000) The role of leaf structure in vibration propagation, Journal of the Acoustical Society of America **108** 2412–2418, DOI: `10.1121/1.1286098`.

[243] Mason, M.J. & Narins, P.M. (2001) Seismic signal use by fossorial mammals, American Zoologist (presently: Integrative and Comparative Biology) **41** 1171–1184, DOI: `10.1093/icb/41.5.1171`.

[244] Masters, W.M. (1984) Vibration in the orbwebs of *Nuctenea sclopetaria* (Araneidae) II. Prey and wind signals and the spider's response treshold, Behavioral Ecology and Sociobiology **15** 217–223, DOI: `10.1007/BF00292978`.

[245] • Masters, W.M., Markl, H.S., & Moffat, A.J.M. (1986) Transmission of vibration in a spider's web, in William A. Shear (editor), *Spiders: Webs, Behavior, and Evolution*, chapter 3, pp. 49–69 (Stanford University Press, Stanford, CA).

[246] Michelsen, A., Fink, F., Gogala, M., & Traue, D. (1982) Plants as transmission channels for insect vibrational songs, Behavioral Ecology and Sociobiology **11** 269–281, DOI: `10.1007/BF00299304`.

[247] Nieh, J.C. & Tautz, J. (2000) Behaviour-locked signal analysis reveals weak 200-300 Hz comb vibrations during the honeybee waggle dance, Journal of Experimental Biology **203** 1573–1579.

[248] O'Connell-Rodwell, C.E., Wood, J.D., Rodwell, T.C., Puria, S., et al. (2006) Wild elephant (*Loxodonta africana*) breeding herds respond to artificially transmitted seismic stimuli, Behavioral Ecology and Sociobiology **59** 842–850, DOI: `10.1007/s00265-005-0136-2`.

[249] Randall, J.A. & Leweis, E.R. (1997) Seismic communication between the burrows of kangaroo rats, *Dipodomys spectabilis*, Journal of Comparative Physiology A **181** 525–531, DOI: `10.1007/s003590050136`.

[250] Randall, J.A. & Matocq, M.D. (1997) Why do kangaroo rats (*Dipodomys spectabilis*) footdrum at snakes?, Behavioral Ecology **8** 404–413.

[251] Sandeman, D.C., Tautz, J., & Lindauer, M. (1996) Transmission of vibration across honeycombs and its detection by bee leg receptors, Journal of Experimental Biology **199** 2585–2594.

[252] Speck-Hergenröder, J. & Barth, F.G. (1987) Tuning of vibration sensitive neurons in the central nervous system of a wandering spider, *Cupiennius salei* Keys, Journal of Comparative Physiology A **160** 467–475, DOI: `10.1007/BF00615080`.

[253] Stürzl, W., Kempter, R., & Hemmen, J.L. van (2000) Theory of arachnid prey localization,

Physical Review Letters **84** 5668–5671, DOI: 10.1103/PhysRevLett.84.5668.

[254] Tautz, J., Casas, J., & Sandeman, D. (2001) Phase reversal of vibratory signals in honeycomb may assist dancing honeybees to attract their audience, Journal of Experimental Biology **204** 3737–3746.

Miscellaneous

[255] • Clack, J.A. (2002) *Gaining Ground: The Origin and Evolution of Tetrapods* (Indiana University Press, Bloomington, IN).

[256] Clack, J.A. (2002) Patterns and processes in the early evolution of the tetrapod ear, Journal of Neurobiology **53** 251–264, DOI: 10.1002/neu.10129.

[257] Evans, L.C. (1998) *Partial Differential Equations*, volume 19 of *Graduate Series in Mathematics* (American Mathematical Society, Providence, RI).

[258] • Gammaitoni, L., Hänggi, P., Jung, P., & Marchesoni, F. (1998) Stochastic resonance, Reviews of Modern Physics **70** 223–287, DOI: 10.1103/RevModPhys.70.223.

[259] • Newman, J.N. (1986) *Marine Hydrodynamics* (MIT Press, Cambridge, MA).

[260] Strogatz, S.H. (1994) *Nonlinear Dynamics and Chaos: With Applications to Physics, Biology, Chemistry and Engineering* (Perseus Books Publishing, Cambridge, MA).

[261] Thomsen, J.J. (2003) Theories and experiments on the stiffening effect of high-frequency excitation for continuous elastic systems, Journal of Sound and Vibration **260** 117–139, DOI: 10.1016/S0022-460X(02)00916-1.

[262] 2005 visualization challenge, Science **309** 1989–1993, DOI: 10.1126/science.309.5743.1989.

[263] **H** Volterra, V. (1959) *Theory of Functionals and of Integral and Integro-Differential Equations* (Dover Publications, New York, NY), the English edition is an expanded and corrected version of the Spanish original from 1927 based on a series of lectures by Volterra at the University of Madrid in 1925.